

**SURFACE TENSION DRIVEN FLOWS REVEAL POLYMER
PROPERTIES AT THE NANOSCALE**

**NON-EQUILIBRIUM TOPOGRAPHIES:
SURFACE TENSION DRIVEN FLOWS
REVEAL POLYMER PROPERTIES AT THE
NANOSCALE**

By

JOSHUA D. MCGRAW,
BSc (Dalhousie University),
MSc (McMaster University)

A Thesis
Submitted to the School of Graduate Studies
in Partial Fulfillment of the Requirements
for the Degree
Doctor of Philosophy

McMaster University
©Copyright by Joshua D. McGraw, 2012.

DOCTOR OF PHILISOPHY (2012)
(Physics)

McMaster University
Hamilton, Ontario

TITLE: Non-equilibrium topographies: surface tension driven flows reveal polymer properties at the nanoscale

AUTHOR: Joshua D. McGraw,
BSc (Dalhousie University),
MSc (McMaster University)

SUPERVISOR: Dr. Kari Dalnoki-Veress

NUMBER OF PAGES: xi, 126

Abstract

In this thesis, experiments designed to elucidate properties of polymer molecules in confinement are described. Here, confinement means that some dimension of the space in which the polymers are placed in is comparable to the size of the molecules themselves. This smallest dimension is typically a few to ten times the molecular size, which for the polymer molecules described here is normally in the range of tens to hundreds of nanometres.

In most cases, the experiments were designed around the concept that nature tends to minimize the surface area of a liquid. The most important results are those concerned with the levelling of a stepped film's height profile. Films are prepared such that their height profiles are well described by a Heaviside step function and to a good approximation, they are invariant in one dimension. The temporal dependence of the levelling gives rheological information about the molecules making up the stepped films. For the range of heights that is much larger than the typical size of molecules making up the film, we use classical hydrodynamics to model the flows in these stepped films. Having measured the temporal and geometric dependence of the energy dissipation in time, we find that the hydrodynamic models are in excellent agreement.

Apart from the liquid state evolution of stepped films this thesis also contains material concerned with non-equilibrium properties of thin polymer films. A common method of preparing films is spin coating. This violent process can leave polymer chains in non-equilibrium configurations. We have made measurements addressing the questions: what are the conformations of as-cast, spin coated polymer chains? Furthermore, if we anneal as-cast films, how long does it take for the polymer chains to relax to an equilibrium? We found that polymer chains are strongly stretched by the spin coating process, and that it takes about one bulk polymer relaxation time to lose memory of the preparation procedures for our films prepared on mica. In related experiments, we confined molecules to films thinner than a typical length scale for the polymers, then made bilayers out of such films. This creates what we refer to as an entropic interface, across which polymer chains suffer a reduction in entropy due to their inability to explore some conformations. We find that this entropic interface heals on a time scale that is much faster than one bulk polymer relaxation time.

Preface

This is a ‘sandwich’ thesis, based on papers published or submitted during my PhD work. As an introduction, the first two chapters consist of an overview of the concepts required to understand the works presented in the papers (see Appendix) and some details concerning the sample preparation and analysis. It is hoped that the second chapter will be useful to those who consider performing crazing or stepped film levelling experiments. Chapter 3 contains descriptions of the published or submitted works, and specifically addresses my contributions to each of them. For these projects in which I was the main contributor, manuscripts are included in the Appendix. Additionally, I have been involved with projects in which I was not the main contributor. These are also outlined in a second appendix, but are not included in this thesis.

Acknowledgements

Thanks.

That's basically it. In the more than six years since I arrived in Hamilton, this is the most insignificant statement I could make to all of the great people I've encountered here – it's a start, though, so here we go.

Hamilton has changed me: I've become acutely aware that cities are made out of the people who live in them, with great people making great cities. Hamilton is a great city. Thank you, Hamilton.

Downsizing the previous thought, it can also be said that great departments are made out of the great people who run them. I am then indebted to the administrative staff who have fought so hard to make life easier since my arrival to the Department of Physics and Astronomy: (from east to west) Tina, Cheryl, Rose and Mara. Thank you.

Great groups are also made from the people who live in them. I therefore must dutifully, and happily, so happily and full heartedly, thank Drew, Adam, MJ, Jess, MA, Joe, Mark, Rob, Sara, Matilda, Mark, Paul and Raffi. Sharing offices, cars, planes, hotels, labs, tents, stories, advice, wisdom and all that together has been truly wonderful. If ever I am so fortunate to encounter a group of such talented, enthusiastic and beautiful people, then I will be happy to claim that it's no big deal if lightning strikes twice.

Friends, you are the ones making it the most difficult for me to leave this place I've come to call home. Each for a very special reason, I have to give space in these acknowledgements to PhilPatMike, Brendan, Clare, Claire, Laura, Blair, Kendall, Andreas, Jess, and Jackie. You are fabulous friends. Lightning strikes twice and it's no big deal.

Tom and Oliver, whom I must thank as collaborators, but could easily have appeared in that list of the previous paragraph. I hope that we can find a way to continue attacking science together. I have also to thank Elie for joining the project. Without your guidance and Tom's talent, much of this work would not have been possible, certainly it would have been of a lower quality without the three people listed here. A.-C. Shi, J. Li; and M.W. Matsen are thanked in the same spirit.

Undergrads, let's talk about talent. In chronological order: David Tran, Ian Rowe,

Nick Jago, Mel Ferrari and Paul Fowler. Your hard work and intelligence have in large measure brought me here. I wish you continued success, which you all seem to be enjoying. You (I have to add Sara here, though not as an undergrad) have taught me more than you would care to take credit for, thank you for the lessons.

Mom and Dad. How much and in how many ways can two people support such a life? I always tell people that doing a PhD is not such a big deal, you just need to take the appropriate number of baby steps. You held my hand for all the right baby steps from the real beginning, and let me fall on my face occasionally. This is definitely the right way, and I appreciate your guidance, understanding and wisdom. The very fact that you play this role so well to *six* people is all the more amazing. You're wonderful parents, and I love you. Thanks to Mark, Leah, James, Liz and Joe. You're the best I could have and I love you too.

Kari, I could put you in all the paragraphs. You enthusiastically welcomed me to Hamilton, this great city, made me a home in the great department and have built the best group. You are a valuable friend, a valued collaborator. You are the best supervisor that a student could have. I have often turned to you for advice outside of the called for duties of a supervisor, and you have every time been a strong voice. For every success, one must give credit to the giants on whose shoulders they stood. For this success, I have to thank you, if only one, as the best giant I could have hoped for. Thanks.

Contents

Abstract	iii
Preface	v
Acknowledgements	vi
1 Introduction	1
overview of the papers	4
1.1 polymers	5
1.1.1 solutions	8
1.1.2 diblocks	11
1.1.3 phase separation	12
1.2 entanglement	14
1.2.1 viscosity	18
1.2.2 crazing	19
1.2.3 confinement	21
1.2.4 non-equilibrium networks	23
1.2.5 blends	25
1.3 surface tension	25
1.4 hydrodynamics	28
1.4.1 steps	31
1.4.2 bumps	32
1.4.3 rings	35

CONTENTS

2	Experimental Details and Data Analysis	37
2.1	sample preparation	37
2.2	crazing	39
2.3	capillary levelling	42
3	Summary of Papers	51
4	Outlook and Conclusions	61
	Slip Thin Film Equation	62
	Ultrathin Film Equation	63
	Asymmetric Thin Film Equation	64
	Conclusion	66
A	Appended Papers	69
	Step Levelling, Experiment i (Soft Matter)	69
	Step Levelling, Experiment ii (PRL)	77
	Ring breakup: homopolymers (Soft Matter)	83
	Rings: diblock edge repulsion (EPJE)	89
	Craze: Blends (PRE)	98
	Craze: Non-Equilibrium (submitted to EPJE)	104
B	Other Contributions	113

List of Figures

1.1	Schematic diagram of polymer torsion angles	7
1.2	Correlation blobs for a chain in solution	10
1.3	Diblock chains and film morphologies	12
1.4	Entangled polymer tube relaxation	15
1.5	Schematic of a crazing experiment, and chain deformation	20
1.6	Schematic of hydrodynamic velocity profiles	22
1.7	Surface tension and Laplace pressure	26
1.8	Schematics of levelling samples	32
2.1	Schematic of vacuum ovens	38
2.2	Typical craze data	41
2.3	Typical capillary levelling data	45
2.4	Fit of computational solution to levelling data	47
4.1	Outlook: slip and confinement	64
4.2	Outlook: asymmetric M_w distributions	66
B.1	Droplet levelling profiles	116

LIST OF FIGURES

Chapter 1

Introduction

Brownian motion can occur when a particle is continuously subjected to small nudges in random directions due to thermal fluctuations. In a particular simple case the particle is being pushed by its neighbours in a dense ensemble of identical particles, as in a viscous liquid. In this case the nudges are small in the sense that the reaction of such forces is not so large that the particle moves a distance comparable to its size before being slowed by viscous dissipation, that is, before being nudged in a completely new direction. Thus, continuously by small amounts but steadily, the particle is randomly pushed to and fro. Eventually it escapes its local environment and finds new neighbours.

A complication can be introduced by permanently attaching particles together. If almost all of the particles are given two permanent neighbours (and disallowing for the possibility of triangular couplings), our simple liquid becomes a sea of long chain-like molecules. Thus, every time a particle is pushed, it must drag along its two neighbours, which in turn must drag along their other neighbours, and so on. At first sight this problem may seem intractable, but it is the problem of polymer physics. While there is indeed much to be learned, we do have a considerable knowledge concerning these systems [1,2]. Nevertheless, some new insights into the problems of polymer physics are contained in this thesis.

Given that particles, the *monomers*, are constrained by being attached to two of their neighbours, one expects that the time it takes to find new, unattached, neighbours would be much longer than in the simple liquid case. In fact, synthetic chemists

can now easily make chains that have 10^4 monomers, such that the times taken for all monomers to find new neighbours in a melt of identical chains is approximately $10^{10} - 10^{12}$ times longer than for the monomeric liquid case [1–3]. This enormous increase in time scales for relaxation means that polymer liquids are highly viscous [4]. In addition, polymer systems have many other properties that make them distinct from monomeric solids or liquids.

In numerous cases, the distinction between polymeric materials and regular monomeric materials arises because of interactions called entanglements [1–3, 5–7]. Entanglements are the collections of interactions between two different chains that disallow polymer chain backbone crossings. As will be seen throughout this thesis, entanglements manifest themselves in many ways. Chief among them is through the viscosity of a polymer liquid that inhibits a flow induced by surface tension. However we will see several other examples: the arrangement of the entanglements within a system, and the chain statistics between the entanglements play an important role in the observed behaviour of a polymer system.

Moving away from bulk, macroscopic liquids, we must make a distinction between molecules near a surface and those within the liquid. The difference is that, at a surface, the molecules are missing some of the neighbours [8, 9] they would have had in the bulk. Thus, these surface or interface molecules are in a different energy state as compared to their counterparts within a bulk liquid. As such, we may expect that the surface molecules will act quite differently. This difference is important in many industrial applications and in nature.

There are many unanswered questions concerning the topic of polymers at surfaces and interfaces. Most of the experiments described in this thesis are motivated by a desire to understand the properties of interfacial polymers. Using polymers to study molecular interfaces has several practical advantages because polymers are much larger than typical molecules. The most important idea is that by virtue of the huge number of monomers in a polymer chain, the specific chemical makeup of the monomers is less important than the very fact that the molecules are just *long*. It has been shown [1, 10] that this universality allows fairly general statements to be made about observed polymer behaviours, even if we mostly use polystyrene as a model system in the work presented in this thesis. Second, polymer molecules are

relatively easy to confine because of their size. Thus, in the study of systems with sizes comparable to the constituents, polymers make great candidates. On a more technical note, polymers are not volatile under the conditions in which they are used here. As such, the volume of our systems remains constant with time.

In this thesis, when experiments are not directly probing the properties of polymers at surfaces (*e.g.* chain configurations), the observations made are heavily influenced by a surface or interfacial tension. Specifically, surface tension can provide a driving force inducing a flow when the topography is non-uniform. Thus, we have entanglements that inhibit flow, and a surface tension that drives it. This interplay forms the basis on which the hydrodynamics discussed herein is developed.

In the following sections, all of the topics that have been addressed in this short introduction will be developed in more detail. We start with a general introduction to polymers in the melt, then move to a short discussion on polymers in solution. Some of the relevant interfaces here are between different blocks of single co-polymer chains, so a description of these exotic molecules will be given. It will be seen that if the polymer chains are long enough, entanglements start to dominate the observed physics and several implications will be discussed. A section devoted to the topic of surface tension follows, then some thin film hydrodynamics (using the lubrication approximation) in various geometries is presented. These topics form the basis of the first chapter. In the second chapter, details of experimental procedures are given, and then some particular analysis methods are described as they are not fully explained in the manuscripts presented at the end of the thesis. Chapter 3 gives an overview of these papers, and in particular details my specific contributions to them. There is a final section that discusses the conclusions that may be drawn from the papers presented. Some outlook is also given, in particular where this refers to the studies of the hydrodynamics of stepped polymer films. An appendix contains the published or submitted manuscripts. Before continuing with a discussion of the physics of polymers, however, a short description of the specific projects presented in the Papers will be given.

overview of the papers

It can be said that this thesis is (almost) all about surface and interfacial tension. With the exception of one experiment presented here, surface tension drives all of our polymer surfaces to be flat. Additionally, interfaces that exist as a result of surface tension act as uncrossable boundaries for polymer chains, thus affecting their entanglement networks. Surface and interfacial tensions are at the root of all the driving forces in the dynamical experiments presented here. In the simplest case, we have a polymer film with a step in the height profile,

$$h(x, y) = h_1 + h_2\Theta(x) . \quad (1.1)$$

$\Theta(x) = 1$ if $x > 0$ but equals zero otherwise. Over the range of distances that we measure, it can be assumed that this step is infinitely wide in the y -direction, and that the flat regions extend to $\pm\infty$ in the x -direction. When these films are heated to above the glass transition (polystyrene with $T_g \approx 97^\circ\text{C}$ is used), surface tension drives a flow that levels out the step. The levelling occurs because this decreases the surface area, thus decreasing the energy of the system. This is the work presented in Papers 1.i, 1.ii and 2.i, 2.ii. It will be shown that understanding this system provides a versatile tool that can be used for the study of polymers at surfaces and interfaces. In Paper 2.iii, this stepped surface is changed such that we assume the surface to be flat everywhere except for a small spherical cap sitting on an identical fluid. This spherical cap also has an excess in the surface area and as before the surface tension drives a flow for flattening to occur. The thickness of the bottom layer is changed and we see a power law crossover in the dynamics.

Paper 1.iii deals with another surface tension driven flow in which the surface is shaped like a toroidal section. The surface breaks up into a collection of droplets as water would after falling out of a faucet, this is the Plateau-Rayleigh instability. The novelty of this system is in the toroidal nature of the structure, which offers an alternative energy minimization route – the torus can just close up if the geometry is right. Paper 1.iv sees the polymer tori composed of molecules called diblock copolymers. These are molecules composed of two linear blocks of distinct chemistry. Under our experimental conditions the diblocks phase separate into lamellar structures; how-

ever, defects inevitably exist. By using the toroidal shapes, we have found that we can elucidate how these defects interact with one another. Paper 2.iv is a theoretical study of the lamellar defects in isolation.

Papers 1.v and 1.vi are not about surface tension. Here we undertake to study the entanglement networks in various polymer films. We investigate the effect of blending short chains with long chains on the entanglement network. It is found that short chains can act as a diluent for some of the entanglements that would have been present in a pure long-chain system. In the second study of entanglement networks, we look at non-equilibrium systems prepared by spin coating, or by creating a barrier for the chains which is uncrossable and then lifting the restriction. In both cases, the temporal evolution of the chain statistics is monitored and we extract relaxation times that are described in terms of the longest relaxation time of the polymers in the bulk. Paper 2.v also deals with issues related to non-equilibrium chains. In this case, we study the effect of free surfaces on the glass transition and determine that the number and type of interfaces plays a central role in the glass transition.

1.1 polymers

As discussed above, a polymer is formed by covalently bonding many monomers together in a chain¹. Confining ourselves to this architecture, a single characteristic is enough to determine many properties of a monodisperse melt, this being the number of monomers in a molecule, N (also called the degree of polymerization). Since the monomers making up a homopolymer chain are all the same, specifying the molecular weight M is also sufficient to describe a molecule. M and N are related by the monomer mass, m_o , through $M = m_o N$. Here m_o is the molar mass of a statistical monomer, which comprises more than one chemical monomer. In synthetic systems, one must deal with the fact that typical polymerization routes do not produce chains whose lengths are all identical, thus the ensemble of chains is polydisperse. The most common method of characterizing the polydispersity is through a function of moments

¹The preparation of polymer molecules is not limited to putting monomers together linearly. It is possible to make polymers with many different architectures, including combs, stars, dendrites, and H-shaped “dumbbells”, among others. For the purposes of this thesis, however, we will only be concerned with linear molecules.

of the chain length distribution. The number and weight averaged molecular weights are defined by

$$M_n = \frac{\sum_i n_i M_i}{\sum_i n_i}, \quad (1.2)$$

$$M_w = \frac{\sum_i n_i M_i^2}{\sum_i n_i M_i}, \quad (1.3)$$

where n_i are the numbers of chains with molar mass M_i . The polydispersity index is defined as $PI = M_w/M_n$. Molar mass distributions with $PI < 1.1$ are commonly called ‘monodisperse’, and unless otherwise noted, the systems studied here satisfy this convention.

Once we have a melt of polymer chains, we can ask what each of the chains looks like. We first consider an arbitrary section of chain that is four monomers long. While the angle between any three successive monomers is typically well defined, there is some flexibility in the torsional angle, ϕ : the vector between the positions of the third and fourth monomers can leave the plane defined by the positions of the first three monomers [1], see Fig. 1.1(a). As seen schematically in Fig. 1.1(b), the energy for *trans* states is slightly less than for *gauche* states. Nevertheless, the two *gauche* states are taken with equal nonzero probability. This gives polymer chains flexibility which leads to their performing random walks as schematically shown in Fig. 1.1(c). Since the *trans* state is preferred², more than one monomer is required for the segments to become uncorrelated, but the correlations die out quickly. For PS in the melt, it takes approximately 7 monomers for the segments to become uncorrelated, and this is typical for a variety of polymers [2]. Therefore, at a given instant of time each chain has the conformation of a random walk. Here, interactions with monomers far along the chain have been ignored. While there is a hard core repulsion between monomers on the same chain, these interactions are the same as those with monomers on other chains. As such, there is no preference in the melt for a monomer to interact with monomers on the same chain or on other chains, and the random walk statistics are preserved [1].

²For atactic polystyrene (PS) whose side groups are randomly distributed in direction on the polymer backbone, the *trans* state has been measured to occur with a probability of approximately 0.68 [11].

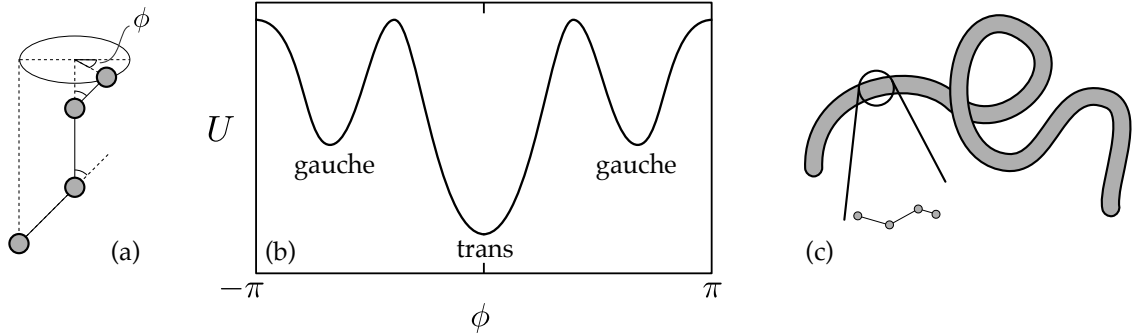


Figure 1.1: (a) Schematic of a 4-monomer segment of a polymer chain, with torsion angle ϕ , the dashed lines lie in the plane defined by the three lower monomers. (b) The energy U of the small polymer subunit is dependent on ϕ , leading to correlation of monomer orientation on short length scales. (c) On scales larger than the Kuhn length, b , the monomer correlations die out, and the polymer does a random walk in the melt. (a), (b) adapted from [1]

If chains perform random walks, then their size distribution is Gaussian as mentioned above. For purely Gaussian chains, the root-mean-square end-to-end distance of a chain is given by

$$R_{ee} = bN^{1/2}, \quad (1.4)$$

where b , the Kuhn length, is the size of a *statistical monomer*. That is, N is the number of uncorrelated chain segments, each of which have a linear dimension b . A length scale related to the end-to-end distance is the radius of gyration, which is defined as the root-mean-square distance of monomers from the centre of mass of the molecule (this is a more relevant length scale for polymers of more exotic architecture). The radius of gyration for a linear molecule is simply related to the end-to-end distance through a numerical coefficient, $R_g = R_{ee}/\sqrt{6}$ [2]. In neutron scattering experiments, it is possible to measure the radii of gyration for an ensemble of chains. This was done for deuterated polystyrenes of various molecular weights and it was found that

$$R_g = (\kappa M_w)^{1/2} \quad (1.5)$$

with $\kappa^{1/2} = 2.75 \times 10^{-2}$ nm mol/g [12] for PS; here a typical molecular weight will be $M_w \approx 100$ kg/mol which thus has a radius of gyration of about 9 nm, and an end-to-end distance of $R_{ee} \approx 22$ nm.

One consequence of the fact that polymer chains take on random walk configurations is that their structures are quite open. We define the pervaded volume, V_p , as the smallest sphere that would enclose an entire polymer chain. In a melt of like chains, the amount of space occupied by other chains inside the pervaded volume is considerable. Since $V_p \sim R_{ee}^3$, and the volume taken up by the chain is only $V_c \sim N$, the fraction of space actually occupied by the chain in its own pervaded volume is $P_c = V_c/V_p \sim N^{-1/2}$. Since $N \gg 1$ in most cases we see that the chain occupies only a small fraction of its pervaded volume, thus there are many interactions between monomers on a given chain with monomers on the other chains in its immediate vicinity.

1.1.1 solutions

isolated chains

In the previous section, we justified the idea that polymer chains undergo random walks in the melt. As a result of the random walks, chains have end-to-end distances or radii of gyration that scale with the square root of the number of monomers. This scaling does not hold if an isolated polymer chain is in solution. For the purposes of this thesis, we will consider only the case where the solvent is strongly attracted by the monomers on the chain – the case of an athermal solvent. From an energetic point of view, the polymer chain would prefer to have only solvent around each of its monomers. Thus, for the case in which entropy is neglected, the chain should be completely straight such that each monomer is surrounded by a maximum number of solvent molecules. Of course, this rod-like configuration severely reduces the entropy (only one state is completely stretched out), so the real conformation is somewhere in between the Gaussian coil and the straight rod.

Using a simple argument due to Flory, an estimate can be made for the size of an isolated polymer chain in solution. Following [2], we start from the assumption that

the entropy is derived from the Gaussian probability distribution:

$$S(R) = k \ln \Omega \approx k \left(\frac{-3R^2}{2b^2N} + \text{const.} \right), \quad (1.6)$$

since the Gaussian probability distribution is exponential in the first term. The constant due to the normalization does not depend on R , and k is Boltzmann's constant. The enthalpic contribution can be estimated using a mean field approach. The interaction energy per monomer-monomer interaction is determined by the excluded volume of the monomer-solvent pair. This excluded volume, v , is determined by integrating the Boltzmann factor weighted monomer-monomer interaction potential over all space. For an athermal solvent $v \approx b^3$, the monomer volume. The interaction energy is kT per excluded volume. Inside the polymer coil, the concentration of solvent is $c = N/R^3$. The probability of monomer-monomer interactions is proportional to c , and there are N such interactions, so the enthalpic contribution to the free energy is $U \approx kTvN^2/R^3$. Therefore, the free energy of interaction of the polymer coil is

$$F = U - TS = kT \left(\frac{b^3N^2}{R^3} + \frac{3R^2}{2b^2N} \right). \quad (1.7)$$

In equilibrium, the free energy is minimized (*i.e.* $\partial F/\partial R = 0$), yielding a relation for size scaling of an isolated 'Flory' polymer in an athermal solvent:

$$R_f \approx bN^{3/5}. \quad (1.8)$$

This mean field approach gives an exponent which is close to the answer given by more accurate calculations accounting for correlations between the monomers. Using Monte Carlo simulations, for example, it can be found that $R_f \approx bN^\nu$ where $\nu \approx 0.588$ [13].

overlapping chains

As the concentration of polymer increases in a solution, chains begin to overlap. Since in the melt chains have size that scales with $N^{1/2}$ while in dilute solution their size varies approximately according to Eq. 1.8, we see that the chains must somehow transition between the two scaling regimes. On length scales that are small compared

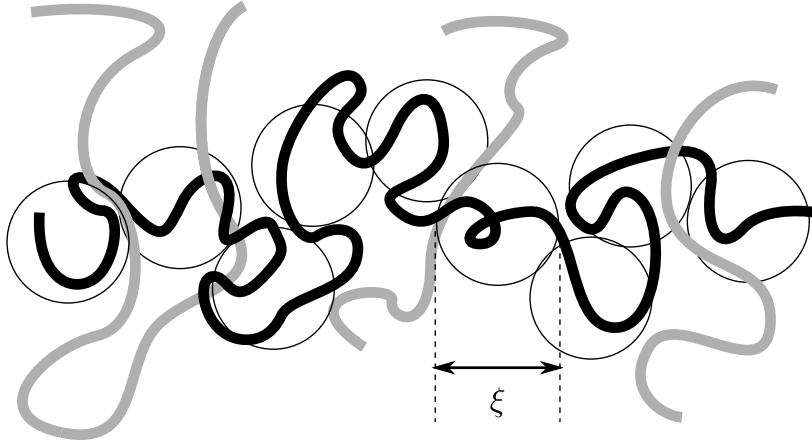


Figure 1.2: Schematic of a polymer chain in solution (solvent not shown). Each blob of monomers is composed mainly of monomers from a single portion of the chain. On length scales larger than ξ , the chain starts to interact with monomers from other chains (grey) and from monomers from different segments of the same chain.

to the typical distances between chain overlap in solution, chain segments do not know that other chains are in the solution. These small segments with g monomers have Flory statistics as described by the exponent $\nu \approx 3/5$: their size is

$$\xi = bg^\nu, \quad (1.9)$$

as demonstrated in Fig. 1.2. Each of these segments can be seen as a collection of monomers with their associated solvent (even though the solution is not static, the solvent molecules are continuously associated with different chain segments). These correlation ‘blobs’ [1, 2] are space filling, they have the same concentration as the solution itself:

$$c = g/\xi^3. \quad (1.10)$$

Each correlation blob is chemically identical, and just as in the melt, there is no difference between a correlation blob interacting with another on the same chain, or on a different chain. Thus, the correlation blobs are ideal in the sense that they perform random walks, so that $R_s = \xi(N/g)^{1/2}$ is the size of a chain in solution.

Using Eqs. 1.9 in place of ξ , we find the polymer size in solution to be

$$R_s = bg^\nu \tilde{N}^{1/2} \quad (1.11)$$

where $g = (b^3c)^{1/1-3\nu}$ and $\tilde{N} = N/g$. Written in this way, we see that the chain is an ideal random walk of segments with g swollen monomers each. In Paper 1.vi, we claim that spin coating chains from an athermal solvent leads to chains that are stretched in comparison to Gaussian chains. The swelling described by Eq. 1.11 is one of the mechanisms proposed to be responsible for this stretching.

1.1.2 diblocks

Copolymers are polymer chains composed of more than one type of monomer [14]. Proteins are a type of copolymer that are important for the functioning of a large number of biological processes. They are constructed from a variety of amino acids, the order and type of which determines the shape and function of the molecule. While proteins are much more complicated than what can be produced synthetically, it is possible to produce molecules with a small number of blocks that have much practical and scientific significance [15, 16]. The simplest compound molecule is the diblock copolymer, as shown in Fig. 1.3(a). These are built from two linear chain polymers that are covalently bonded together at their ends. As with polymer solutions, there is in general an interaction energy associated with the two types of monomers that make up the two blocks. In contrast to the case presented in Section 1.1.1, we will only consider the case for which the interactions are such that the system prefers to phase separate [17].

The parameters sufficient to describe diblock copolymers in the bulk are N , f and χ . Here N is the number of monomers as before. The interaction energy between A and B monomers is characterized by

$$\chi = \frac{z}{kT} \left[\epsilon_{AB} - \frac{1}{2}(\epsilon_{AA} + \epsilon_{BB}) \right]. \quad (1.12)$$

ϵ_{ij} is the interaction energy between two nearest neighbour i and j molecules, it is a characterization of short ranged interactions; and z is the coordination number, or

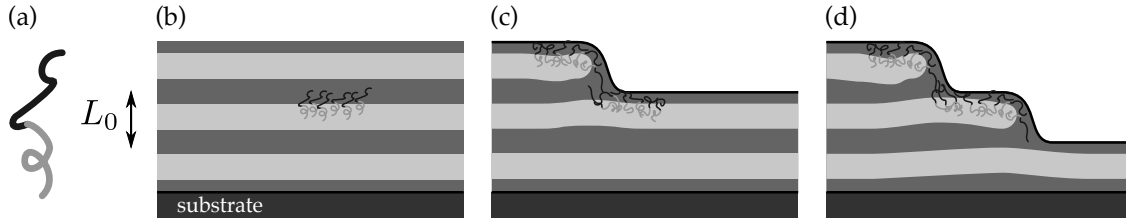


Figure 1.3: (a) A single diblock copolymer molecule with $f \approx 0.5$. (b) A portion of an ordered film with period L_0 and no defects. (c) If the film height is incommensurate with L_0 , step edges are formed, deforming the lamellar structure. (d) Two defects can interact, further deforming the lamellae.

the number of nearest neighbours for a given monomer. Defined as in Eq. 1.12, a positive value of χ suggests that phase separation is favoured energetically, to say nothing of the entropy for now. We typically refer to the diblock molecule as having an ‘A block’ and a ‘B block’. The fraction of the molecule that is composed of A monomers is f and the molecule contains $(1 - f)N$ B monomers. In this work, the only case that will be discussed is $f \approx 0.5$.

1.1.3 phase separation

In a system of diblock copolymers, phase separation can only happen on a length scale that is commensurate with the molecules. This is markedly different than the case for different chemical species that are not covalently bonded together. For a system composed of A molecules and B molecules that are not covalently bonded, the Flory-Huggins interaction energy [1, 2, 17, 18] is

$$\frac{\Delta F}{kT} = \frac{\phi_A}{N_A} \ln \phi_A + \frac{\phi_B}{N_B} \ln \phi_B + \chi \phi_A \phi_B, \quad (1.13)$$

where ϕ_i and N_i are the volume fractions and degrees of polymerization of the A and B molecules. The first two terms represent the mixing entropy of the system, while the last term represents the change in enthalpy upon mixing. If $N_A = N_B = N$, then the relevant parameter governing the phase behaviour of the system is χN . For values of $\chi N > 2$, the system phase separates, either by nucleation and growth or by spinodal decomposition [2, 18].

For symmetric diblock copolymers, the situation is different since the molecules cannot macrophase separate. In this case, the molecules minimize contact between A and B monomers by microphase separating into lamellae, shown schematically in Fig. 1.3(b). The condition for phase separation in this case is that $\chi N > 10$. When $\chi N \gg 10$, called the strong segregation regime, the diblock junction points are confined to 2-dimensional planes, and the lamellar spacing is set by a balance between the entropic cost of chain stretching and the enthalpic cost of having A and B blocks in contact. The lamellar spacing in the strong segregation limit [18] can be calculated by minimizing these contributions. It is found that the lamellar spacing $L_0 \approx b\chi^{1/6}N^{2/3}$ in this regime. When the molecules are not strongly segregated, the molecular junctions are not confined to planes, and the simple calculation used to compute the lamellar spacing cannot be used. In these cases of intermediate segregation there is a nonzero concentration of both species everywhere (in an ensemble average), and self consistent field theory (SCFT) can be used to predict concentration profiles and lamellar spacings [10, 19].

The simplest case of a lamellar diblock phase in confinement occurs when the molecules are placed near a flat solid boundary. It is typical that one of the blocks prefers the surface in this case. The preference for one of the blocks to be in contact with the surface directs the ordering such that the lamellae are oriented parallel to it [20]. If the film has a free surface and is not commensurate with L_0 , then this free surface breaks up into a collection of islands, is perforated with holes, or has a bicontinuous topography [21]. If the substrate prefers one block and the air prefers the other, the majority of the film surface has heights that are odd integer multiples of $L_0/2$. However, the film must continuously change height from $nL_0/2$ to $(n+2)L_0/2$. This height change, coupled with the connectivity of the diblock molecules results in a deformation of the lamellae in the vicinity of the transition region as shown in Fig. 1.3(c).

Since unperturbed lamellae minimize the free energy, these defects necessarily increase the free energy of the system. Understanding these defects on a molecular level was the motivation for Paper 2.iv. Experimentally, it is also possible to study the interaction between two of these step defects, shown schematically in Fig. 1.3(d). It is possible to equilibrate a single step edge, but placing a second step in the vicinity

of the equilibrated one disturbs the preferred morphology. Therefore, there is an energy cost associated with the step defects being near one another. This interaction is studied in Paper 1.iv.

1.2 entanglement

Thus far the structure and statistics of polymer melts have been discussed. However, to discuss the dynamics of polymer melts and solutions, it is necessary to introduce the concept of entanglements when the chains we are concerned with are large compared to the entanglement molecular weight, M_e . Entanglements arise out of the collective interactions between chains. At the root, they are a result of the fact that polymer backbones cannot pass through one another. It was noted in the introduction that equilibrated polymer chains perform random walks, which indicates that the pervaded volume of a specific (very long) polymer chain is nearly void of that polymer chain: $P_c \sim N^{-1/2}$. Assuming the mass density of PS to be $\rho \approx 1 \text{ g/cm}^3$, $M_w = 100 \text{ kg/mol}$ and $R_{ee} \approx 22 \text{ nm}$, we get

$$P_c = \frac{M_w}{\rho \mathcal{N}_A R_{ee}^3} \approx 0.02, \quad (1.14)$$

where \mathcal{N}_A is Avogadro's constant. That this fraction is so small indicates that most of the interactions a polymer chain experiences are with *other* chains. These interactions lead to entanglement phenomena.

Fig. 1.2 indicates how a polymer chain suffers from a mobility loss due to entanglements. In that figure, each of the heavy lines should be considered being only a part of a much longer chain. Thus, the black chain is trapped by each of the grey chains, and it is forced to wiggle back and forth more or less across the page. It is trapped in a *tube*. The concept of a polymer in a tube was developed by de Gennes [22] and Doi and Edwards [3], with various treatments to be found elsewhere [1, 2, 23]. The basic idea is that each of the entanglement points can be replaced with a coarse grained curvilinear tube of diameter d that encompasses the whole chain (see Fig. 1.4 where the grey segments represent the tube). In the reptation model, the polymer chain performs a one-dimensional random walk along the contour of this tube, this motion is called reptation. At $t = 0$, the chain is fully constrained, but as soon as the first

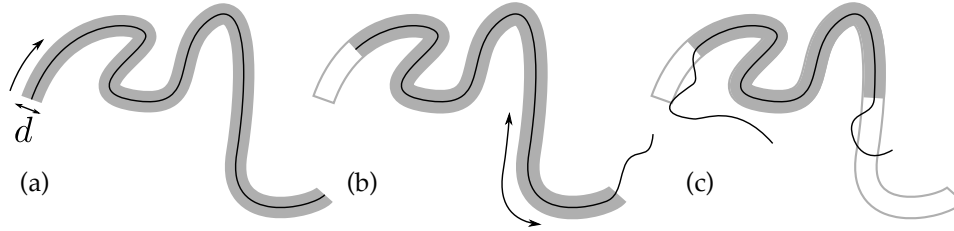


Figure 1.4: Schematic of the tube relaxation process. The tube diameter, d , is defined such that a random walking polymer chain with N_e monomers traverses an average end-to-end distance $d = bN_e^{1/2}$. (a) At $t = 0$, the tube fully envelops the chain. (b) After some time, the chain ‘reptates’ and some of the original tube (grey) is forgotten. (c) Both ends reptate back and forth until one end passes a point the other end has already visited, and the entire original tube is forgotten. The time taken for this to happen is called the reptation time, τ_{rep} .

step is taken, one chain end ‘abandons’ the tube, and ‘forgets’ that it was constrained.

As a possible experiment, consider a polymer melt to which a step strain is applied, and in which the remaining stress is measured as a function of time³. In the reptation model, a polymer system relaxes (*i.e.* the stress is lost) on the same time scale that an individual chain takes to lose memory of its original tube. As a polymer chain reptates back and forth, the chain ends continuously visit new portions of the tube. Segments of the original tube ‘disappear’ whenever one of the chain ends visits a portion that has not yet been visited, see Fig. 1.4. Relaxation of the entire tube takes place on a time scale called the reptation time, τ_{rep} , and at this time the polymer melt sustains no stress in the step strain experiment.

The quantity that determines the phenomenological tube diameter, d , was mentioned above, it is the entanglement molecular weight, M_e . The tube diameter is the distance between entanglements along a polymer chain. Since the equilibrium polymer chains are performing random walks, we have that $d \sim M_e^{1/2}$. The entanglement molecular weight is typically defined by analogy with rubber elasticity. In rubber elasticity theory [2], elasticity is due entirely to the entropic character of polymer chains. From Eq. 1.6, we have for the entropic free energy of a polymer chain with

³In an elastic solid, the stress would be constant in time. However, in a polymer melt the chains are not attached to one another and this stress decays as chains move past one another.

N segments

$$F_S(R) \approx kT \frac{R^2}{b^2 N}. \quad (1.15)$$

Stretching a polymer chain costs energy. Furthermore, since the free energy is quadratic, ideal polymer chains are Hookean springs. In a rubber, chains are permanently linked together through crosslinks. The macroscopic object is microscopically a network of many Gaussian strands with N_x monomers, where N_x is the number of monomers between crosslinks. Each network strand obeys Eq. 1.15. The force required to stretch a rubber band is equal to the sum of all the forces for stretching the polymer segments between the cross links. As can be found elsewhere [2, 18, 24], the stress, σ , required to impose a strain, ε , under the assumption of affine network deformations is given by

$$\sigma = \frac{\rho \mathcal{N}_A kT}{M_x} \left[(1 + \varepsilon) - \frac{1}{(1 + \varepsilon)^2} \right], \quad (1.16)$$

where $M_x = m_0 N_x$. The prefactor is the shear modulus

$$G_x = \frac{\rho \mathcal{N}_A kT}{M_x}, \quad (1.17)$$

which connects the microscopic M_x to the macroscopic force measured in a deformation experiment. For polymer liquids in which the chains are much longer than M_e , the time dependent response after a step strain, $\varepsilon(t) = \varepsilon_0 \Theta(t)$, with Θ a Heaviside function, displays a regime in time for which there is little change in the stress as a function of time. This stress plateau arises because on short time scales, the entanglements act like cross links. On time scales comparable to the reptation time, however, the tube is abandoned and the stress relaxes. Silly Putty offers a simple, direct way to observe these viscoelastic effects. Rolling Silly Putty into a ball and throwing it against a table, one observes an elastic bounce. However, if the ball is gently placed on the table, the mass flows under the influence of gravity on a time scale of some tens of seconds.

Measurements of M_e are typically made through the use of oscillatory shear experiments. In these experiments, some polymeric liquid is placed in between two

plates. On one of the plates, a sinusoidal oscillation with a frequency ω is imposed. The other plate is held rigidly in place, but the force on this plate as a result of the imposed deformation on the oscillating plate is measured. For the case in which the substance between the two plates is a purely viscous liquid, the stress is proportional to the strain rate, so the force lags the deformation by a phase of $\pi/2$. In the opposite case, for which the substance is a Hookean solid, the stress on the bottom plate is in phase with the imposed deformation.

Polymeric liquids are neither purely viscous nor elastic. In the oscillatory shear experiment described above, the phase lag is neither 0 or $\pi/2$ and it is frequency dependent. In practice [25], a spectrum of phase lags is collected, and are expressed in the form

$$\sigma(t) = \varepsilon_0 G'(\omega) \sin(\omega t) + \varepsilon_0 G''(\omega) \cos(\omega t), \quad (1.18)$$

where G' and G'' are the in- and out-of-phase portions of the measured stress; respectively, they represent the elastic and viscous portions of the response. The functions G' and G'' are routinely used in the study of rheology in order to test molecular theories of polymer viscoelasticity [3, 23]. In particular, an integral involving the function $G''(\omega)$ can be used to determine the plateau modulus,

$$G_e = \frac{2}{\pi} \int_{-\infty}^{\infty} d\omega \frac{G''(\omega)}{\omega}. \quad (1.19)$$

This expression for G_e can then be related to M_e by analogy with Eq. 1.17. This is a measurement of M_e using a dynamical experiment in a linear response regime.

In a collection of works by Fetters and co-workers [5, 6], packing models for the entanglement molecular weight of a polymer melt are summarized (see references therein). In these packing models, the entanglement molecular weight is predicted based on the ideas of Eq. 1.14. The argument says that the entanglement molecular weight is determined by the condition that $P_c \sim 0.5$; this value⁴ of P_c corresponds to the state for which the molecule is interacting with itself as much as it interacts with other chains. If entanglements arise out of interactions with other chains, then this criterion says that once a polymer chain is interacting with enough *other* molecules, it

⁴The exact value of P_c that ‘defines’ the entanglement concept is model dependent.

should display properties derived from entanglement models, such as the tube model described above.

Fetters and co-workers collected κ (from small angle neutron scattering as in [12], see Eq. 1.5) and M_e values (from oscillatory shear spectra) from a large number of references for different polymers. Using this data for more than 25 different polymers, they found a relation for the entanglement molecular weight in terms of material parameters:

$$M_e \sim \frac{1}{\rho^2 \kappa^3} \sim \rho p^3, \quad (1.20)$$

where p is the packing length of a polymer species: $p = \rho \mathcal{N}_a / \kappa$. The value of expressing the entanglement molecular weight in terms of the packing length is geometric in nature. In [6], it is shown that the packing length has a monomeric interpretation. If a monomer is thought of as cylinder with circular cross section of area r_m^2 and length l , then $p \propto r_m^2 / l$. Thus, if the monomer is skinny, then M_e is small, as may be intuitively clear.

1.2.1 viscosity

The presence of entanglements plays an important role in the observed behaviour of long chain polymer systems. If we apply a constant shear stress to an entangled polymer melt and wait for times much longer than the reptation time, viscous flow is observed. The observed viscosity is influenced by entanglements. On the basis of the reptation model (see Fig. 1.4), we can estimate the viscosity of a long chain polymer system [2].

Since the chain is constrained to live inside the tube, it performs a random walk along the tube's length. The entire chain experiences a friction that is a result of all monomers moving against the melt. With ζ the friction coefficient between monomers, the chain has a friction coefficient $N\zeta$, and thus a curvilinear diffusion coefficient $D_c = kT/N\zeta$ using the Einstein relation. The primitive path length of the tube, defined as its curvilinear length, is estimated as $L = d \frac{N}{N_e}$. Using $d = bN_e^{1/2}$, we have that $L = bN/N_e^{1/2}$. The reptation time is defined as the time taken for the chain to

diffuse out of the original tube:

$$\tau_{\text{rep}} = \frac{L^2}{D_c} = \frac{b^2 \zeta N^3}{kT N_e}, \quad (1.21)$$

with the important result that $\tau_{\text{rep}} \sim N^3$ according to the reptation model. The viscosity of a liquid can be estimated as the product of the plateau modulus and the relaxation time, so

$$\eta \approx G_e \tau_{\text{rep}} \sim \frac{N^3}{N_e^2}, \quad (1.22)$$

In experiments [4] it is seen that the viscosity is slightly different from the prediction of the reptation arguments, $\eta \sim M_w^{3.4}$. The relationship shown in Eq. 1.22 is tested as part of the investigations presented in Papers 1.i, 1.ii and 2.i – 2.iii.

1.2.2 crazing

When a glassy material is put under strain, it will elastically deform, with the molecules being moved slightly out of their preferred intermolecular positions. If the material is deformed beyond a certain level, the yield point, molecules begin moving past one another, even in the glassy state [26]. For molecular glasses, the extent to which plastic deformation can occur is small as compared to the strains that long-chain polymer glasses can sustain; molecular glasses fail (*i.e.* break) soon after the yield point. On the other hand, long-chain polymer glasses can extend much further [26, 27] than short chain systems because they are entangled [28, 29].

In the case of a polymer film, one experiment that can be performed is to freely suspend the film with thickness h across a gap, as in Fig. 1.5(a), and to uniformly stretch it beyond the yield point [24, 30–34]. During the stretching, defects are formed by locally thinning the film into a neck, these defects are called crazes, and have thickness $h_c < h$ as seen in Fig. 1.5(b). Inside a craze drawn from a film with equilibrated polymer chains, the chains are highly deformed, with the random walk statistics invalidated. Crazes grow in width by drawing new material from the undeformed film until it is easier to bring in new material rather than continuing to deform the chains at the edge of the craze [33, 35]. As a result, material in the middle of a well developed

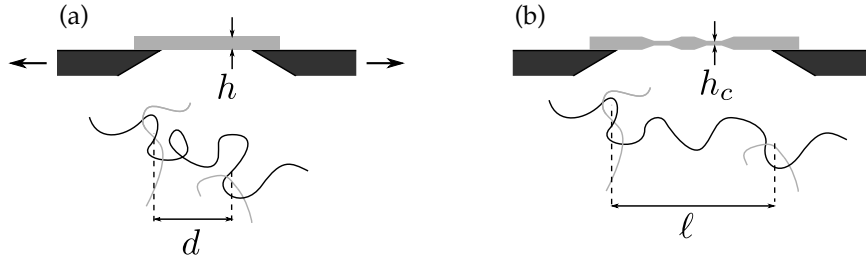


Figure 1.5: Schematic of the crazing process in a film with equilibrated chains. (a) A film with thickness h is strained in the film-plane direction. Before straining, entanglement points are a distance $d \sim N_e^{1/2}$ apart. (b) After crazing, there are crazes distributed through the film, with thickness h_c . The entanglements are now a distance $l \sim N_e$ apart.

craze does not deform as a result of new material being brought into the craze near the undeformed portion of the film.

In a crazing measurement, entanglements act like fixed cross links, as has been discussed by Donald and Kramer (experiments [28, 31, 32, 36]) and by Rottler and Robbins (simulations [37, 38]). In the undeformed material, the end-to-end distance of entanglement strands scales according Eq. 1.4: $d \sim N_e^{1/2}$. The stressed material in the craze contains highly oriented chains, and the distance between entanglement points in the craze is linear in the entanglement molecular weight: $l \sim N_e$, so $d/l \sim N_e^{-1/2}$ (see Fig. 1.5). In Papers 1.v and 1.vi, and in references [33–35], it is argued that the draw ratio of the molecules, d/l , is the same as the draw ratio of the length of craze compared to the length of the undeformed material that went into making the craze. By making such an argument, it is possible to connect the measurable heights (craze and undeformed film height) to the molecular quantity N_e :

$$\left(\frac{h_c}{h}\right)^2 \sim N_e^{-1} \sim M_e^{-1}. \quad (1.23)$$

This relationship assumes that Gaussian chain statistics are valid, and is used extensively in the analysis of Papers 1.v and 1.vi.

1.2.3 confinement

Thus far, all the concepts surrounding entangled chains have had to do with polymer chains in the bulk. The Fetters work [5, 6] puts on firm footing the idea that interactions with other chains in the melt dominate the entanglement phenomena observed. One way of testing this idea is by putting chains near an interface. For chains near an interface, it was argued by Silberberg [39] that for an ideal random walk the chain segments encountering a non-adsorbing interface are simply reflected back into the melt. The result is that chain segments that would have explored space beyond the barrier in its absence are reflected back. This reflection principle has a major effect on the packing of chains that encounter an interface, since they are forced to share space with fewer other chains as compared to the bulk. Brown and Russell [40] have discussed this reflection principle in light of the chain packing arguments. They conclude that if the reflection principle and packing arguments are correct, then there must be a marked reduction in the entanglement density near an interface. Their prediction is that entanglements with other chains occur a factor of three times less often near an interface.

There have been a number of measurements reported in which the properties of polymer chains near interfaces are investigated. Shin, Russell and co-workers [41] reported an enhanced mobility of polymer chains through nanoporous alumina. Their results indicated a capillary rise time that scales with $M_w^{1.5}$, which they attributed to a viscosity scaling $\eta \sim M_w^{1.5}$. Bodiguel and Fretigny [42] also observe a marked decrease in the viscosity of thin polymer films dewetting off of a liquid substrate, finding a stretched exponential dependence of the viscosity with film thickness, $\eta = \eta_0(1 + \exp[-(z/R_g)^{3.4}])$. In their follow up work [43] Bodiguel and Fretigny argued that since $R_g \sim M_w^{1/2}$, for small thicknesses their empirical observations would be consistent with $\tau_d \sim M_w^{1.7}$. This exponent is close to that observed by Shin and co-workers. Rowland [44] and co-workers also observed an enhanced dynamics of thin polymer films during nano-imprint lithography when the films became less than R_g . While each of these results suggests an enhanced dynamics in confinement, O'Connell and McKenna [45, 46] have used a microbubble inflation technique to measure the viscoelastic properties of freestanding polymer films. In their measurements, they find that the rubbery plateau compliance (related to the inverse of the modulus of

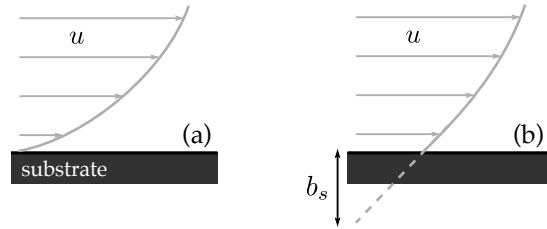


Figure 1.6: Schematic of hydrodynamic velocity profiles. (a) The no-slip case has velocity $u = 0$ at the interface while, (b) a slippery liquid-substrate interface has a slip length, b_s , over which the fluid velocity profile linearly extrapolates to zero. The liquid-substrate interface with non-zero slip length has liquid sliding across the solid surface.

Eq. 1.17) was reduced. Their films are stiffer than unconfined films, suggesting a larger entanglement density (smaller M_e). These results seem to be in contradiction with the enhanced mobility reported elsewhere.

Concerning the conformations of polymer chains near interfaces, Si and co-workers have performed crazing measurements [34] (as are presented in Papers 1.v and 1.vi, and shown schematically in Fig. 1.5) that probe polymer chain statistics in thin films. Briefly, a thin glassy film is stretched to just before the point of failing. This produces necks in the material (as when a grocery bag is stretched) that are surrounded by undeformed material. Comparing the thickness of the neck and that of the undeformed film gives information about the entanglement network, as will be discussed in detail later. The thin films studied there had a range of thicknesses extending from below to well above the unperturbed radius of gyration. As such, these films were well suited for an investigation of the ideas presented by Silberberg [39] and their effects on the entanglement density [40]. Si and co-workers observed that the extension ratio was consistent with a reduced interchain entanglement density near uncrossable surfaces.

When fluids flow past a solid substrate, it is possible that they can slide across it [47]. One characterization of the process of fluids sliding across a surface is called the slip length (schematically shown in Fig. 1.6), which is defined as the distance below the substrate at which the fluid velocity linearly extrapolates to zero. This slip effect will be important if the slip length is comparable in size to the fluid system under study. For polymer liquids on solid substrates, the slip length can be in the

range of one hundred microns [48]. Where polymers are concerned, a simple argument due to de Gennes indicates that the slip length, b_s , scales with the viscosity of the polymer melt [49],

$$b_s \sim \frac{N^3}{N_e^2}, \quad (1.24)$$

see Eq. 1.22. In a following study on the boundary conditions of liquids flowing past a solid surface, Bäumchen and co-workers [50] observed slip lengths that scaled according to the molecular weight dependence shown in Eq. 1.24. They noted, however, that the bulk value of M_e could not account for their data. A larger than the bulk value of M_e was needed to account for their observations, consistent with the arguments of Brown and Russell [40].

The results discussed above indicate that there is still much to be learned about polymers near interfaces. Paper 1.vi deals with aspects of polymer chains near interfaces. There, we use thin polymer films with thickness in the range of R_g . The films are thus strongly influenced by the polymer chain statistics near a reflecting surface as described by Silberberg: in this case, the polymer-air interface is the reflecting one. We then place two equilibrated reflecting interfaces in contact by creating a bilayer polymer film. Upon annealing the bilayer films above T_g , we see that the chains formerly at the air-polymer interface relax by exploring volume that was previously unavailable to them in the opposing film. This relaxation occurs on a time scale that is faster than one bulk reptation time. The work contained in that manuscript also deals with some aspects of the chain statistics in a non-equilibrium film prepared by spin coating, which is the method most commonly used to explore the physics of polymers in confinement. Papers 1.i, 1.ii and 2.i – 2.iii are also concerned with the mobility of polymers in thin films on a substrate. We have been motivated to undertake these experiments in light of the fact that few tools exist that are able to characterize the rheological properties of polymer chains in confinement.

1.2.4 non-equilibrium networks

The previous subsections have demonstrated that entanglement networks are of paramount importance in the determination of polymer properties. Understanding these

properties (*e.g.* the melt viscosity, or the mobility in confinement) seems often to be determined by an ability to understand the entanglement network. As this is the case, researchers comparing their results must be concerned with the state of their networks, and whether or not they are in equilibrium.

Several decades ago, Croll noted [51] the importance of residual stresses in air-dried polymer coatings. The residual stress arises because polymer solutions go through a glass transition at non-zero solvent content [52], even though the solvent continues to evaporate after the transition. If there is adhesion of the molecules at the substrate, the volume loss can only occur through a reduction of the film thickness. The polymer molecules thus become compressed in the film normal direction since large scale molecular rearrangements do not occur in the glassy state. The equilibrium state in a film much thicker than the unperturbed radius of gyration is for the molecules to perform uncorrelated random walks. A uniform compression of all the polymer molecules results in a preferred orientation, thus there is a stress.

As spin-coating from polymer solutions (discussed in Section 1.1.1) is the dominant method by which thin films are prepared in the study of polymer confinement, it is important to know whether the studied properties represent true equilibrium phenomena, or if they are a result of some driving force toward equilibrium. Reiter and co-workers have been involved with many studies concerning the nature of as-cast polymer films [53–57]. In these works, it is clearly demonstrated that either annealing (heating above T_g) or ageing (heating below T_g) has a significant impact of various dewetting or destabilization processes. In the annealing studies by Steiner and co-workers [56, 58] and also by Li and co-workers [59], it is reported that the viscosity of a polymer film takes up to five orders of magnitude longer than the bulk reptation time to establish a plateau in the viscosity of thin polymer films. These observations in part motivated the annealing studies of polymer entanglement networks presented in Paper 1.vi. There we find that annealing 100 nm films on mica for times of order one bulk reptation time is sufficient to observe a plateau in the neck-to-film heights measured in a crazing experiment. We suggest that a surface effect not operative in our experiments might be responsible for the observed discrepancy between our results and those reported by others.

In Paper 2.v, we report on another aspect of polymer thin film studies that has

attracted attention in light of the non-equilibrium phenomena discussed here. Since the seminal work of Keddie, Jones and Cory [60], many researchers have reported measurements of glass transition reductions in thin polymer films both supported [61] and free standing [62], *i.e.* with one and two free interfaces. In [63,64], it was reported that no T_g reduction was observed in thin films with thickness down to 10 nm. The authors suggested that the discrepancy was due to sample preparation artefacts not considered by other authors (*e.g.* [60–62]). Paper 2.v negates the idea that glass transition reductions can be explained by the presence of sample preparation artefacts.

1.2.5 blends

In order to elucidate the importance of entanglements, a final aspect we discuss is the effect of adding various small molecular weights on the entanglement network. Thus far, we have only considered the physics of these entanglement systems when all the chains are much longer than the entanglement strands, $M_w \gg M_e$. If some chains in the network are smaller than, or on the order of the entanglement mesh size, then adding small chains must have the effect of diluting the entanglements in the network. In Paper 1.v, we discuss the idea that not all entanglements are equally effective at carrying network stress, thus in the crazing measurement, these small chains will not participate and the craze will be consistent with one that grew from a network with fewer entanglements. Similar work was carried out by Kramer and co-workers [30], however there, the authors were focused on networks diluted by chains with $M_w \ll M_e$, while we used molecular weights as large as $\sim 5M_e$ over a large range of compositions. Our results indicated the importance of the idea that chains slightly above M_e cannot necessarily be treated as ‘entangled’.

1.3 surface tension

Just as an ideal gas resists a change in volume, $\delta W = -PdV$, it generally costs energy to increase the surface area of a solid or a liquid: $\delta W = \gamma dA$. In these expressions: W is the work; P, V are the pressure and volume; and A is the surface area of the system. γ is the surface or interfacial tension, and it is the driving force of all the fluid flows examined in detail in this thesis. To understand why it costs energy to

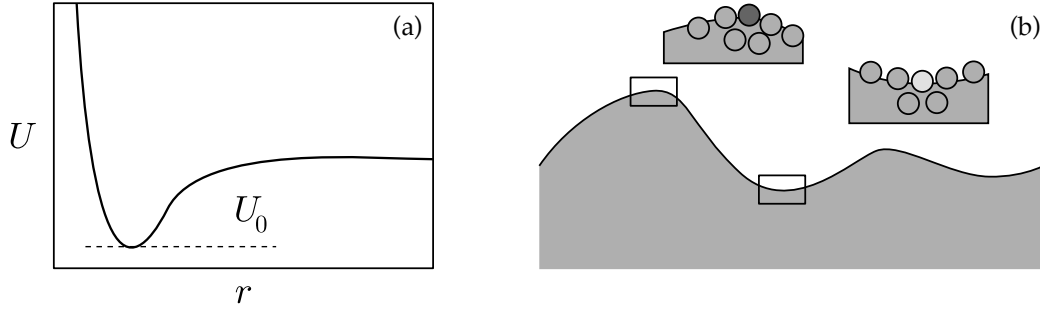


Figure 1.7: (a) Schematic of an intermolecular interaction potential, with a repulsion at short distances, and a long range attraction. (b) Schematic of a possible liquid-air interface. Boxed regions are blown up and a few molecules near the interface are shown. The dark molecule is in a higher energy state than the light one.

create a surface we can consider the case of a liquid in which all the molecules are non-polar. For non-polar molecules, there is typically [9] a long range van der Waals interaction acting between the molecules:

$$U_{vdw}(r) \sim -\frac{1}{r^6}. \quad (1.25)$$

This interaction arises because of the fact that atoms and molecules are polarizable [9] and the instantaneous dipole moments of one molecule induce a dipole moment in neighbouring molecules, resulting in an attraction. On the other hand, when molecules come too close to one another, their electron clouds begin to overlap, and there is an electrostatic repulsion. This is often empirically associated with a different power law, $U_e(r) \sim +1/r^n$, with $n > 6$. The result is a total interaction potential between molecules that may be schematically depicted as in Fig. 1.7(a). The molecules in the liquid tend to be found at distances from each other described by the potential well. If half of the molecules in our system are removed to infinity, then each molecule on the surface finds itself with approximately U_0 of extra energy [8], associated with its neighbours being found in the plateau of Fig. 1.7(a). Thus, if surfaces cost energy, then nature should want to minimize the surface area.

In addition to the energy considerations made surrounding Eq. 1.25, it is also true that in polymeric materials, there is an entropic contribution to the surface tension that is dependent on the molecular weight. As described by Dee and Sauer [65,66], the

dominant entropic contribution to the surface tension is from the free volume available to chain segments, while the entropic cost associated with configurational degrees of freedom described by Silberberg [39] is negligible. For the high molecular weights used here, the molecular weight dependence of the free volume is determined by the density of chain ends. Dee and Sauer [65, 66] note that the molecular weight dependence of the surface tension is well described by a function of the form $\gamma = \gamma_\infty(1 - K/M_n)$ in this regime. In this expression γ_∞ is the surface tension at infinite molecular weight and K is a constant. Based on their data [65] for PS at 227 °C, we estimate that over the range of molecular weights $15 < M_n < 1000$ kg/mol (representative of the range used here), surface tensions change by a factor of about 3%. Since the error on a typical measurement of the capillary velocity, γ/η with η the viscosity, is in the range of 20% as described in the next chapter, and because the viscosity of a polymer melt changes by more than 5 orders of magnitude over the same range of molecular weights, this variation in the surface tension is negligible.

Given that surfaces cost energy, we see that nature tends to minimize the surface area between two immiscible fluids (oil and water, for example). In addition to the area minimization, there is also a pressure jump across a curved surface, and we can evaluate it by computing the work done on completing an infinitesimal change in the radius of a spherical volume [8]. If a spherical volume changes its radius by an amount dR , then the work done is

$$\delta W = -P_o dV_o - P_i dV_i + \gamma dA , \quad (1.26)$$

where the subscript ‘*o*’ is for outside and ‘*i*’ is for inside the bubble. By conservation of volume, $dV_o = -dV_i$, and using the spherical geometry we have

$$\delta W = -(P_i - P_o)4\pi R^2 dR + \gamma 8\pi dR . \quad (1.27)$$

At equilibrium $\delta W = 0$ such that using $\Delta P = P_i - P_o$, the pressure jump on traversing an interface is,

$$\Delta P = \frac{2\gamma}{R} , \quad (1.28)$$

where we now interpret R as the radius of curvature. Eq. 1.28 tells us that the curvature of an interface implies a pressure, this type of pressure is usually referred to as the *Laplace* pressure [8]. In Fig. 1.7(b) is shown a surface with an arbitrary surface topography, a generalization of Eq. 1.28 takes into account the two radii of curvature, $R^{-1} \rightarrow R_1^{-1} + R_2^{-1}$, and for a surface topography dependent on x only, $h = h(x)$, the curvature is $R^{-1} = -\partial_x^2 h / [1 + (\partial_x h)^2]^{3/2}$ [67]. Eq. 1.28 implies that the regions that are concave down should have higher pressure than the regions that are concave up. Thus, the material under the darkened particle in Fig. 1.7 experiences a higher pressure than the region under the lighter particle. This implies the existence of a pressure gradient, and where there are pressure gradients in liquids, there can be a flow.

1.4 hydrodynamics

This section combines the principles discussed in some of the previous sections in order to understand how liquid polymers flow in certain thin film geometries. There are two assumptions that will greatly simplify the analysis. First, the films are highly viscous, such that inertial effects are negligible. Second, the films are thin in comparison to typical lateral length scales, this will allow us to neglect certain components of the flow. Hydrodynamic treatments of flows typically start with the Navier-Stokes equation in three dimensions and the incompressibility constraint [68]:

$$\rho \left(\frac{d\mathbf{u}}{dt} + \mathbf{u} \cdot \nabla \mathbf{u} \right) = -\nabla P + \eta \nabla^2 \mathbf{u} , \quad (1.29)$$

$$\nabla \cdot \mathbf{u} = 0 , \quad (1.30)$$

where $\mathbf{u} = (u, v, w)$ is the velocity vector, with u, v, w the x, y, z components of the velocity field. Eq. 1.29 is a statement of the conservation of momentum: the left hand side is the temporal derivative of the momentum per unit volume, with the right hand side being the force per unit volume (not including any body forces, such as gravity). The Reynolds number determines the relative importance of the inertia and the force.

It is defined as

$$\text{Re} = \frac{\rho u_o l_o}{\eta} , \quad (1.31)$$

where u_o and l_o are typical velocity and length scales of the flow. Recasting Eq. 1.29 in dimensionless units using these scales, the Reynold's number multiplies the left hand side. Typical Reynold's numbers encountered in the experiments discussed here are $\text{Re} \sim 10^{-13}$ (see Papers 2.i and 2.ii), such that we can neglect the inertial terms of the Navier-Stokes equation.

Neglecting the left hand side of Eq. 1.29, we are left with

$$0 = -\nabla P + \eta \nabla^2 \mathbf{u} , \quad (1.32)$$

which is typically referred to as the Stokes equation. In Papers 1.i, 1.ii and 2.i, 2.ii, we will consider the case in which the topography is not dependent on y , so we assume that $v = 0$ everywhere. Furthermore, we assume that the films are thin in comparison to lateral length scales, that is $h_o \ll x_o$ where h_o is the typical film height and x_o is the typical length scale of the flow in the lateral direction. As such, we can assume that w is negligible and we have

$$0 = -\partial_x P + \eta \partial_z^2 u . \quad (1.33)$$

As boundary conditions we assume that $u(0) = 0$ (the no-slip condition, see Fig. 1.6(a)) and we also assume that there is no stress at the fluid-air interface (the viscosity of air is many orders of magnitude less than that of the polymer liquids we consider), therefore $\partial_z u|_h = 0$ where h is the distance between the substrate and the fluid-air interface. Using the no-slip and no-stress boundary conditions, we integrate Eq. 1.33 and find a parabolic velocity profile:

$$u(z) = \frac{\partial_x P}{2\eta} (z^2 - 2hz) . \quad (1.34)$$

The pressure is provided by the curved interface, such as is shown in Fig. 1.7(b). If we assume small height gradients, then $P \approx -\gamma \partial_x^2 h$. By integrating the incompressibility

constraint and using the parabolic velocity profile, we find that

$$\partial_t h + \frac{\gamma}{3\eta} \partial_x (h^3 \partial_x^3 h) = 0 . \quad (1.35)$$

We have thus derived the equation of motion for an air-fluid interface under the influence of surface tension whose flow is mediated by the viscosity. Eq. 1.35 is an example of an equation which is derived from the *lubrication* approximation, where the lubrication approximation assumes that flow in the vertical direction is much smaller than the flow in the horizontal direction. Eq. 1.35 is more formally derived in [67, 68], and is also derived in Papers 2.i and 2.ii.

For further analytical treatments of equations such as 1.35, it is convenient to non-dimensionalize through $h = h_o H$, $x = x_o X$, and $t = \frac{3\eta x_o^4}{h_o^3 \gamma} T$. H , X and T are dimensionless variables and h_o and x_o are the typical height and length scales of the problem. Making this change of variables, we have the dimensionless form of the evolution equation

$$\partial_T H + \partial_X (H^3 \partial_X^3 H) = 0 . \quad (1.36)$$

A particular feature of this type of equation is that can be reduced to a self-similar form by introducing the variable

$$U = \frac{X}{T^{1/4}} = \left(\frac{3\eta}{\gamma h_o^3} \right)^{1/4} \frac{x}{t^{1/4}} . \quad (1.37)$$

Making this change of variables, we are left with a differential equation of a single variable and we have $F'U = 4[F^3 F''']'$ (see *e.g.* [69]), where we have defined $F(U) = H(X/T^{1/4})$. Thus, if the geometry of our experimental design admits a self-similar solution, then recasting our time dependent data in the self-similar variable U should collapse all of the data onto a single curve. This type of self-similar evolution is experimentally observed in Papers 1.ii, 2.i and 2.iii (the latter in cylindrical coordinates, with a slightly different self-similar variable).

1.4.1 steps

As discussed above, Papers 1.i, 1.ii and 2.i, 2.ii deal with the preparation, annealing and analysis of stepped PS films. In Fig. 1.8(a) is schematically shown an example of such a film, prepared with a bottom layer of thickness h_1 and a step with height h_2 . The Laplace pressure is large in the top corner since $\partial_x^2 h \rightarrow -\infty$. On the other hand, where the step meets the lower film the opposite is true, $\partial_x^2 h \rightarrow \infty$. Away from these corners, the Laplace pressure is 0. As such, there is a localized region of high Laplace pressure gradients in the as-prepared sample. When this type of sample is heated to above T_g , there is a flow that tends to smooth the pressure gradients. After a short period of annealing (in comparison to our experimental annealing times), these large gradients smooth out to a considerable extent. The top corner ejects material in both directions, resulting in a bump of material to its ‘right’ (see Fig. 1.8(a) after annealing for the definitions of ‘right’ and ‘left’). By the same argument, the bottom corner takes material from the top one, but it also takes material from the ‘left’, resulting in the formation of a dip.

The bump and dip regions are, for the entirety of the step profile evolution, the regions of the highest and lowest Laplace pressure. However, the positions of maximal (absolute) height are not the positions of maximal pressure. Thus, while the bump has material flowing out of it, an approximately equal amount of material flows into it, resulting in a self-similar profile that levels with time. We have also performed numerical simulations of Eq. 1.36 (described in Paper 2.i). These dimensionless profiles can be stretched to fit onto the measured ones. By inspection of Eq. 1.37, we see that comparison of the experimental and computed profiles offers a measurement of the capillary velocity, γ/η , this determination is described more fully in Papers 1.ii and 2.i, and is also described in Section 2.3.

We also characterize the measured profiles by the contour length in excess of a flat film:

$$\Delta L \approx \frac{1}{2} \int dx (\partial_x h)^2 . \quad (1.38)$$

This has the relevant physical interpretation of being the excess free energy of the system; γL is the surface energy per unit width in the y -direction. To make progress

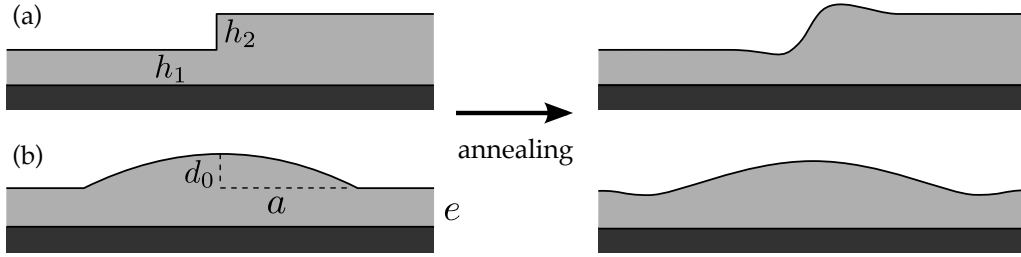


Figure 1.8: (a) Schematic of an as-prepared stepped film with bottom layer thickness h_1 and a step of height h_2 . (b) Schematic of a spherical cap on an identical film. The film has thickness e and the spherical cap has maximum height d_0 and base radius a . This figure adapted from the graphical abstract of Paper 2.i.

in understanding the time dependence of the energy dissipation, we take advantage of the self-similarity solutions, $H(X, T) = F(U)$. In doing so, we find that the energy decreases as $\gamma\Delta L \sim t^{-1/4}$, and depends on an integral involving $F(U)$. The integral in $F(U)$ contains the geometric dependence of the evolution. We have found in Paper 1.ii that our data for all times, molecular weights and geometries (different h_1, h_2) fall onto a master curve, thus demonstrating the usefulness of stepped films for investigations of confined polymer systems.

1.4.2 bumps

When a drop of liquid is placed on a substrate, as in Fig. 1.8(b) with $e = 0$, the equilibrium state is generally for the liquid to form a spherical cap with some contact angle at the surface, $\tan \theta_0 \sim d_0/a$ when $a \gg d_0$. By balancing surface tension forces or by computing the work differential at equilibrium [8, 70] we can find a relation between the equilibrium contact angle and the surface and interfacial tensions of the problem: $\gamma \cos \theta_0 + \gamma_{SL} = \gamma_{SV}$. Here as before, γ is the liquid-vapour surface tension, γ_{SL} is the interfacial tension between the solid and the liquid, and γ_{SV} is the solid-vapour surface tension. If a drop is placed onto the substrate and the contact angle is not equal to θ_0 , then the surface tensions are not balanced, and there is a driving force for flow. In the particular case where $\theta_0 = 0$, there is complete spreading. In these situations, any droplet of liquid placed on the substrate, no matter the contact angle, will eventually form a thin film of liquid on the substrate. The law governing

the flow from a spherical cap to a thin film is called Tanner's Law [71], and the flow in this case proceeds such that $d_0 \sim t^{-0.2}$.

One way of ensuring that the equilibrium contact angle of a system is $\theta_0 = 0$ is to make the substrate out of the same material as the liquid droplet. We carried out such a study, and it forms the basis of S. Cormier's MSc thesis [72]. Details of the experiments can be found in that thesis and in Paper 2.iii. There is a significant correspondence between the spherical cap experiment and the stepped film levelling one. Specifically, this is the case in terms of the analysis making use of self-similarity concepts. It is for this particular reason that the discussion concerning the levelling of spherical caps is retained here. In Fig. 1.8(b) is shown a schematic of the second geometry in which we study surface tension driven flows. In these experiments we place a polymeric spherical cap onto a spin coated polymer film, with the cap and the film made from the same polymer. We can easily change the height, e , of the resulting films while keeping the droplet section, d_0 and a , roughly constant. In doing so we change the aspect ratio of the droplet, $d_0(t=0)/e$, which as is described in Paper 2.iii, has a remarkable effect on the evolution of $d_0(t)$.

When this cap-and-film system is heated above T_g , a flow proceeds immediately at $r = a$, since this is the only place in the system with a curvature gradient. For the same reason that a dip is formed near the bottom corner of a stepped film, a dip is also formed in the region $r = a$, where r is the radial distance from the centre of the droplet. The driving forces and damping mechanisms in this case are the same as for the stepped film system, *i.e.* surface tension drives a flow mediated by the viscosity. The difference is in the geometry, as such, the differential equation governing the height $h(r, t)$ is [68]

$$\partial_t h + \frac{\gamma}{3\eta} \frac{1}{r} \partial_x \left[r h^3 \left(\partial_r^3 h + \frac{1}{r} \partial_r^2 h - \frac{1}{r^2} \partial_r h \right) \right] = 0 . \quad (1.39)$$

This equation of motion can also be non-dimensionalized, and we use $d = h_o D$, $r = h_o R$ and $t = \frac{3\eta h_o}{\gamma} T$; d is the height in excess of the undisturbed film: $h = e + d$, and we use $h = h_o H$. As it is only the geometry of this system that is different from the stepped films discussed in the previous section, it is reasonable to guess that self-similar solutions for this equation also exist. In Papers 2.i and 2.iii, we argue the

existence of self-similar solutions of the form

$$G(W) = \frac{H(R, T) - E}{H(0, T) - E}, \quad (1.40)$$

$$W = \frac{R}{[H(0, T)^3 T]^{1/4}}. \quad (1.41)$$

In the limiting case for which the droplet height is much larger than the film height, one expects a behaviour that is close to Tanner's law. In this case, the viscous dissipation is dominated by flow near the contact line. The reason for this is that the excess energy in the spherical cap is dissipated where there are flow gradients. Large flow gradients lead to high dissipation. Given that the no-slip condition is typically valid at the solid-liquid boundary, while the no-stress condition is operative near the liquid-vapour boundary, we see that flow gradients in the z -direction can get quite large near the contact line. The gradients are correspondingly much smaller at the centre of the droplet.

When the droplet size is much smaller than the film height, the flow gradients that were large in the Tanner limit are relieved by the presence of a film under the droplet. Therefore, the flow gradients near the contact line are of comparable size to the ones near the centre of the droplet. Since Tanner's droplet spreading, with $d_0 \sim t^{-0.2}$, is dominated by dissipation at the contact line, we expect to see a different behaviour when the droplet is small in comparison to the film height. As explained in Paper 2.iii, by systematically changing the bottom film height in relation to the droplet size, we smoothly transition from Tanner's spreading for a thin film, to a different spreading power law, $d_0 \sim t^{-0.5}$ for small droplets on thick films. To explain these observations, we again make use of self-similarity principles. Whereas in the case of a stepped film, we used the contour length integral (Eq. 1.38), we can write down the volume in excess of the film with height e :

$$V \sim \int dr r d(r, t). \quad (1.42)$$

Making use of the self-similarity described by Eqs. 1.40 and 1.41, we obtain an expression for the height of the droplet with time: $(d_0/e)^2(1+d_0/e)^3 \sim t^{-1}$. This expression predicts that limiting values of d_0/e result in two different power laws: $d_0 \sim t^{-0.2}$

for relatively small e ; and $d_0 \sim t^{-0.5}$ for relatively large e . Where the values of d_0/e are not in the limiting regimes, a smooth transition between the two power laws is predicted. All of these predictions are in agreement with the observations made in the experiments. Details are found in Papers 2.i and 2.iii and in [72].

1.4.3 rings

The final surface tension driven flow that is encountered in this thesis is one in polymer ring sections on a substrate, see Paper 1.iii. The rings are prepared by a unique spin coating process that involves the placement of a methanol bath on a Si substrate, into which a drop of polymer solution (PS dissolved in toluene) falls. Having prepared the rings, we observe a surface tension driven flow that causes the toroidal caps to break up into a collection of droplets on a substrate.

To understand why this flow proceeds, we consider a linear fluid jet. The fluid jet is modelled as an infinitely long cylinder of fluid, with radius R . The main idea is to see whether a sinusoidal perturbation of this surface will decrease the surface area. If the surface area is decreased by a perturbation, then the perturbation should grow, otherwise the cylinder is stable. By computing the surface area of the cylinder after a sinusoidal perturbation has been applied, and conserving volume, we find that if the wavelength, λ , satisfies $\lambda > 2\pi R$, then the perturbation is unstable [73]. This instability is called a Plateau-Rayleigh instability.

In a toroidal jet, it is necessary that the wavelengths are discretized due to the periodic geometry [74]. The circular geometry also provides for an alternate energy minimization route. In addition to a Plateau-Rayleigh instability, the ring can also reduce its area by shrinking the torus hole (while conserving volume and maintaining a circular cross section). In Paper 1.iii, this interplay between the breakup instability and the shrinking one is discussed in more detail.

Chapter 2

Experimental Details and Data Analysis

2.1 sample preparation

With the exception of the project concerning the breakup and evolution of toroidal polymer caps on Si substrates (Papers 1.iii and 1.iv), all of the experiments presented in this thesis began with thin films of PS on Si or mica substrates. With the exception of the use of the block co-polymer PS-PMMA (polymethyl methacrylate) all of the polymers used were PS. Molecular weights ranged from 5.5 kg/mol to 1140 kg/mol.

In the spin coating process, a droplet of polymer solution (here, 1-5wt% in toluene is typically used) is placed onto a substrate which is on a spin coater chuck (a recessed circular aluminum block). The spin coater then begins rotating the chuck with a high acceleration (typically ~ 5000 rpm/s). This acceleration and the high spinning rates (~ 4000 rpm) cause most of the solution to be ejected and a thin film (some 10's of microns) remains. After a short period of time (about 1 s), the remaining solvent in the film evaporates and a polymer film with a typical thickness of 100 nm remains. The thickness can be measured using atomic force microscopy (AFM) or ellipsometry.

In most cases, an annealing step occurred before any further experimentation with the polymer films. Annealing above T_g allows excess solvent that remains after spin coating to be driven off and allows chains to equilibrate from their highly non-equilibrium as-cast states (due to the hydrodynamic shearing during spin coating,

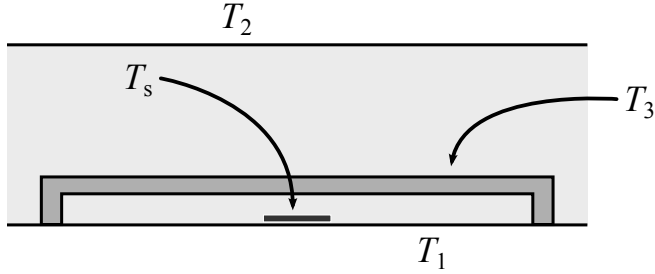


Figure 2.1: (a) Unlevelled data for a typical craze height measurement. For clarity only every tenth data point to be fit is shown. (b) The levelled data with horizontal lines indicating the height of the undisturbed film $h \approx 104$ nm and the height of the craze $h_c \approx 23$ nm, both relative to the substrate at $\tilde{h} = 0$.

and the swelling described around Eq. 1.11, see Paper 1.vi). For annealing, we used a home built vacuum oven that typically operated at 10^{-5} mbar. An example of a vacuum oven that has been used for annealing is schematically shown in Fig. 2.1. The bottom aluminum plate was heated to a temperature T_1 using a heating pad and the temperature measured with a thermocouple, 130°C was a common annealing temperature (see the manuscripts for details). An aluminum plate at the top, separated from the oven walls by a rubber O-ring, was left to be at room temperature, T_2 , and seals the vacuum chamber. A circular aluminum hat, at temperature T_3 measured with a thermocouple, was placed over the sample. The sample temperature, T_s , is determined by an equilibration with the bottom and top plates, and the hat. Since the heating surface is at T_1 , we assume that $T_3 < T_s < T_1$. If the hat is simply placed over the samples, we have found that mechanical contact with the bottom plate is not significant. In this case, the dominant heating mechanism of the hat is through radiation (since the chamber is evacuated) and we find that $T_2 < T_3 < T_1$. The difference between T_1 and T_3 can be between 10 and 20°C . Since the viscosity and relaxation times of polymer chains are exponentially dependent on the temperature [2], we have found that this annealing method is not appropriate when the temperature must be known with a precision of a couple of degrees Celsius. By clamping the hat to the bottom plate, the hat obtains significant mechanical contact. We have found that it is possible to obtain $|T_1 - T_3| < 2^\circ\text{C}$ in this way.

2.2 crazing

As described above, the crazing measurements started by spin coating a thin film of PS on a $30 \times 30 \text{ mm}^2$ mica substrate. The molecular weights used were typically quite large in comparison to all PS described in this thesis (785 and 1140 kg/mol in Papers 1.v and 1.vi), although for the blending experiments, mixtures containing much lower molecular weights were also used (5 kg/mol blended with 785 kg/mol in toluene solutions, Paper 1.v). After spin coating a film, an annealing step was performed (without the clamp in Paper 1.v, with the clamp in Paper 1.vi).

After annealing, the PS films were scored into $9 \times 9 \text{ mm}^2$ sections with a scalpel (nothing more than the weight of the handle and blade is necessary to score the $\sim 100 \text{ nm}$ films). Sections of the PS films were floated onto an ultra clean water bath (Milli-Q or Pall Cascada LS, $18.2 \text{ M}\Omega \text{ cm}$), and picked up across the 1.5 mm gap of fixed, but detachable, aluminum blocks. Prior to floating, these blocks are polished with 4000 grit Si-Carbide sand paper. They were cleaned using acetone and Kimwipes, and were also sonicated in acetone (Fisher Scientific, Optima grade).

After floating, films were left to dry in air for a minimum of 30 min. After drying, the two aluminum blocks were attached to a translation stage and a fixed aluminum platform respectively. The two blocks were unfixed from each other and the translation stage, controlled with LabView software, was moved such that the films had an average strain rate of $\sim 2 \times 10^{-4} \text{ s}^{-1}$. Strain was applied under ambient conditions until crazes were visible under a $4\times$ objective optical microscope. As crazes are typically $\sim 10 \text{ }\mu\text{m}$ wide and up to a few millimetres long, they are best observed using light scattered from their edges at this magnification.

Having produced a film with crazes, the two aluminum blocks are again fixed relative to each other and they are removed from the translation stage and platform. A clean Si wafer is then used as the substrate, onto which the crazed film is placed. Surface (van der Waals) forces pull the film and craze into contact with the Si wafer. The tip of a scalpel blade is then used to put scratches into the film and using AFM, it is possible to measure a height profile as shown in Fig. 2.2.

crazing analysis

With AFM data collected, an example of which is shown in Fig. 2.2(a), the typical measurements that should be acquired are h_c and h , both relative to the substrate. As the changes in the ratio of these values are often quite small, it is important to remove as much as possible all imaging artifacts intrinsic to the AFM scanning. In particular, an analysis developed with this goal in mind has made use of the assumption that for all measurements made on the AFM, there is some background slope on the image, as well as a small (relative to the slope) scan parabola due to non-linearities of the AFM piezo-electric materials. Standard software packages in the analysis of scanning probe microscopy typically have tools to remove both of these artifacts, but usually these can be applied only to a specific region of interest that is not expected to have large, systematic changes in the height. In the craze measurement, we measure a collection of large height changes, in between which we expect the topography to be relatively flat. We have found that the usual analysis methods of common software packages are not adequate for this levelling analysis.

For the typical crazing measurement, the line profile for the height, \tilde{h} , as a function of position, x , has the form shown in Fig. 2.2(a). In our analysis we make the approximation that this data is a composition of three Heaviside step functions, with an additional general quadratic superimposed. Introducing the notation $\Theta_q = \Theta(x - \bar{x}_q)$ for a Heaviside step function centred at \bar{x}_q , the measured profile has the form

$$\tilde{h}(x) = \alpha x^2 + \beta x + \gamma + h\Theta_1 + (h_c - h)\Theta_2 + (h - h_c)\Theta_3, \quad (2.1)$$

$$= \alpha x^2 + \beta x + \gamma + h(\Theta_1 - \Theta_2 + \Theta_3) + h_c(\Theta_2 - \Theta_3), \quad (2.2)$$

$$= \alpha x^2 + \beta x + \gamma + h\Theta_{1\bar{2}\bar{3}} + h_c\Theta_{2\bar{3}}. \quad (2.3)$$

Here, $\Theta_{ij\dots} = \Theta_i + \Theta_j + \dots$ and a tilde (\tilde{i}) indicates subtraction; we should be careful not to confuse γ (the fitting constant) with γ (the surface tension). By selecting the data in regions that we expect to be flat, and neglecting data in regions of height transitions, it is possible to do a linear least squares fit of the data $\tilde{h}_i(x_i)$ after defining

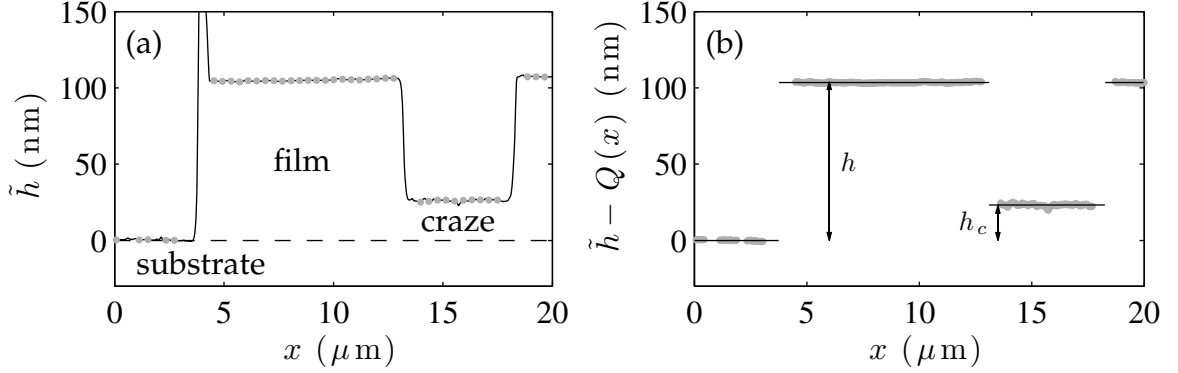


Figure 2.2: (a) Unlevelled data for a typical craze height measurement (785 kg/mol PS, annealed for 40 hr at 130 °C). The line shows every measured data point, with grey points the data to be fit. For clarity only every tenth data point to be fit is shown. (b) The levelled data (grey points) using $Q(x) = \alpha x^2 + \beta x + \gamma$. Horizontal lines indicate the height of the undisturbed film $h \approx 104$ nm and the height of the craze $h_c \approx 23$ nm, both relative to the substrate at $\tilde{h} - Q = 0$.

the three \bar{x}_q . Having done so, we minimize

$$S^2(\mathbf{a}) = \sum_i \left[\tilde{h}(x_i) - \{ \alpha x_i^2 + \beta x_i + \gamma + h\Theta_{1\bar{2}\bar{3}} + h_c\Theta_{2\bar{3}} \} \right]^2, \quad (2.4)$$

where $\mathbf{a} = [\alpha, \beta, \gamma, h, h_c]^T$ and i runs over the data that has been selected for fitting. Setting $\partial S^2 / \partial \mathbf{a}_i = 0$ for all i leads to the following set of linear equations which is inverted for \mathbf{a} :

$$\begin{bmatrix} x_i^4 & x_i^3 & x_i^2 & x_i^2\Theta_{1\bar{2}\bar{3}} & x_i^2\Theta_{2\bar{3}} \\ x_i^3 & x_i^2 & x_i & x_i\Theta_{1\bar{2}\bar{3}} & x_i\Theta_{2\bar{3}} \\ x_i^2 & x_i & 1 & \Theta_{1\bar{2}\bar{3}} & \Theta_{2\bar{3}} \\ x_i^2\Theta_{1\bar{2}\bar{3}} & x_i\Theta_{1\bar{2}\bar{3}} & \Theta_{1\bar{2}\bar{3}} & \Theta_{1\bar{2}\bar{3}} & 0 \\ x_i^2\Theta_{2\bar{3}} & x_i\Theta_{2\bar{3}} & \Theta_{2\bar{3}} & 0 & \Theta_{2\bar{3}} \end{bmatrix} \begin{bmatrix} \alpha \\ \beta \\ \gamma \\ h \\ h_c \end{bmatrix} = \begin{bmatrix} x_i^2\tilde{h}_i \\ x_i\tilde{h}_i \\ \tilde{h}_i \\ \tilde{h}_i\Theta_{1\bar{2}\bar{3}} \\ \tilde{h}_i\Theta_{2\bar{3}} \end{bmatrix}, \quad (2.5)$$

or,

$$\mathcal{M}\mathbf{a} = \mathbf{y}.$$

In \mathcal{M} and \mathbf{y} , it is assumed that all entries are summed over all i . Solving¹ Eq. 2.5 provides a systematic way of measuring h_c and h , as shown in Fig. 2.2(b).

2.3 capillary levelling

The capillary levelling samples also begin with spin coated polymer films, in this case films are cast onto mica and Si substrates, the former being rinsed with ultra pure water, methanol and toluene. In most cases, the films were annealed at 130 °C for 24 hr prior to stepped film preparation (the clamp described at the beginning of this chapter was used in Papers 1.ii and 2.i, 2.ii, but not for Papers 1.i and 2.iii). In these cases, molecular weights between 15.5 and 192 kg/mol are used, though in forthcoming experiments, we will see higher molecular weights used.

After annealing, the preparation of stepped films proceeds as detailed in Paper 1.i; and the process is described here as well. The films on Si form the bottom layer of height h_1 , these heights are typically measured with AFM after all annealing has been completed on the stepped film system. To measure this height, a scratch is put into the film with the tip of a scalpel blade near (typically a few tens to hundreds of micrometres) the spot where capillary levelling profiles were collected. The films on mica were used to form the step of height h_2 .

To form the step, sections of films were floated off mica onto an ultra clean water bath. In cases of low molecular weights ($M_w \lesssim 55$ kg/mol), the films broke apart on the water and this results in many clean edges for the capillary levelling experiments. 55 kg/mol PS films can be tapped gently with tweezers while they are floating on the water and this typically results in their breaking resulting in the presence clean straight edges. For higher molecular weights, the films are much stronger due to the presence of entanglements.

Films with higher molecular weights were picked up using a second 1×1 cm² 1-0-0 Si wafer that has been scored (approximately 1 mm near and perpendicular to the horizontal edge) using a diamond scribe. It helps to expose this second Si wafer to an air plasma (a Harrick plasma cleaner was used here) for approximately 30 s. The plasma cleaning decreases the contact angle of water with the wafer as compared to

¹A MATLAB package written to solve these equations – `craze.zip` – can be found at: http://www.physics.mcmaster.ca/~dalnoki/KDV_Group/Code.html.

an unexposed wafer. The smaller contact angle results in floated films with fewer folds, helping to increase the possibility of finding clean straight edges. With the films on water, the plasma cleaned Si wafers are partially dipped into the water using self-closing tweezers, at a shallow angle typically less than 45° , allowing a meniscus to crawl up the wafer. A section of film is then pushed with clean (cleaning with Kimwipes and acetone is sufficient) tweezers up the meniscus and is held in place with the tweezers until some of the meniscus dries and contact between the film and Si wafer is observed.

The film is then slowly pulled out of the water bath as water evaporates from between the wafer and the film. After completely drying (approximately 10 minutes), the Si wafer with the floated film is split by applying pressure with the diamond scribe on the scored portion of the wafer. The splitting of the wafer results in the film also being split into two pieces. Individually, these two pieces can be floated back onto the water bath. Keeping track of the side that was split by the propagating crack, the PS film spin coated onto Si is dipped into the water at an angle of approximately 90° . The floating film is then gently pushed into contact with the PS-on-Si. Once contact is made, the cohesion between PS and PS ensures that when the PS-on-Si is pulled out of the water, the floating film comes with it. It has been noted that the highest probability of success in making the stepped film as clean and flat as possible occurs if the split edge is the last part of the floating layer to leave the water bath.

After floating of the second layer has been completed, inspection of the sample with high magnification ($50\times$) is necessary. For high molecular weight films, crazes along the split face are commonly found, as are folds in the film. For all stepped films studied here, the regions of interest were free of crazes and folds as viewed with optical microscopy and AFM. The rate of success for making such a stepped film is roughly one-in-six when the molecular weights are high enough for the films to form crazes. For unentangled films, almost all attempts result in a suitable measurement area.

With the preparation of a stepped film completed, AFM was used to inspect the regions of interest before annealing. We have found that the steps are a Heaviside step function to within a couple of hundred nanometres in the x -direction defined by Eq. 1.1. When the topographic slopes are comparable to the AFM tip angle,

interactions between the side of the tip and the topographic features are possible. The topographic features therefore appear broader than they are. Since the AFM tips we use have a tip angle of approximately 45° , it is probable that tip convolution artefacts are present in the as-cast films: the as-prepared steps may be even sharper than they appear as measured with our tips. When steps are free of defects for some tens of micrometres (the typical scan sizes used for the results presented here), annealing of the stepped films was performed at temperatures $120^\circ\text{C} < T < 180^\circ\text{C}$ for tens to thousands of minutes. After annealing, measurements of the same spots inspected prior to annealing were imaged using AFM. In Paper 1.i, optical microscopy was used and images were collected throughout the annealing process. In all cases the widths of the experimentally levelled profiles observed was much greater than the initial width as measured before annealing. Therefore, typical experimental deviations from the Heaviside initial condition used in the models can be neglected.

levelling analysis

The analysis of levelling data starts in much the same way as for crazing data. Our samples are prepared with topography that satisfies Eq. 1.1 to a good approximation (see Papers 1.i and 1.ii for examples of initial height profiles). A typical measured line profile after annealing is shown in Fig. 2.3. The range of distances required is often much larger than for measurements of crazed samples, and the scan parabola from the AFM is often more apparent, as shown. For levelling data, we assume that in regions that have not been disturbed by capillary levelling, the data is still well described by a function with the same form as Eq. 2.3, except with only a single Heaviside step:

$$\tilde{h}(x - \bar{x}_0) = \alpha x^2 + \beta x + \gamma + h_2 \Theta_1, \quad (2.6)$$

where h_2 is the height of the upper layer of the stepped film, \tilde{h} represents the measured data with no levelling, and \bar{x}_0 is determined after removing the quadratic contribution to the data. The function to minimize is

$$S^2(\mathbf{b}) = \sum_i \left[\tilde{h}(x_i) - \{\alpha x_i^2 + \beta x_i + \gamma + h_2 \Theta_1\} \right]^2, \quad (2.7)$$

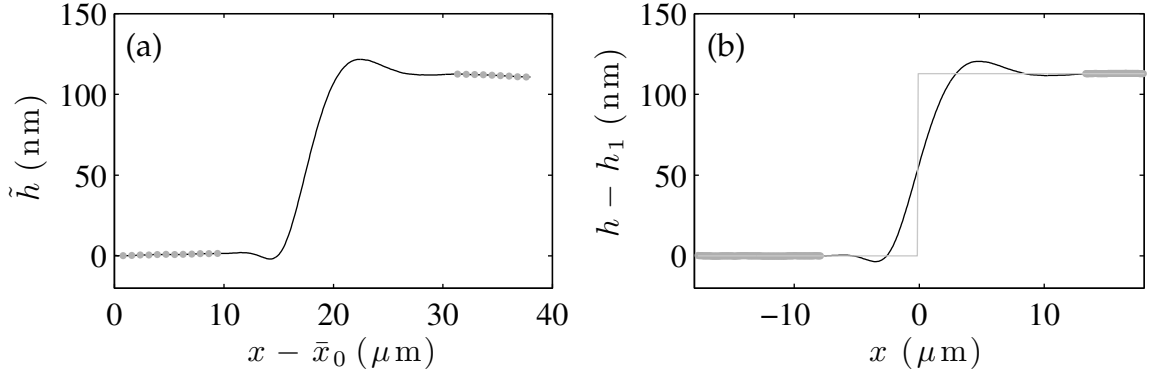


Figure 2.3: (a) Unlevelled AFM data for a typical capillary levelling measurement (118 kg/mol PS annealed at 180 °C for 10 min, $\{h_1, h_2\} = \{87, 113\}$ nm). The line shows every measured data point, with grey points the data to be fit with Eq. 2.7. For clarity only every tenth data point to be fit is shown. (b) The levelled data (black line) with a light grey line indicating the step function with the same volume as the measured height profile. The data which was fit to the step function is shown as grey points.

where $\mathbf{b} = [\alpha, \beta, \gamma, h_2]^T$ and \bar{x}_1 is defined prior to the fitting (note that $\bar{x}_1 \neq \bar{x}_0$ as seen in Fig. 2.3, the latter being determined by the volume conservation described below). Setting $\partial S^2 / \partial \mathbf{b}_i = 0$ for all i as before leads to a system of equations similar to the one shown in Eq. 2.5, determining \mathbf{b} , and in particular h_2 . Since there is a film with height h_1 (measured according to a replacement of h_2 with h_1 in Eq. 2.7 and using the appropriate data set) under the measured baseline for levelling samples, we see that

$$\tilde{h} - Q = h - h_1, \quad (2.8)$$

where

$$Q(x) = \alpha x^2 + \beta x + \gamma. \quad (2.9)$$

In Eq. 2.8, h is the quantity that appears in Eq. 1.35.

With \mathbf{b} determined, it is important to choose the horizontal origin (\bar{x}_0) in a consistent way. This will be crucial when comparing data sets from the same sample at

different times; if the origin is not chosen in a consistent way, then the self-similar scaling (Eq. 1.37) will not collapse the time-dependent data. Since we prepare the samples with a topography that is well represented by $h(x, 0) = \Theta(x)$, a natural way of choosing the origin is to enforce a volume conservation, with the origin being the position of the height step at $t = 0$. This constraint is used to determine the origin. After determining \mathbf{b} and computing $h - h_1$ according to Eq. 2.8, the discrete volume of the measured profile (relative to a height, h_v , which is less than or equal to the minimum height of the profile, $h_v \leq h_{\min}$) is computed according to

$$V_m = \Delta x \sum_{i=1}^n (h_i - h_v) , \quad (2.10)$$

where Δx is the spatial increment of the measured profile and n is the number of measured points². The volume of the step function is

$$\begin{aligned} V_s &= \int dx h_v + h_2 \Theta_0 , \\ &\approx \Delta x \left[\sum_{i=1}^{i_o-1} h_v + \sum_{i=i_o}^n (h_2 + h_v) \right] , \\ &= \Delta x \left[(i_o - 1)h_v + (n - i_o + 1)(h_2 + h_v) \right] . \end{aligned} \quad (2.11)$$

Thus, i_o is chosen so as to minimize $|V_m - V_s|$, which determines \bar{x}_0 . In Fig. 2.3(b) is shown a profile that has been levelled and centred according to the procedure outlined in this section.

determination of the capillary velocity

In the previous section, a method of removing the quadratic contribution from capillary levelling data was described, which yields measured values of h_1 and h_2 and a profile $h(x, t) - h_1$. Using these measurements, we define a dimensionless step profile as $H(X, 0) = H_1 + H_2 \Theta(X)$ with H_1 and H_2 chosen such that their ratio matches the ratio of the measured heights. In Paper 2.i, a method of numerically solving Eq. 1.36 is described. In principle this method can be used to solve for the height

²Using a more sophisticated numerical algorithm for computing the volume produces no meaningful change in the results.

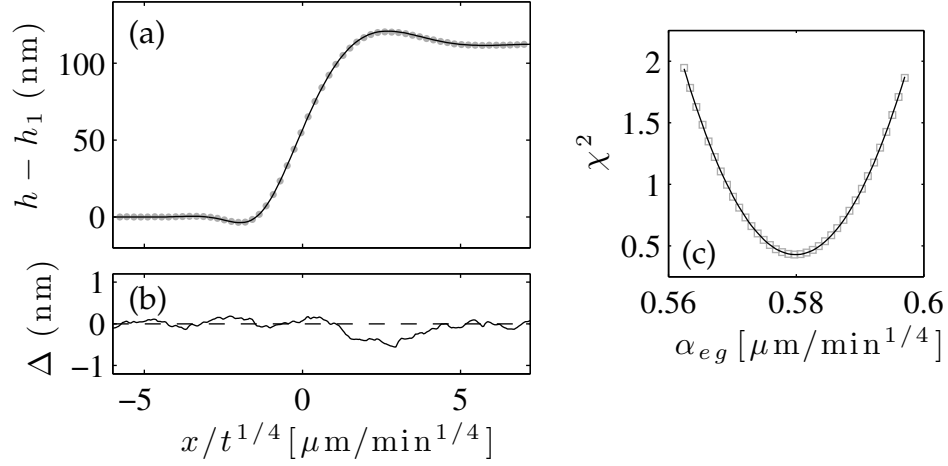


Figure 2.4: (a) Fit of a computed profile ($\{H_1, H_2\} = \{0.77, 1\}$, black line) to the levelled data shown in Fig. 2.3. For clarity, only every fifth measured point is shown. (b) The residuals of the fit with $\Delta = [h - h_1] - h_o[H - H_1]$. Note that a 1 nm deviation is less than 1% of the measured height range. (c) Variation of χ^2 as a function of α_{eg} as defined in Eqs. 2.13 and 2.15. The solid line is a quadratic fit to the computed data (grey squares).

profile starting from any 1-dimensional topography, but there we have focused on the stepped film geometry, along with the spherical cap on a film. In the stepped film case the initial height profile chosen is a discretized version of

$$H(X, 0) = \begin{cases} H_1 & \text{if } X < 0, \\ H_1 + H_2/2 & \text{if } X = 0, \\ H_1 + H_2 & \text{if } X > 0, \end{cases} \quad (2.12)$$

where $H_i = h_i/h_o$. We normally choose $h_o = h_2$. With this initial condition, a special numerical form [75] of Eq. 1.36 is discretely integrated forward in time using a fourth order Runge-Kutta algorithm. The result of such a computation is shown in Fig. 2.4(a).

Using these computational profiles, it is possible to determine a capillary velocity γ/η (where γ is the surface tension). Guided by the self-similarity principle, we define

$f(u) = h(x/t^{1/4})$ and as before $F(U) = H(X/T^{1/4})$. The function to be minimized is

$$S^2(\mathbf{c}) = \sum_{i=1}^n [f(u - \delta_u) - h_2 F(\alpha_{eg} U) + \delta_F]^2, \quad (2.13)$$

where $\mathbf{c} = [\alpha_{eg}, h_2, \delta_u, \delta_F]^T$. The shift δ_u is inserted to remove any error that arises from the discretization in the volume in Eq. 2.10. δ_F is introduced to account for errors in the height measurements. The result for a typical fit, after minimizing Eq. 2.13 with $\partial S^2 / \partial \mathbf{c}_i = 0$ for all i , is shown in Fig. 2.4(a). The residuals of the fit are shown in Fig. 2.4(b), where we see that deviations on the level of 1% are typical. The most physically relevant fitting parameter in Eq. 2.13 is α_{eg} . By comparison to Eq. 1.37, we can see that $\alpha_{eg}^4 = \gamma h_o^3 / 3\eta$. Therefore, we have

$$\frac{\gamma}{\eta} = \frac{3\alpha_{eg}^4}{h_o^3}, \quad (2.14)$$

which is the sought after quantity. Therefore, with a simple stretch of a computed height profile, we find that it is possible to measure the ratio of the surface tension to the viscosity of a polymer film³. For constant molecular weight, we have consistently measured capillary velocities in stepped films with thicknesses (h_1 or h_2) ranging in thickness from ~ 30 to 1000 nm.

To compute the error in the capillary velocity, we use Eq. 2.13 and compute

$$\chi^2 = \frac{S^2(\mathbf{c})}{(n-4) \langle \sigma_h^2 \rangle} \quad (2.15)$$

for a range of α_{eg} in the vicinity of the minimum, α_{\min} . Here we take the average error in the height measurement to be the root-mean-square roughness of the polymer film, $\langle \sigma_h^2 \rangle \approx 0.3$ nm. The variation of χ^2 is shown in Fig. 2.4(c). The error in α_{eg} is taken as inversely proportional to the curvature of the χ^2 versus α_{eg} curve at α_{\min} :

$$\sigma_{\alpha_{eg}} = 2 \left[\frac{\partial^2 \chi^2}{\partial \alpha_{eg}^2} \Big|_{\alpha_{\min}} \right]^{-1/2} \quad (2.16)$$

³A MATLAB package written to level and centre a stepped film profile, and to determine the capillary velocity – `caplev.zip` – can be found at: http://www.physics.mcmaster.ca/~dalnoki/KDV_Group/Code.html.

We thus extract an error in α_{eg} of about 5% of the best fitting value. After carrying the error associated with α_{eg} into the capillary velocity (the error in the height measurement is negligible by comparison), we have $\gamma/\eta = 3.2 \pm 0.6 \mu\text{m/s}$ for 118 kg/mol PS at 180°C. This error is typical for all of the capillary velocity measurements reported in this thesis.

Chapter 3

Summary of Papers

In this chapter and in Appendix B, a brief description of the projects to which I have contributed during the course of my PhD studies is given. In particular, my contributions to each of the projects are explicitly stated. In this chapter, the works for which I was the main contributor are described with the manuscripts to be found in Appendix A, while the works in which I played a secondary role are described in Appendix B.

In Papers 1.i, 1.ii and 2.i, 2.ii, the work concerning the capillary levelling of a stepped film in one dimension is described. Understanding of this system, and in particular the hydrodynamics describing it, helped in our understanding of the system described in Paper 2.iii, where we uncovered new scaling laws in the levelling of liquid droplets on a liquid substrate.

Our work on capillary driven flows continues in Paper 1.iii where we describe the instability of homopolymer rings. In Paper 1.iv, the molecules contained within the rings are diblock copolymers. There we see that the structure of the molecules results in the formation of defected lamellar phases near the boundary of a liquid. The interaction of these defects plays a dominant role in the shape and dynamics of the ring structures. In Paper 2.iv, the structure of the defects driving the experimentally observed flow is considered theoretically.

Papers 1.v and 1.vi are concerned with the structure of the entanglement networks of long-chain polymer films. In Paper 1.v, we investigate the effect of adding small chains of various lengths and weight fractions to these long-chain networks. Paper

1.vi deals with the preparation of non-equilibrium entanglement networks, and also their temporal evolution in the melt state. Paper 2.v deals with the longstanding debate about non-equilibrium effects on the glass transition of thin polymer films.

Paper 1.i

Capillary levelling as a probe of thin film polymer rheology

J.D. McGraw, N.M. Jago and K. Dalnoki-Veress, *Soft Matter*, **7**, 7832 (2011).

This paper is the first in a series that deals with the capillary levelling of stepped polymer films. In essence, it is the proof-of-concept that motivated further study for this system. The quantity that we extract from optical microscopy images is the slope of the topography at the midpoint of the step. We find that the steps become more level as time progresses, in accordance with the intuitive notion that highly curved surfaces should level with time. Using a scaling approach developed by Stillwagon and Larson [76] (Prof. A.-C Shi is gratefully acknowledged for guiding us to this literature), we find that a characteristic width, w , defined by the extracted slope changes with time as $w \sim t^{1/4}$. The prefactor in this power law is inversely related to the viscosity, and by keeping the geometry of the films constant and changing the molecular weight only, we find that the prefactor changes according to the expectations of bulk polymer rheology. That is, we find the expected molecular weight dependence of the viscosity.

I performed the initial experiments on this system, and also developed the method by which samples are prepared in collaboration with my supervisor. Early discussions with Dr. A. Raegen are also gratefully acknowledged here. N. Jago joined our group as a summer student, and I co-supervised him while we worked through methods of extracting quantitative information from the optical microscopy data, and also fine tuned the sample preparation. I wrote early versions of the MATLAB codes used to extract this information. I prepared the first draft of the manuscript.

Paper 1.ii

Self-Similarity and Energy Dissipation in Stepped Polymer Films

J.D. McGraw, T. Salez, O. Bäumchen, E. Raphaël and K. Dalnoki-Veress, Physical Review Letters, **109**, 128303 (2012).

The second experimental study of the stepped film system involved the theoretical expertise of T. Salez supervised by E. Raphaël at the ESPCI in Paris, France. In this study we focused on the details of the topography as the step evolves in time. Using the numerical scheme developed by T. Salez (see Paper 2.i), we found that it is possible to closely match the experimental profiles to the numerically computed ones, as described in Chapter 2 here, leading to a determination of the capillary velocity, γ/η . The temporal evolution is described in terms of a self-similarity argument, and we learn that *all* length scales of the capillary driven stepped film evolve according to $t^{1/4}$ – in particular, this growth law is not limited to w as defined in the Paper 1.i. This generalization of the length scale evolution leads one to the conclusion that the contour length, *i.e.* the energy, also decreases according to $t^{-1/4}$. Aside from the temporal evolution of the stepped bilayer, we also investigate the geometric dependence of the evolution. By varying h_1 and h_2 in the as-prepared stepped films while keeping the molecular weight constant, we see that the fraction of the initial free energy is different at a constant annealing time for different film geometries. We determined that for the range of thicknesses, molecular weights and times investigated in this study, it is possible to collapse nearly all of the data onto a master curve that was justified by invoking self-similarity principles (Papers 2.i and 2.ii describe details not contained in this Paper).

For this study, I designed and performed the experiments and wrote the first manuscript; T. Salez wrote the theoretical section of this paper. The completion of the manuscript was a collaboration between all the authors. I was also heavily involved with discussions of the theoretical work that was led by T. Salez.

Paper 1.iii

Plateau-Rayleigh instability in a torus: formation and breakup of a polymer ring

J.D. McGraw, J. Li, D.L. Tran, A.-C. Shi and K. Dalnoki-Veress, *Soft Matter*, **6**, 1258 (2010).

In the last surface tension driven flow experiment, we investigated the instability of toroidal caps on a Si substrate. The rings are forced to undergo a glassy-to-liquid transition by immersion in a toluene saturated atmosphere (our experience here inspired the method for preparing the droplets in Paper 2.iii), and break up via a Plateau-Rayleigh instability. Because of their toroidal nature, an alternative energy minimization route exists, in which the rings can simply shrink into a single droplet. We find that the evolution of toroidal rings is a competition of both mechanisms. In addition to observing ring breakup and shrinking in the liquid state, we performed simulations of a time dependent phase separation process; these were done by J. Li under the supervision of A.-C. Shi. Using these simulations, and being guided by the literature on the formation of ring shaped coffee stains [77], we propose a mechanism for the ring formation during the complex spin coating process that is used to prepare them.

This paper is a good demonstration of the principle that we should follow up on the sometimes fun and unexpected results that are inevitable in research. The formation of rings on a substrate was discovered by D. Tran during an honour's research project which I co-supervised. The original goal of the project was to prepare 'unentangled films' – the droplet-into-methanol method was just one of many attempts to prepare such films. Following their discovery, D. Tran focused his attention on ring break up using optical microscopy. I collected all the AFM data that appears in the manuscript, helped develop the model used to describe their formation with J. Li, and wrote the first draft of the manuscript.

Paper 1.iv

Dynamics of interacting edge defects in copolymer lamellae

J.D. McGraw, I.D.W. Rowe, M.W. Matsen, and K. Dalnoki-Veress, *European Physical Journal E*, **34**, 131 (2011).

Following our investigations of homopolymer rings, we prepared rings out of diblock copolymers. In this study, the toroidal nature of the rings is neglected, as the curvatures in the plane of the substrate are much smaller than the curvatures in the substrate-normal direction. Thus it is the radial height profile that we are concerned with, furthermore, we focus our attention on the outer-most portions of the rings. In this region, the height profile imposed by the formation of the rings is asymmetric with respect to the highest point on the ring. Lamellae form parallel to the substrate, and at the edges of the ring, they form steps. Each of these steps is a defect in the lamellar structure that has an associated energy cost. When these defects are too close to one another, there is an edge-edge interaction which causes the defects to move relative to one another. We find that the edge motion is well described by a model assuming a quadratic inter-edge potential with the motion being described by classical mechanics.

For this project, I completed the initial experiments demonstrating that rings could be prepared from diblock copolymers, and that their evolution and structure was different from the homopolymer rings. I. Rowe joined the group as an honour's thesis student, whom I co-supervised on this project. I. Rowe completed many of the early experiments which led to our studying the edge interaction and also collected the first edge collection evolutions. I collected several more edge evolutions; developed the model; wrote data analysis codes and numerical routines for solving the differential equations using MATLAB; and wrote the first draft of the manuscript.

Paper 1.v

Swelling molecular entanglement networks in polymer glasses

J.D. McGraw and K. Dalnoki-Veress, Physical Review E, **82**, 021802 (2010).

In this project we turn our attention to the entanglement networks of films composed of binary and ternary molecular weight blends of PS. The majority component of the blend is a long chain which has on average ~ 50 entanglement strands. We mix short chains with these long ones, the molecular weights of the shorter chains being less than or in the vicinity of the entanglement molecular weight, M_e . We find that the short chains act to dilute the entanglement network of the long chain system, and that the molecular weight and composition dependence is captured by a simple packing model.

This project began during the time of my MSc studies, and was written about exclusively in my MSc thesis. The data for binary blends was collected during this time. All of the ternary blend data was collected during the beginning of my PhD studies. The model used to describe the data changed considerably over the first year of my PhD studies and the manuscript, written by me, followed these changes accordingly.

Paper 1.vi

Relaxation of non-equilibrium entanglement networks in thin polymer films

J.D. McGraw, P.D. Fowler, M.L. Ferrari and K. Dalnoki-Veress, submitted to European Physical Journal E on 11/10/12, e120229: 8 pages.

In this paper, we continue the use of crazing measurements to investigate the entanglement networks of thin polymer films. Here we are concerned with non-equilibrium states of the entanglement networks, and how they evolve in time. Two systems are studied: the first is a network that results from the violent spin coating process that is used extensively in science and technology for the preparation of thin polymer films. We conclude that these networks must contain highly stretched chains upon formation. We observe the temporal evolution of the craze measurement, $(h_c/h)^2$, and find that this plateaus on a time scale that is consistent with the bulk polymer reptation time. We note that this temporal result is in contradiction with several reported results in the literature, and we offer plausible explanations for why this might be. These are questions that will need to be addressed by the community in the future.

The second entanglement network studied in this paper is the non-equilibrium system formed in the preparation of a bilayer polymer film. These bilayers, equilibrated according to the measurements provided in the first system studied, contain an *entropic* interface at their centres, through which the polymer chains have been folded back onto themselves. These reflected chains are not at equilibrium since their conformations have been restricted by what used to be an air-polymer interface. In the melt, these entropic interfaces heal as revealed by the crazing measurement. Remarkably, the time scale of the interface healing is shorter than a bulk reptation time. We propose a simple model that accounts for this fast relaxation.

All of the measurements reported in this paper were performed by P. Fowler. An early version of the bilayer evolution plot was completed by M. Ferrari, it was these measurements which led us to the conclusion that the sample annealing temperature could be controlled to a much finer degree by clamping the hat in our vacuum ovens. I co-supervised M. Ferrari during an honour's thesis project, and also co-supervised P. Fowler during summer research and honour's thesis projects. I completed early

experiments in the bilayer evolution project, demonstrating their feasibility. I also wrote the first draft and developed the models describing the data.

Chapter 4

Outlook and Conclusions

Just below Eq. 1.1, it was stated that Papers 1.i, 1.ii and 2.i, 2.ii lay the groundwork for a versatile tool that can be used to attack many problems in the physics of polymers near surfaces and interfaces. Here, examples of problems that we have begun addressing will be presented, along with a preview of some data. As with Papers 1.i, 1.ii and 2.i, 2.ii, the work shown here has been done in collaboration with T. Salez and E. Raphaël (theory), and with O. Bäümchen (experiments), along with my supervisor.

Eq. 1.35 is known to us as the Thin Film Equation (TFE). As the projects that we undertake have necessitated the use of new physics in the hopes of understanding experimental results, the number of acronyms employed has grown. Here, we will very briefly describe the ‘Slip’, ‘Ultra’ and ‘Asymmetric’ Thin Film Equations (STFE, UTFE and ATFE). The goal in these sections is to give a flavour of the physics we explore in upcoming projects.

In addition to the projects described in detail below, we here speculate on some of the outstanding problems to which the stepped film geometry may have some relevance. The glass transition temperature of thin polystyrene films was reported by Keddie, Jones and Cory [60] to be reduced when the films were less than a critical thickness. This observation is consistent with the idea that molecules at surfaces and interfaces are different than those in the bulk. Thus, if the system size is comparable to some interfacial length scale, then one might expect deviations from bulk behaviour, in particular where this is related to glassy dynamics. Since the work of Keddie,

Jones and Cory was published, there have been a large number of studies reporting deviations from bulk behaviour (see selected works by Forrest [78], Torkelson [79], Ediger [80], McKenna [45] and others). The stepped film system can be used to shed light on this problem of glassy dynamics since the presence of the height step provides a driving force which may lead to a surface evolution, even below the glass transition temperature [81].

There is still much to be learned about the entropic interface described in Paper 1.vi, and stepped films could be used to gain insights into this problem. Just as an entropic interface exists between the bilayer films prepared in that paper, all of our stepped films have a similar interface when the molecular weight is significantly above the entanglement molecular weight (for all the stepped film levelling experiments presented here, the timescales probed are too long to see any effect of the transient entropic interface). Preparing films with molecular weights both significantly above and below M_e would be necessary. If one prepared such stepped films and performed experiments for times much shorter than the times required to reach self similarity, differences in the evolution could be attributed to the healing of the entropic interface created by floating two films atop one another. These types of experiments could lead to insights about the nature of entanglements in polymer systems.

Related to the early time regime described in the previous paragraph, the stepped film experiments could lead to insights about the transient regime of differential equations such as Eq. 1.35. Using stepped films with molecular weights that are below M_e , and annealing for times shorter than the time required to reach self-similarity, one could gain experimental access to these early times. The study of equations such as Eq. 1.35 is an active research topic (see *e.g.* [82]), and the stepped film levelling system could provide a valuable source of insight.

Slip TFE

In deriving Eq. 1.34, it was assumed that the velocity of the fluid at the solid-liquid interface is $u(0) = 0$. However, this is not necessarily the case as has been demonstrated by many researchers (see *e.g.* [47, 50, 83]). In the case where liquids slide against a solid substrate, we define the slip length, b_s through the boundary condition $u(0) = b_s \partial_z u|_0$ (see Fig. 1.6). Defined as such, the slip length is the distance below the substrate

that the fluid velocity linearly extrapolates to zero. Using a boundary condition that incorporates a non-zero slip length gives rise to the Slip Thin Film Equation (STFE):

$$\partial_t h + \frac{\gamma}{3\eta} \partial_x [(h^3 + 3b_s h^2) \partial_x^3 h] . \quad (4.1)$$

This equation is identical to Eq. 1.35 except for the presence of a second term added to the h^3 term in the spatial derivative portion of the continuity equation. In particular, it is possible to non-dimensionalize the equation in exactly the same way as for the TFE, and we have the same self-similarity variable, $U = \left(\frac{3\eta}{\gamma h_o^3}\right)^{1/4} \frac{x}{t^{1/4}}$, as defined in Eq. 1.37.

Teflon surfaces are known to show slip behaviour [50], and in Fig. 4.1(a), we show a comparison of profiles that demonstrate conclusively two ideas. First, the substrate, and in particular the slip length, plays a role in the observed profile. A slippery substrate allows for the movement of more material. Second, on the same slippery substrate, there is a molecular weight dependence on the slip. This is seen to be true by the observation that the higher molecular weight levelling experiment has a broader profile in the reduced position variable (*i.e.* the dependence of the viscosity has been normalized so we only see effects due to the substrate- M_w combination in this representation).

Ultra TFE

As described in [34] and in Paper 1.vi, the entanglement network near an uncrossable boundary is highly modified. In [41] and [42] it was suggested that the mobility of polymers near such uncrossable interfaces is enhanced, and this is probably due in part to the modified entanglement networks that exist there. These results have motivated us to study a similar system, one in which the bottom layer of our stepped film is comparable to the size of the unperturbed polymer size.

In Fig. 4.1(b) is shown the measured height as a function of position for a stepped film with $\{h_1, h_2\} = \{18, 96\}$ nm using 192 kg/mol PS. For this molecular weight, the radius of gyration is $R_g \approx 12$ nm. There is also a fit shown that used a profile computed using Eq. 1.36. The salient feature of this fit is that it does not capture the data in the dip region. We propose that this failure of the fit is due to the fact

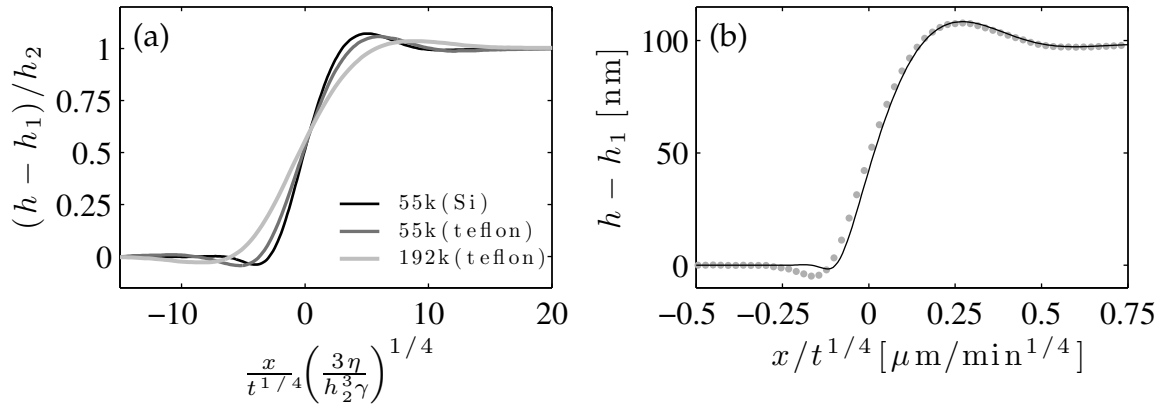


Figure 4.1: (a) Height as a function of scaled position for capillary levelling of stepped films on Si and on teflon. The horizontal axis is chosen such that the heights, times and viscosities of the polymers are normalized. The differences in the profiles are due to the slip boundary condition at the solid-liquid interface. Data on teflon collected by O. Bäümchen. (b) Height *vs.* scaled position for 192 kg/mol PS with $\{h_1, h_2\} = \{18, 96\}$ nm annealed at 140 °C for 2030 min. The points are measured data while the black line is a fit to Eq. 1.35 (TFE).

that the polymer chains on the thin side of the stepped film are confined, and as a result are more mobile. If the chains are more mobile on the thin side, then more molecules would move from this side to reduce the free energy associated with the step in the height. This kind of enhanced mobility can be modelled with a height dependent viscosity. We thus have the Ultra-Thin Film Equation (UTFE):

$$\partial_t h + \frac{\gamma}{3} \partial_x \left[\frac{h^3}{\eta(h[x])} \partial_x^3 h \right], \quad (4.2)$$

where $\eta(h[x])$ is a phenomenological effective viscosity, see [42] for an example of this kind of approach to the modelling.

Asymmetric TFE

In order to test the idea that a higher mobility layer on the thin side of the stepped film would result in a relatively larger dip, we prepared samples that were composed of PS with two different chain lengths. In order to directly compare to the results of the previous section, we prepared a thin PS film on Si with molecular weight 55.5

kg/mol. To complete the stepped film, we floated a 192 kg/mol PS film – with roughly the same height as that on the Si wafer – as the capping layer. Thus, we *know* in this case that the material on the thin side of the stepped film is much more mobile. In Fig. 4.2(a) we show the results of such an experiment. The stepped film was annealed for 240 min at 140 °C.

For comparison, we show a stepped film in Fig. 4.2(b) that was composed of a *blend* of the two molecular weights and also had $h_1 \approx h_2$. This profile is well described by a profile computed according to Eq. 1.36 (Paper 2.i) and fit according to the procedure outlined in Section 2.3. Comparing the profiles in Figs. 4.2(a) and (b), one can see that the profile in (a) has moved much more material from the thin side of the bilayer as compared to the case in (b) where the molecular weight distribution (mobility) is uniform.

Finally, if the material on the thin side of the stepped film is *less* mobile than the material on the thick side, then we would expect that the dip would be small in comparison to the symmetrically distributed mobility case. In Fig. 4.2(c) is shown the results for an experiment in which we used a higher molecular weight for the film on the Si substrate; the step is approximately the same height as the film that was prepared on Si. It can be seen that the dip is much smaller than would be expected if the film had a symmetrically distributed mobility.

In order to understand the data presented in Fig. 4.2, we have developed a model, the Asymmetric Thin Film Equation (ATFE), that has nearly the same form as the one shown in Eq. 4.2. In this case, the physics is slightly different and we instead have $\eta(h[x]) \rightarrow \eta(M_w[x])$ where the position dependent, weight averaged molecular weight (Eq. 1.3) determines the local viscosity [25]:

$$\partial_t h + \frac{\gamma}{3} \partial_x \left[\frac{h^3}{\eta(M_w[x])} \partial_x^3 h \right]. \quad (4.3)$$

This equation relies on the presence of a Poiseuille flow (quadratic velocity profile $u(z)$) to be valid, which in turn requires the molecular weight distribution in the vertical direction to be uniform, while the film has a non-uniform distribution of molecular weights in the horizontal direction. Since the lateral distances involved in our problems are much larger than the vertical ones, we will assume that a fast mixing in the vertical direction, compared to flow times in the x -direction, is valid.

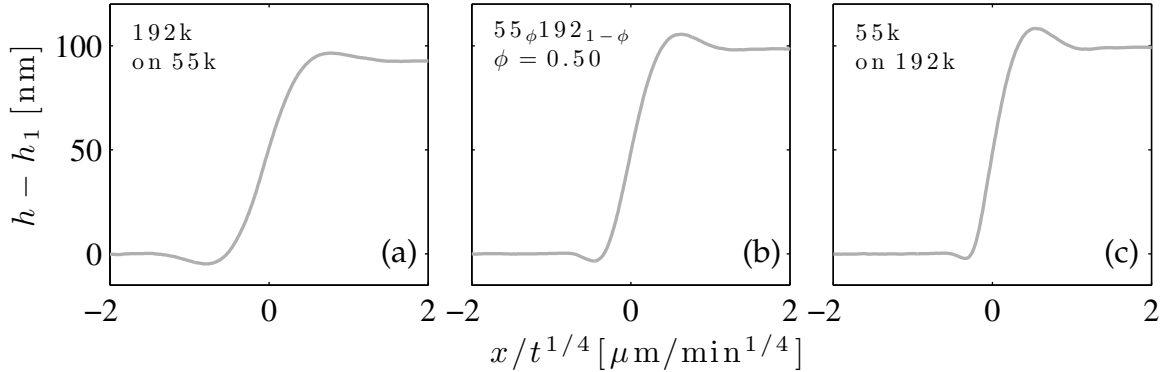


Figure 4.2: Demonstration that laterally asymmetric molecular weight distribution in the stepped films results in profiles with different shapes. For all films here, $h_1 \approx h_2$, such that the film geometry cannot account for the profile shapes. (a) The film making up the bottom layer has a high molecular weight; (b) the two films composing the sample are made from the same blend; and (c) the lower molecular weight makes up the lower film.

Conclusion

Surface tension is the result of a non-trivial, spatially varying interaction potential between molecules: creating a surface requires energy. As a result of this energy cost, nature tries to minimize the surface area of a given interface. In the works presented here, we have taken advantage of this fact to study the physics underlying a wide range of liquid polymer systems. First, we have studied the evolution of a liquid system that is prepared with a surface that is well described by a Heaviside step function. In this case, the excess surface area is provided by the height jump, and this excess is found to dissipate with a power law in time $\Delta L \sim t^{-1/4}$. In Papers 1.i, 1.ii and 2.i, 2.ii, we describe how this dissipation law comes about, and also derive the geometric and material dependences that are in the prefactor of this simple energy dissipation relationship. As a result of these studies and the various projects described in the Outlook, it is hoped that the stepped film geometry will be useful in the study of thin film polymer physics and thin-film hydrodynamics.

In Paper 1.iii we have observed that surface tension is responsible for the breakup of polymer tori prepared on a substrate. We have also prepared these toroidal sections from diblock copolymers as described in Paper 1.iv. We observe that the interplay

between surface tension and the preferred lamellar structure results in a repulsion between lamellar defects found at the interface of a thin film of symmetric diblock copolymers.

When polymers are confined to thin films, it often happens that the method by which these films are prepared leaves the chains in highly non-equilibrium configurations. As the distribution of entanglements, and the chain length statistics play such an important role in the physics of polymers, it is important to understand how preparing films affects these quantities. In Papers 1.v, 1.vi and 2.v, we investigate these effects. We have found that small chains tend to dilute entanglements. Intermediate length chains do so as well, and there is a non-trivial molecular weight dependence for the dilution probability in a crazing experiment. We have found that spin coating, the method most commonly used for the preparation of thin polymer films, leads to highly stretched, non-equilibrium chain configurations. Annealing above T_g for periods of order one reptation time is enough to lose memory of the spin coating effect for our samples prepared on mica. Polymer chains near interfaces take on different conformations than those in the bulk. In Paper 1.vi, we investigate the effect of placing two equilibrated polymer interfaces into contact. In the liquid state, the chains explore new configurations, and the reflection that cost the chains in entropy is undone on a time scale that is shorter than the bulk reptation time.

Appendix A

Appended Papers

Manuscript i

Capillary levelling as a probe of thin film polymer rheology

J.D. McGraw, N.M. Jago and K. Dalnoki-Veress, *Soft Matter*, **7**, 7832 (2011).

Cite this: *Soft Matter*, 2011, **7**, 7832

www.rsc.org/softmatter

PAPER

Capillary levelling as a probe of thin film polymer rheology

Joshua D. McGraw, Nicholas M. Jago and Kari Dalnoki-Veress*

Received 15th February 2011, Accepted 8th April 2011

DOI: 10.1039/c1sm05261f

While measuring the rheology of bulk polymer systems is routine, when the size of a system becomes comparable to molecular dimensions, properties of flow are hard to measure and poorly understood. We present the results of experiments that are easily performed and can probe the rheological properties of polymer films that are mere tens of nanometres in thickness. Glassy bilayer polymer films are prepared with height profiles well approximated by a step function. Upon annealing such stepped bilayer films above the glass transition, the height profiles broaden due to gradients in the Laplace pressure. By varying the molecular weights of the stepped films, we control the rate at which the broadening takes place. A scaling relation derived in the lubrication approximation is used to show that the rate of broadening is consistent with that expected from polymer rheology in the bulk, thus validating the technique as a uniquely versatile rheological probe for thin polymer films.

Introduction

Molecular mobility in confined environments is markedly different from that in the bulk. The study of confined flows has received considerable attention as the application of thin liquid films becomes relevant to industrial processes. Specifically, when a polymer melt is confined to length scales smaller than the natural size of these long chain molecules in the bulk, material properties change. These changes pose great challenges for our fundamental understanding of these systems. For this reason developing robust experimental methods for the study of flow in confined environments is an important endeavour; here we wish to make a contribution to this end.

Two notable experimental methods by which one can study the viscous and viscoelastic response of polymers confined to nanoscale dimensions are by the observation of dewetting liquid films from a substrate^{1–9} and the evolution of small scale surface structure.^{10–17} In the case of the former, much has been accomplished in understanding the fundamental processes that govern the dynamics of hole nucleation and growth. Dewetting in thin films proceeds because there can be a reduction of the free energy by exposing the underlying substrate. The energy gained by exposing the substrate is dissipated by viscous friction in a rim that forms around the dewetting hole. Fruitful collaboration between theory^{1,4,18–20} and this experimental technique has led to alternative measurements of the polymer reptation time,⁵ an improved understanding of the mechanisms controlling slip effects at the substrate polymer interface,^{7,8} and insight into the effect of film preparation on the rheology of thin polymer films.⁹

In addition to dewetting, hole growth in free standing polymer films has also been shown to be a valuable method of probing viscoelasticity of thin polymer films.^{21–23}

In the case of liquids which do not dewet a substrate and have some surface topography, there is an energy reduction due to a free surface evolution. Excess surface area is reduced by the Laplace pressure and the relaxation of the surface is moderated by viscous losses.^{10,24–26} The Laplace pressure arises from local curvature at the free surface, ρ , and is equal to $p = \gamma/\rho$, where γ is the surface tension.²⁴ In cases where lateral length scales are much greater than vertical ones, which is the case we will consider here, the inverse of the radius of curvature is simply given by the second derivative of the height with respect to position, $1/\rho \approx \partial_x^2 h$. Various experimental systems have been developed to study the relaxation of local curvature to investigate viscous, elastic and glass transition effects.^{11–17}

The measurement we describe here is among the list of rheological experiments that take advantage of surface tension to measure viscous properties of thin polymer films. In what is to follow, we will describe the technique which relies on preparing *stepped bilayer films* for the study of thin film rheology. The resulting samples are prepared in the glassy state and transition from a ‘thin’ to ‘thick’ region with an initial height profile that is well described by a Heaviside step function. As shown schematically in Fig. 1(a), the stepped films are composed of a film with thickness h_1 at the substrate, partially capped with a second film of thickness h_2 . A jump in temperature to above the glass transition, T_g , allows the system to relax. The relaxation proceeds such that the excess surface area in the transition from a thin film with thickness h_1 to a thick film with thickness $h_1 + h_2$ gradually disappears under the influence of surface tension. As shown in Fig. 1(b), we characterize the evolution of the surface profile with the width, w , which is a dominant length scale

Department of Physics & Astronomy and the Brockhouse Institute for Materials Research, McMaster University, Hamilton, ON, Canada.
E-mail: dalnoki@mcmaster.ca

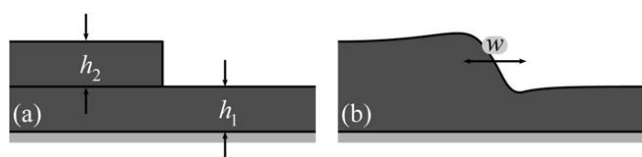


Fig. 1 Schematic diagrams of the sample geometry. (a) The as-prepared glassy stepped films composed of two layers: one in contact with the substrate of height h_1 and a second partially covering the first with height h_2 . (b) When the temperature is above T_g , the films are in the melt state and the width, w , spanning the regions between 'thin' (h_1) and 'thick' ($h_1 + h_2$) broadens.

describing the flow. Since the force of surface tension driving flow is balanced by viscous stresses, varying the molecular weight of the polymer used in the bilayers modifies the viscous damping. While our approach is complementary to the techniques described above, it is distinct in its ease and versatility. Here we consider the simplest case of two layers composed of a single polymer species with the same molecular weight. However, it is a simple matter to extend this technique to heterogeneous stepped films: two films of differing molecular weight, differing chain architecture (e.g. linear and branched), or chemically distinct polymer species, to name a few.

Experiment

All samples discussed in this work were prepared such that both films making up the stepped bilayer were prepared from polystyrene (PS) of the same molecular weight. The PS used had weight averaged molecular weights, $M = 24.7, 55.5$ and 118 kg mol^{-1} , with polydispersity indices of 1.03, 1.07 and 1.05 (Polymer Source Inc.). The polymer was dissolved in toluene with concentrations ranging from 1.0 to 3.9 wt% depending on the molecular weight of the polymer and the desired film thickness. In the first stage of the stepped bilayer preparation (see Fig. 2) a film with thickness approximately $h_1 = 100 \text{ nm}$ was spincast onto a $10 \times 10 \text{ mm}^2$ Si wafer (University Wafer). A second film also with an approximate thickness of $h_2 = 100 \text{ nm}$ was spincast onto a freshly cleaved $25 \times 25 \text{ mm}^2$ mica substrate (Ted Pella Inc.). Both films were annealed at $120 \text{ }^\circ\text{C}$ in vacuum for approximately 12 h to remove residual stress and solvent. After

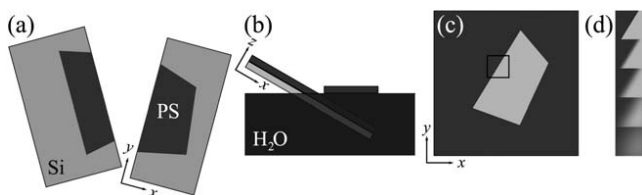


Fig. 2 Schematic diagrams illustrating steps of the sample preparation. (a) A PS film is floated from mica onto a bare Si wafer, which is then split in half. (b) One piece of PS, from (a) is floated off of the Si and onto a water bath. (c) This portion of the PS film is then picked up using a thin film of PS that has been spincast onto a Si wafer. (d) The resulting stepped bilayer film, composed entirely of PS on a Si substrate, shows different light intensity under optical microscopy due to the differences in optical path length of the monolayer and bilayer region. (d) Schematic sequence showing that the transition in film thickness of the boxed film portion shown in (c) broadens upon annealing above T_g .

the initial annealing step, portions approximately $8 \times 8 \text{ mm}^2$ of the film which was spincast onto mica were floated onto a clean water bath (Milli Q). These pieces were then picked up using another $10 \times 10 \text{ mm}^2$ Si wafer. A section near the edge of the Si was previously scratched using a diamond scribe along the crystal axis prior to floating. Immediately after picking up these portions of the film, the diamond scribe was used to press firmly on the scratch near the edge of the Si wafer. The pressure induces fracture of the Si wafer along a line of crystal symmetry. With the film floated across this line, the procedure results in a polymer film with a straight edge (see Fig. 2(a)). Having prepared a thin film with a straight fracture, these portions of the film are again floated onto the clean water bath and subsequently picked up using the Si wafers which have had thin PS films previously spincast and annealed (Fig. 2(b)). With this procedure, it is possible to find portions of the bilayer polymer film with height profiles that are well approximated by a Heaviside step function, $h(x) = h_1 + h_2$ if $x < 0$, and $h(x) = h_1$ otherwise, where $h(x)$ is the film height at position x ; this stage of the preparation is shown in Fig. 1(a) and 2(c). The portions with straight edges are easily found using an optical microscope.

Prior to measurements on the surface profile evolution (see schematic in Fig. 2(d)) the step heights were measured using an atomic force microscope (AFM, Veeco Caliber) in tapping mode as follows. A scalpel blade was used to make a scratch down to the hard Si substrate, away from the region where the surface profile is to be observed. An AFM image in the region where the substrate is exposed could then be used to determine the thickness h_1 ; h_2 was subsequently determined by AFM in the region where the sample was to be observed using optical microscopy.

The prepared bilayers were placed on a heating stage (Linkam) in air and the temperature was rapidly increased ($90 \text{ }^\circ\text{C min}^{-1}$) from room temperature to $180 \text{ }^\circ\text{C}$, which is well above the glass transition of PS, $T_g \sim 100 \text{ }^\circ\text{C}$ (we have verified that performing the experiment in an inert argon atmosphere using a 52 kg mol^{-1} sample produces identical results to similar samples annealed in air). Shortly after reaching the final annealing temperature, optical microscopy images were collected at various intervals up to annealing times of approximately $6.6 \times 10^4 \text{ s}$. An optical filter centred at 630 nm (Newport 20BPF10-630, FWHM $\sim 10 \text{ nm}$) was placed between the light source and the sample so that, to a good approximation, all light reaching the CCD was monochromatic.

Under monochromatic illumination the light intensity observed in the optical images is a direct consequence of thin film interference.²⁷ In order to calibrate the thickness obtained from the light intensity values measured using the CCD camera, we prepared a series of thin PS films on $10 \times 10 \text{ mm}^2$ Si wafers. The thickness of all films was measured using ellipsometry. These eighteen films prepared ranged from 13 nm to 200 nm in thickness, bridging the range of thicknesses relevant to this study. Prior to each measurement of the surface profile evolution, a set of images was taken at the same exposure time and light intensity using the calibration samples so that, using an appropriate phase contrast model,²⁷ the intensity could be related to the thickness of the samples (see appendix).

For speed, versatility, and ease, measurements were performed with optical microscopy. However, the optical measurements

were verified using AFM. A sample with a molecular weight of 118 kg mol^{-1} was used to prepare a step edge as described above. The initial height profile was measured in tapping mode, and the sample was then heated to $180 \text{ }^\circ\text{C}$ for ten minutes. Following a quench to room temperature, the topographic data in the area of interest was again measured in tapping mode. This procedure was repeated several times for various annealing times up to an annealing time of approximately $4 \times 10^4 \text{ s}$.

Results and discussion

Atomic force microscopy

In Fig. 3, we show AFM topographic data for lines perpendicular to the step edge of a bilayer film. At $t = 0.04 \text{ s}$, our claim that the as-prepared bilayer film height profile is well represented by a Heaviside step function is verified. As time progresses, the transition region from thin to thick broadens. In addition, a prominent dip forms which falls below the thin portion of the stepped film. The dip is the result of material flow towards the low pressure region, thus depleting material from the thin portions. To characterize the width of the transition region, we obtain the tangent to the topographic data at position x_0 , where the height is half way between the thick and thin region $h_0 = h_1 + \frac{1}{2}h_2$. The width of the transition region can then be defined through the slope of the tangent line, $\partial_x h|_{x_0}$, as

$$w \equiv h_2(\partial_x h|_{x_0})^{-1}. \quad (1)$$

Defined in this way, w is the distance over which the extrapolated tangent of the $h(x)$ data at (x_0, h_0) traverses a height h_2 . The inset of Fig. 3 shows the temporal evolution of widths as measured by AFM. We note that the first data point corresponding to the as-prepared bilayer film is shown at $t = 0.04 \text{ s}$. This value for the time requires some justification.

As will be discussed below, the data is expected to follow a power law, $w(t) = bt^n$ with t the annealing time, and

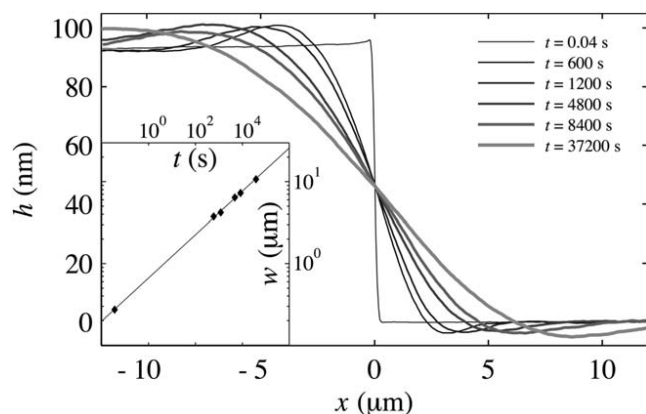


Fig. 3 AFM height profiles, horizontally shifted such that $h(x) = h_0$ when $x = 0$, of a 118 kg mol^{-1} PS stepped bilayer film annealed for various times up to $\sim 4 \times 10^4 \text{ s}$. The substrate is approximately 90 nm below the line extending horizontally from $x = 0$ through $x = 10 \text{ } \mu\text{m}$ in the AFM trace at $t = 0.04 \text{ s}$. The inset shows the width (see eqn (1)) of the transition from thin to thick film regions as a function of time. The line is a power law fit as described in the text.

b a constant. However, the annealing time of the as-prepared film should not be taken as $t = 0$, because there is ambiguity in the initial state for two reasons: (1) the as-prepared stepped film will evolve even at room temperature due to the high initial Laplace pressure; and (2) while the as-prepared film may be well approximated as a Heaviside step function, it will deviate from that on the smallest length scales. Thus, we fit the power law with an offset, which is equivalent to suggesting that the film, which relaxed at room temperature, had evolved as if it was heated at $180 \text{ }^\circ\text{C}$ for 0.04 s . Clearly the functional form with $b = 0.7 \pm 0.2$ and $n = 0.26 \pm 0.02$ is an excellent fit to the data.

Optical microscopy

In Fig. 4 we show typical optical images of the same spot on a 24.7 kg mol^{-1} stepped film, both as-prepared (a), and after annealing for approximately $6.6 \times 10^4 \text{ s}$ (b). These images can be compared to the schematic evolution shown in Fig. 2(d) and the evolution of the AFM line profiles in Fig. 3. The contrast in the images is due to spatial variation of the optical path length resulting from differences in the film thickness. The solid white lines in Fig. 4(a) and (b) show the observed average intensity across the transition region. Consistent with the schematic and the AFM data, these images show that the transition between the thin and thick regions of the film broadens with time. In comparing AFM to optical microscopy data, it is worthwhile noting that while AFM has the advantage of being able to probe narrow transition widths, optical

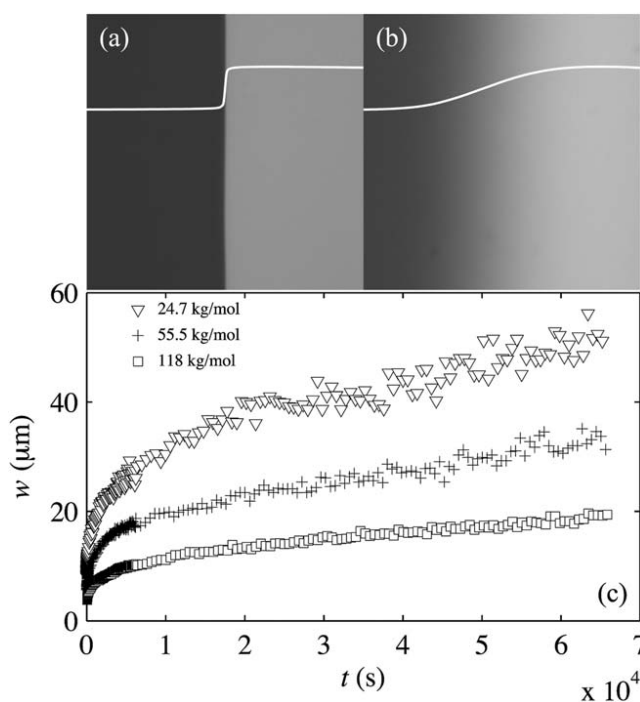


Fig. 4 (a) An optical image of an as-prepared 24.7 kg mol^{-1} PS stepped film; and (b), the same sample after annealing for approximately $6.6 \times 10^4 \text{ s}$. Optical microscopy images were obtained under monochromatic illumination. The solid white lines show the averaged intensity profile across the transition region. The width and height of both images is $65 \text{ } \mu\text{m}$. (c) The width, $w(t)$, for the transition region of the stepped films prepared from three different molecular weights. w was determined from the optical images and determined using eqn (6).

microscopy can access small gradients in the height. Remarkably this translates to being able to probe lateral flows over tens of micrometres in films with thickness ~ 100 nm. The geometry of this stepped film is such that the thin region is near the first minimum in the periodic thickness *versus* reflected intensity curve and the thick film is close to but less than the nearest maximum. Thus, the intensity varies monotonically with the film thickness, simplifying the interpretation of the images. Using the thin film interference equations to describe the reflected intensity as observed on the CCD detector,²⁷ it is straightforward to obtain w as described in the appendix.

Fig. 4(c) shows the results of several experiments in which stepped films were annealed for approximately 6.6×10^4 s at 180 °C. From the intensity profiles of the monochromatically illuminated optical images the width was obtained as a function of time for three molecular weights (see eqn (6) in the appendix). For all samples studied, $w(t)$ increases quickly for early times, since that is when gradients in the Laplace pressure are the greatest. As the widths become larger, the rate of increase slows as the pressure gradients relax. It is notable that for a given annealing time, the molecular weight of the sample determines the width; larger molecular weights result in smaller widths due to the greater viscous dissipation.

To understand the data presented in Fig. 4(c) quantitatively, we resort to analysis based on the lubrication approximation of the Stokes fluid equations. Extensive reviews on flow in thin fluid films have been written^{25,26} and the evolution equations are developed there in full detail and for systems of much greater generality than we will consider here. Stillwagon and Larson¹⁰ have carried out a detailed derivation of flow in a system that is similar to that described here. Here we quote the final result, while their derivation is outlined in the appendix. Within the lubrication approximation, the width characterizing the transition region between the thin and thick regions of the film grows as a power law in time:

$$w^4 \sim \frac{\gamma h_0^3 t}{\eta}, \quad (2)$$

where η is the viscosity of the fluid under study.

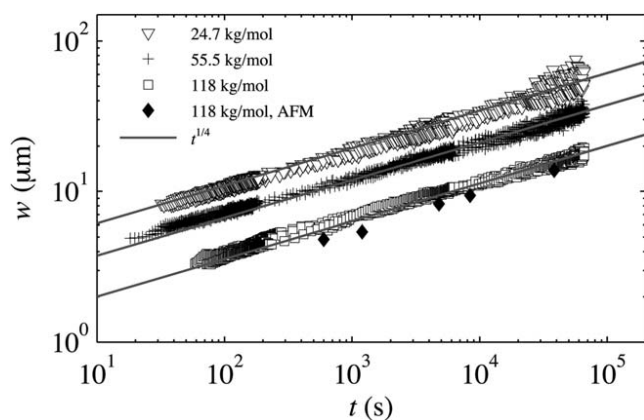


Fig. 5 Logarithmic plots showing w as a function of t for several stepped films. For each molecular weight, the data represent four individual annealed bilayers under similar conditions. Except for the sample that was observed by AFM (\blacklozenge), all samples were observed under an optical microscope.

Comparison to model expectations

In Fig. 5 we show the results of $w(t)$ for all stepped films on a double logarithmic plot in accordance with the prediction of eqn (2). As discussed above, there is some ambiguity in the choice of $t = 0$ because of sample preparation and relaxation of the step prior to commencing the experiment. Furthermore, experimental practicalities dictate that it takes some time to heat from below T_g to 180 °C, to focus the sample, and begin data collection. For this reason all data are fit to the functional form for $w(t)$ with an offset in time to determine the time corresponding to the first width measurement point (*i.e.* shift t , such that when the data is extrapolated to $t = 0$, $w = 0$). The time shifts for all data are reasonable and range from 18 s to 120 s. Clearly this lag time only affects the initial annealing times and is insignificant for annealing times ranging up to tens of hours.

In addition to the optical data, we also show the widths as measured directly from the AFM profiles of Fig. 3. While all optical data was carried out for stepped films with nearly equal values of $h_0 = 148 \pm 3$ nm, the AFM images were obtained on films that were slightly thinner with $h_0 = 136 \pm 2$ nm. Thus the AFM data was scaled by the factor $(148/136)^3$ in accordance with eqn (2). The agreement between the AFM and optical data for the 118 kg mol⁻¹ PS provides a further verification of the measurement and eqn (2).

Eqn (2) predicts that the measured width of annealing bilayers should increase with time as a power law, $w(t) = bt^{1/4}$. The solid gray lines in Fig. 5 are best fits to the data using b as the only fitting parameter for each molecular weight. The data is well represented by the expected power law dependence. As pointed out by Mullins,²⁸ there are additional surface and volume diffusion processes that may contribute to the evolution of the steps, especially in the case of small molecule liquid systems. Below we present analyses which supports the idea that bulk flow is a dominant mechanism for the results presented in Fig. 3–7.

The result from the lubrication approximation also predicts that the prefactor, b , should decrease with the viscosity as $\eta^{-1/4}$. The prefactor also contains dependence on γ and h_0 , but only the molecular weight, and hence the viscosity, varies between data

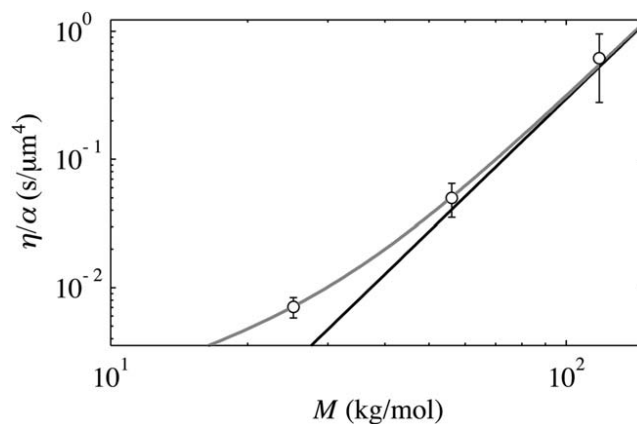


Fig. 6 Scaled viscosities, η/α , as a function of molecular weight obtained from the data in Fig. 5. The grey curve is the best fit of eqn (3), which describes $\eta(M)$ in the crossover region from Rouse dynamics ($\eta \sim M$) to the reptation dynamics in the entangled melt $\eta \sim M^{3.4}$. The black curve represents the long chain reptation regime.

sets in Fig. 5. Therefore, we can write $b = (\alpha/\eta)^{1/4}$, with α a constant. Since the viscosity of a polymer melt varies with molecular weight, M , in a well established manner,²⁹ it is possible to verify the scaling of the data with M as suggested by eqn (2).

In Fig. 6 we show the values of η/α as a function of the molecular weight, where η/α was obtained from the best fits to the data in Fig. 5. Since α is independent of the molecular weight, the ratio η/α should follow the well established dependence of the melt viscosity as a function of M (see the text by Rubinstein and Colby²⁹). For chains much shorter than the critical molecular weight, M_c , the viscosity of a polymer melt is dominated by the Rouse model. In this regime $\eta \sim M$. On the other hand, for $M \gg M_c$, entanglement effects are most important and in this regime it is found that $\eta \sim M^{3.4}$. It turns out that for polystyrene, the critical molecular weight is approximately $M_c \approx 31 \text{ kg mol}^{-1}$.³⁰ Therefore, the molecular weights used in this study are in neither asymptotic regime. In the crossover regime the viscosity is well described by²⁹

$$\eta \sim M \left[1 + \left(\frac{M}{M_c} \right)^{2.4} \right] \quad (3)$$

which smoothly joins the two asymptotic limits. Eqn (3) assumes that our experiments probe only the zero shear rate viscosity. This assumption is justified here by ensuring that our strain rate is well below that for which shear thinning becomes important.†

The gray solid line in Fig. 6 shows the best fit curve to the η/α data using eqn (3). In this fit there is only one free parameter in the expression $\eta/\alpha = \zeta M [1 + (M/M_c)^{2.4}]$. We find $\zeta = 1.8 \pm 0.5 \times 10^{-4} \text{ mol s kg}^{-1} \mu\text{m}^4$. Also shown (black line) is the extrapolated high molecular weight asymptotic limit with $\eta \sim M^{3.4}$. The agreement with the expected functional form is excellent, providing further evidence that the technique is a robust probe of viscosity in thin polymer films. As noted above, the prefactor, b , of eqn (2) contains dependence on the height, the surface tension of the films, and a numerical constant. Taking the height as h_0 , using the surface tension of polystyrene³³ and bulk viscosities³² corrected for temperature using the WLF equation,²⁹ we can extract an estimate of the numerical constant by considering the data in Fig. 6. Eqn (2) is thus empirically determined to be $w^4 = (9 \pm 2)\gamma h_0^3/t\eta$ for these experiments.

Having demonstrated that the experimental results are well described by the expected dependence of the width of the transition on time and viscosity through the use of eqn (2) and (3), it is possible to produce a master curve of all the w versus t data in Fig. 5. In Fig. 7 we show all measured widths plotted as a function of $\alpha t/\eta$ with the scaling factors as in Fig. 6. The data collapses onto a single master curve that spans five orders of magnitude in scaled time and more than one order of magnitude in the width. The existence of such a curve allows the levelling times of geometrically similar films annealed at 180 °C to be

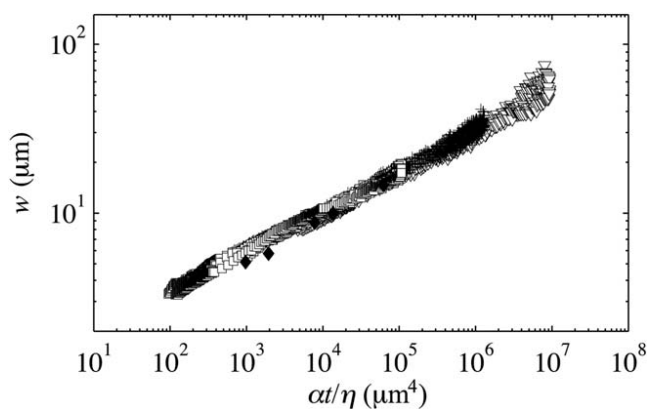


Fig. 7 Measured widths as defined in eqn (6) as a function of the scaled time $\alpha t/\eta$. The symbols are as in Fig. 5.

predicted for a range of molecular weights (viscosities) using eqn (3). Eqn (3) can be used only when the assumption that polymers are in their bulk configuration is valid. This assumption is valid for the films studied here which are much thicker than the radius of gyration of the molecules studied. Polymers in confinement can be investigated by preparing films that are much thinner than the radius of gyration. Preliminary measurements indicate that an observable departure from the bulk expectation (eqn (3)) can be measured using this technique. Measurements of this type will be the subject of a future work.

We end the discussion with a short comparison of our experiment with dewetting experiments of the type that were briefly discussed in the introduction. The rheological studies in which a thin liquid film dewets a substrate have made major contributions to the understanding of many fundamental aspects of polymer science. However, by the very nature of the dewetting problem, it depends on the presence of a surface that is unfavourable for the homogenous liquid that rests upon it. The approach presented here addresses some of the limitations of dewetting studies. While we have focussed on simple homogenous polymer films, by simply changing the two individual films used to prepare the stepped bilayers, it is straightforward to study a wide variety of two component systems. For example the molecular weight, chain architecture, or even the chemical species of the two films that make up the stepped geometry need not be the same. Additionally, the excellent resolution of the film thickness over large length scales possible with optical microscopy under monochromatic illumination provides further opportunities. In particular, measurements of $w(t)$ on films with a constant step height h_2 , and varying thin region h_1 , are sensitive to the polymer substrate boundary condition (*i.e.* lubrication approximation and slip effects). In contrast, varying the step height while keeping the underlying film constant is sensitive to the polymer air interface—a topic that has received tremendous recent attention.

Conclusion

Here we have presented an experimental methodology for the measurement of rheological properties of thin polymer films. Through relatively simple sample preparation procedures, stepped bilayer films are prepared in the glassy state by floating a film with thickness h_2 to partially cover a film of the same polymer with thickness h_1 supported on a substrate. The height profile varies along a line providing a simple

† The dimensionless shear strain rate to be considered is³¹ $\beta = \eta M \dot{\epsilon} / \rho R T$ where $\dot{\epsilon}$ is the shear strain rate, ρ is the mass density and R is the molar gas constant. The largest strain rate in our experiments can be estimated from the early time data of Fig. 4 as $\dot{\epsilon} = \Delta w/h_0 \Delta t \approx 0.1 \text{ s}^{-1}$ for 118 kg mol^{-1} . Using the known viscosity at the temperature at which the experiment is carried out³² an estimate of β can be made. Here β never exceeds 0.02. Since the viscosity is independent of $\dot{\epsilon}$ for $\beta < 1$,³¹ a zero shear rate viscosity is probed in the measurements presented.

flow experiment when the sample is brought into the melt regime. For these thin films gravitational effects can be neglected and the flow is only driven by the Laplace pressure caused by the curvature at the step. The geometry is analytically and experimentally convenient, as well as easy to prepare. Optical microscopy with the sample illuminated by monochromatic light proves to be a simple way to measure the width of the transition from the thin to thick regions of the film. In this first investigation, we have focussed on a well characterized and understood problem: the molecular weight dependence of bulk polymer viscosity. It was shown that the method can be used to measure the differences in the viscosity of a polymer melt as the molecular weight changes. While this study establishes the stepped film geometry as a robust system for the measure of rheological properties in thin films, we are hopeful that the technique will motivate future experiments on more exotic systems.

Appendix

Obtaining $w(t)$ from optical measurements

While in practice one could empirically obtain the calibration factor that translates from a gradient in intensity to a gradient in thickness, here we have used a more rigorous approach. Using thin film equations to describe the reflected intensity as observed on the CCD detector, we can get a measurement of w . Since the height profiles of the thin films are always slowly varying with position we assume that the reflected intensity, I , at position x is a function only of the local height, that is $I = I(h)$. For a uniform transparent film the reflectance is given by²⁷

$$R(h) = \frac{A - B + C \cos(2kh)}{A + B + C \cos(2kh)}, \quad (4)$$

with,

$$\begin{aligned} A &= (n_a^2 + n_p^2)(n_p^2 + n_s^2), \\ B &= 4n_a n_p n_s, \\ C &= (n_a^2 - n_p^2)(n_p^2 - n_s^2), \\ k &= 2\pi n_p / \lambda, \end{aligned}$$

where the wavelength, $\lambda = 633$ nm, is determined by the choice of optical filter, n_a , n_p and n_s are the refractive indices of the air, PS and substrate (here we have taken $n_a = 1$, $n_p = 1.56$ and $n_s = 3.9$). For all of the experiments reported here, the only variable is the film thickness and all other parameters in eqn (4) can be taken as constant. Since even at minimum reflectance there is some background light that makes it to the detector, we model the intensity at the CCD as

$$I(h) = I_b + I_r R(h), \quad (5)$$

where I_b and I_r are fitting parameters. We note that prior to any analysis of the surface profiles (Fig. 4(a) and (b)), the standard PS films with known thicknesses were imaged, their average intensity plotted as a function of h , and the data fit to $I(h)$ to determine the fitting parameters I_b and I_r . This procedure ensured a quick and robust calibration of the relationship between intensity and film thickness. Once calibration images were obtained, all measurements on the stepped films were carried out with the same exposure time and light intensity.

From the definition of the width of the transition in the stepped films as given by eqn (1) and using eqn (4) and (5), we get

$$w \equiv h_2 (\partial_x h|_{x_0})^{-1} = h_2 \left(\frac{\partial_x I|_{x_0}}{I_r \partial_h R|_{h_0}} \right)^{-1}. \quad (6)$$

All derivatives are evaluated at the position where the height of the film is exactly half way along the step (x_0 , h_0). All the quantities on the right hand side of eqn (6) are easily accessible in the measurements performed, and the gradient of the intensity half way up the step, $\partial_x I|_{x_0}$, is the only time dependent quantity. This method of determining the widths can be used when $w \geq \lambda$. For the setup we have used, we can measure widths larger than approximately 1 μm . As seen in Fig. 4(c), none of the widths reported in this study violate this limitation.

Scaling prediction for $w(t)$ from the lubrication approximation

The following calculation is done in greater generality elsewhere,^{10,25,26} but for completeness we outline the main steps in the derivation of the scaling of the width of the transition region with time, $w(t)$. Here, we do not consider gravitational or long range (e.g. van der Waals) forces, evaporation/condensation, or surface tension gradients. Stillwagon and Larson¹⁰ have derived, and experimentally verified, the flow equations based on the lubrication approximation for substrate topographies that are not necessarily flat. Their detailed calculation can be further simplified because our substrates are flat. For the system discussed here, all of the above assumptions are valid and the Stokes equation for the flow in one dimension is

$$0 = \partial_x p + \eta \partial_z^2 u, \quad (7)$$

where p is the pressure, η is the viscosity, u is the velocity in the horizontal direction and z is the vertical coordinate. Assuming no slip at the boundary between the film and the substrate, that there is no stress supported at the air–polymer interface, and that the pressure does not vary in the vertical direction, a parabolic velocity profile in the z -direction results.^{10,24} Since the velocity profile is quadratic with respect to the vertical coordinate and assuming an incompressible fluid, the volume flow rate is cubic in the local film height, $h(x)$. With eqn (7) we then obtain the volume flow rate per unit film width $Q = -h^3 \partial_x p / 3\eta$. The pressure is the product of the surface tension and the curvature at the air–polymer interface. Since $\partial_x h \ll 1$ for all the samples observed under optical microscopy, the pressure is well approximated by $p = \gamma \partial_x^2 h$. Imposing conservation of mass gives an evolution equation for the height profile as a function of time. For the system we are considering, the lubrication approximation for the temporal evolution of this height profile is

$$\partial_t h = \frac{\gamma}{3\eta} \partial_x (h^3 \partial_x^3 h). \quad (8)$$

Nondimensionalizing eqn (8) gives a relevant time scale that is a function of the relevant length scales, the surface tension and the viscosity: $t \approx w^4 \eta / \gamma h_0^3$. Upon rearranging for the width

$$w^4 \approx \frac{\gamma h_0^3 t}{\eta}, \quad (9)$$

as shown in eqn (2). Here we have assumed that the relevant height scale in the problem is h_0 , while the x direction it is the width, w .

Acknowledgements

Financial support from NSERC of Canada is gratefully acknowledged. The authors thank Professors J. A. Forrest and A.-C. Shi for valuable discussions.

References

- 1 F. Brochard Wyart and J. Daillant, *Can. J. Phys.*, 1990, **68**, 1084.
- 2 G. Reiter, *Phys. Rev. Lett.*, 1992, **68**, 75.
- 3 R. Seemann, S. Herminghaus and K. Jacobs, *Phys. Rev. Lett.*, 2001, **87**, 196101.
- 4 J. Becker, G. Grün, R. Seemann, H. Mantz, K. Jacobs, K. Mecke and R. Blossey, *Nat. Mater.*, 2002, **2**, 59–63.
- 5 S. Gabriele, S. Slavovs, G. Reiter and P. Damman, *Phys. Rev. Lett.*, 2006, **96**, 2006.
- 6 D. Bonn, J. Eggers, J. Indekeu, J. Meunier and E. Rolley, *Rev. Mod. Phys.*, 2009, **81**, 739.
- 7 O. Baumchen, R. Fetzer and K. Jacobs, *Phys. Rev. Lett.*, 2009, **103**, 247801.
- 8 G. Reiter, S. Akhrass, M. Hamieh, P. Damman, S. Gabriele, T. Vilmin and E. Raphaël, *Eur. Phys. J. Spec. Top.*, 2009, **166**, 165.
- 9 A. Raegen, M. Chowdhury, C. Calers, A. Schmatulla, U. Steiner and G. Reiter, *Phys. Rev. Lett.*, 2010, **105**, 227801.
- 10 L. Stillwagon and R. Larson, *J. Appl. Phys.*, 1988, **63**, 5251.
- 11 T. Kerle, Z. Lin, H.-C. Kim and T. Russell, *Macromolecules*, 2001, **34**, 3484.
- 12 E. Buck, K. Petersen, M. Hund, G. Krausch and D. Johannsmann, *Macromolecules*, 2004, **37**, 8647–8652.
- 13 T. Leveder, S. Landis and L. Davoust, *Appl. Phys. Lett.*, 2008, **92**, 013107.
- 14 Z. Fakhraai and J. Forrest, *Science*, 2008, **319**, 600.
- 15 D. Barbero and U. Steiner, *Phys. Rev. Lett.*, 2009, **102**, 248303.
- 16 M. Ilton, D. Qi and J. Forrest, *Macromolecules*, 2009, **42**, 6851–6854.
- 17 J. Teisseire, A. Revaux, M. Foresti and E. Barthel, *Appl. Phys. Lett.*, 2011, **98**, 013106.
- 18 P. de Gennes, *Rev. Mod. Phys.*, 1985, **57**, 287.
- 19 V. Shenoy and A. Sharma, *Phys. Rev. Lett.*, 2002, **88**, 236101.
- 20 T. Vilmin and E. Raphaël, *Europhys. Lett.*, 2005, **72**, 781.
- 21 G. Debrégeas, P. Martin and F. Brochard-Wyart, *Phys. Rev. Lett.*, 1995, **75**, 3886–3889.
- 22 K. Dalnoki-Veress, B. Nickel, C. Roth and J. Dutcher, *Phys. Rev. E*, 1999, **59**, 2153.
- 23 C. Roth and J. Dutcher, *J. Polym. Sci., Part B: Polym. Phys.*, 2006, **44**, 3011.
- 24 P. de Gennes, F. Brochard-Wyart and D. Quéré, *Capillarity and Wetting Phenomena: Drops, Bubbles, Pearls, Waves*, Springer, 2003, vol. 1.
- 25 A. Oron, S. Davis and S. Bankoff, *Rev. Mod. Phys.*, 1997, **69**, 931.
- 26 R. Craster and O. Matar, *Rev. Mod. Phys.*, 2009, **81**, 1131.
- 27 O. Heavens, *Rep. Prog. Phys.*, 1960, **23**, 1.
- 28 W. Mullins, *J. Appl. Phys.*, 1959, **30**, 77.
- 29 M. Rubinstein and R. Colby, *Polymer Physics*, Oxford University Press, 2003.
- 30 L. Fetters, D. Lohse, S. Milner and W. Graessley, *Macromolecules*, 1999, **32**, 6847.
- 31 W. Graessley, *Adv. Polym. Sci.*, 1974, **16**, 1.
- 32 T. Fox and P. Flory, *J. Am. Chem. Soc.*, 1948, **70**, 2384.
- 33 D. Schrader, *Polymer Handbook*, John Wiley & Sons, Inc., 1999, vol. 4, ch. V, p. 91.

Manuscript ii

Self-Similarity and Energy Dissipation in Stepped Polymer Films

J.D. McGraw, T. Salez, O. Bäumchen, E. Raphaël and K. Dalnoki-Veress, *Physical Review Letters*, **109**, 128303 (2012).

Self-Similarity and Energy Dissipation in Stepped Polymer Films

Joshua D. McGraw,¹ Thomas Salez,² Oliver Bäumchen,¹ Elie Raphaël,² and Kari Dalnoki-Veress^{1,*}

¹*Department of Physics and Astronomy and the Brockhouse Institute for Materials Research, McMaster University, Hamilton, Canada*

²*Laboratoire de Physico-Chimie Théorique, UMR CNRS Gulliver 7083, ESPCI, Paris, France*

(Received 15 May 2012; revised manuscript received 4 July 2012; published 18 September 2012)

The surface of a thin liquid film with a nonconstant curvature is unstable, as the Laplace pressure drives a flow mediated by viscosity. We present the results of experiments on one of the simplest variable curvature surfaces: a thin polymer film with a step. Height profiles are measured as a function of time for a variety of molecular weights. The evolution of the profiles is shown to be self-similar. This self-similarity offers a precise measurement of the capillary velocity by comparison with numerical solutions of the thin film equation. We also derive a master expression for the time dependence of the excess free energy as a function of the material properties and film geometry. The experiment and theory are in excellent agreement and indicate the effectiveness of stepped polymer films to elucidate nanoscale rheological properties.

DOI: [10.1103/PhysRevLett.109.128303](https://doi.org/10.1103/PhysRevLett.109.128303)

PACS numbers: 47.57.Ng, 47.55.nb, 66.20.Cy, 68.55.am

The properties of polymers and indeed all molecules in thin films and at interfaces continue to stimulate debate. The apparent increased mobility of polymers at interfaces in both the liquid [1,2] and glassy states [3], their structural properties [4,5], as well as the effects of preparation and treatment history [6–9] are areas of concerted effort. While length scales of these systems are frequently just a few molecular diameters, the physics governing their liquid state evolution is quite general and can be used to model, for example, geophysical flows [10].

When a flat liquid film is in contact with a substrate of lower surface energy, a hole can nucleate to expose some of the underlying surface. This phenomenon induces a non-constant curvature of the film driven by interfacial tension and leads to a decrease of the total free energy as the hole grows. This process is called dewetting [11,12]. There have been many studies concerned with details of the shape and evolution of the rim which collects the dewetted fluid [5,13–19], and much has been learned about and from the process of turning a flat film into a collection of droplets.

Several techniques that have been used [20–26] to provide insight into the aforementioned problems [1–9] take the opposite approach. They rely on the property that curved interfaces have more surface area than flat ones. Such curved surfaces can be driven to flatten by the surface tension, γ , but are mediated by the viscosity, η . In several of the surface tension-driven flow techniques, the nanoscale topography is imprinted using a square wave pattern that varies in one lateral dimension only [23–26]. In these studies, the authors typically consider the evolution of the amplitude of the perturbation, rather than that of the profile shape. As in many of the dewetting studies, this Letter is concerned with the details of a capillary-driven flow profile, but in a different geometry: a *stepped film*.

In a previous contribution [22], we explained how to prepare the simple geometry of stepped polymer films. The samples are prepared as schematically shown in Fig. 1(a). They are comparable to the square wave patterns discussed above [23–26] in that the height is a function of only one spatial dimension and time, $h = h(x, t)$. They are different in that they have only one height step. This two-dimensional geometry allows us to study the broadening in the region over which the height changes from h_1 to $h_1 + h_2$ (see Fig. 1) in isolation, rather than having to consider the flow from neighboring steps in a periodic geometry. With the use of scaling laws, it was shown that by measuring a particular lateral length scale, one could measure the relative viscosity [22]. In this Letter, we provide a theoretical treatment of the governing thin film equation which is in agreement with the measured height profiles over a wide range of thickness combinations and over several orders of magnitude in viscosities. We explain in detail the dependence of the energy dissipation on the film geometry and capillary velocity, γ/η .

Films were prepared by spin coating polystyrene (PS) dissolved in toluene onto two types of substrates: $1 \times 1 \text{ cm}^2$ Si wafers (University Wafer) rinsed with ultra-pure water (18.2 M Ω cm, Pall, Cascada LS), methanol, and toluene (Fisher Scientific, Optima grade), as well as

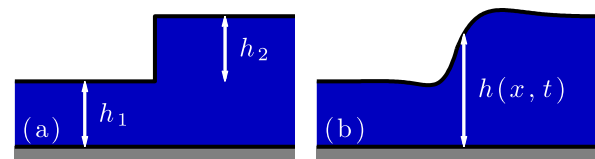


FIG. 1 (color online). (a) Schematic of the as-prepared samples. (b) After annealing above the glass transition temperature, the region of transition between the two terrace heights broadens, and a flow profile can be measured.

freshly cleaved mica substrates (Ted Pella, Inc.). The PS molecular weights were $M_w = 15.5, 55.5, 118,$ and 192 kg/mol with polydispersity indices ≤ 1.07 (Polymer Source, Inc.). The film thicknesses ranged from 30 to 200 nm. These heights were always much larger than the typical size of molecules making up the films. The as-cast samples were annealed at 130°C in a vacuum oven (10^{-5} mbar) for 24 h (more than 2 orders of magnitude greater than the longest relaxation time of the largest polymer used [27]).

The preparation of stepped films proceeded as detailed previously [22]. Briefly, PS films with thickness h_2 on a mica substrate were floated onto ultrapure water and transferred to a Si wafer. After drying, these wafers were split along a crystal axis. The split films were again floated onto water and picked up using a Si wafer coated with a PS film of height h_1 , thus creating a bilayer with step size h_2 (see Fig. 1). Samples are described as having geometry $\{h_1, h_2\}$. All sections of film observed in this study had straight edges as viewed with optical and atomic force microscopy (AFM, Veeco Caliber) for distances of a minimum of $50\ \mu\text{m}$. Figure 2(a) at $t = 0$ illustrates an example of the initial stepped profile; see also Ref. [22].

Prior to measurement of each profile evolution, h_2 was measured (as with all heights reported) using AFM. Then, the film was annealed for 10 min at 140°C on a hot stage (Linkam) using a heating rate of $90^\circ\text{C}/\text{min}$ in air [28]. After cooling to room temperature ($\sim 40^\circ\text{C}/\text{min}$ to below the glass transition, $T_g \sim 100^\circ\text{C}$), the step profile was measured. Given $h(x, t)$ as the distance between the substrate-polymer and air-polymer interfaces, $h(x, t) - h_1$

is the quantity measured. For the 55.5, 118, and 192 kg/mol samples, additional annealing for 10 min periods was performed, with the profile evolution obtained at room temperature. After a final measurement of the height profile, a scratch in the PS film was made down to the substrate to measure h_1 .

Figure 2(a) shows the time evolution ($10 \leq t \leq 300$ min) of three stepped polymer films with $h_1 \approx h_2 \approx 100$ nm, each with a different molecular weight. On each stepped film, there is a prominent “dip” on the thin side of the film and a “bump” on the thick side, which is consistent with our earlier observations [22] and can also be seen in the long wave limit of the data presented by Rognin *et al.* [25]. The evolution proceeds such that positions of the profile extrema are separated over wider distances: the film flattens with time.

The flow profile can be understood from the Laplace pressure, which arises due to curvature at the fluid interface [29]; the range of heights considered here allows us to neglect gravitational [10] and disjoining [30] pressures. Assuming that the height gradients are small, the lubrication approximation applies, and the local Laplace pressure is given by $p(x, t) \approx -\gamma \partial_x^2 h$. Though the as-prepared stepped films have steep gradients, they also contain large curvature gradients in the same regions. These high-gradient regions then flow quickly compared to the experimental annealing times, and the lubrication approximation is valid for all experiments presented here. As a stepped film levels, the bump represents a region of high pressure relative to the flat regions on the thick side of the film, while the dip has a low pressure relative to flat regions on

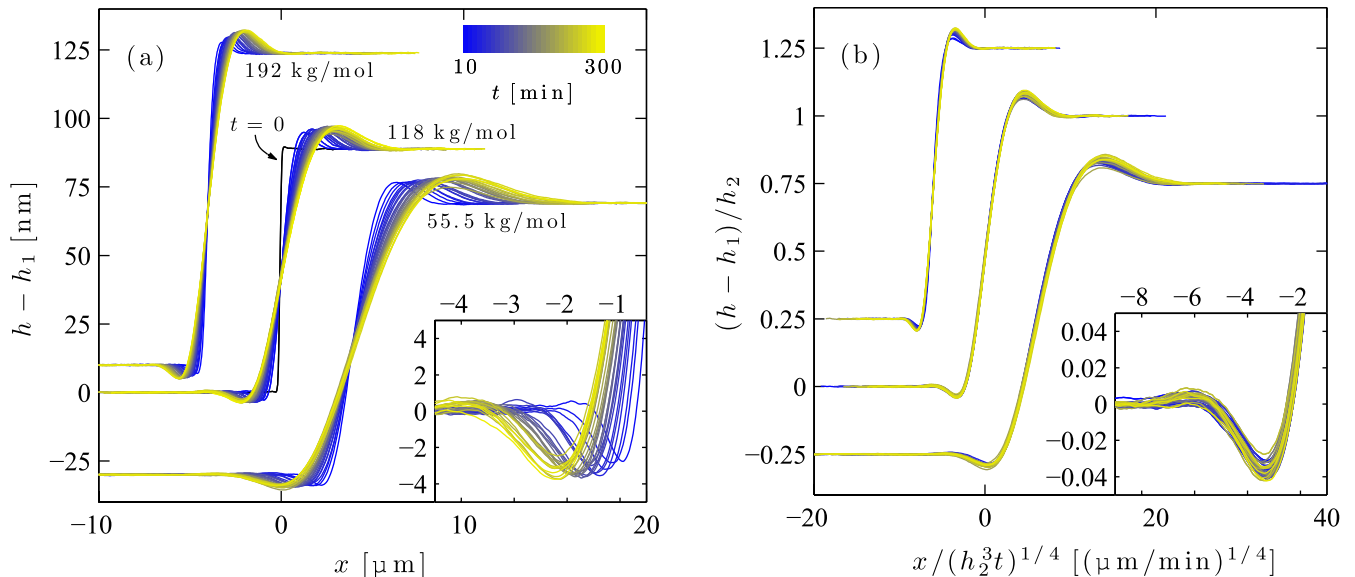


FIG. 2 (color online). (a) Height as a function of position and time ($10 \leq t \leq 300$ min) for three stepped films with molecular weights as indicated. From left to right, $\{h_1, h_2\} = \{106, 114\}, \{89, 89\},$ and $\{101, 99\}$ nm. The inset shows a detail of the “dip” region for the 118 kg/mol sample. (b) Scaled height as a function of scaled position, according to Eq. (2); the inset shows the same region as the inset of panel (a) in scaled variables. Whereas the volume constraint uniquely determines the origin, the 192 and 55.5 kg/mol data have been shifted both horizontally and vertically in both (a) and (b) for clarity.

the thin side. Thus, there are pressure gradients along the region of transition between h_1 and $h_1 + h_2$, and the flow continues.

To understand the data of Fig. 2(a) quantitatively, we combine the lubrication approximation and the Stokes equation of viscous flows that leads [31–33] to $\partial_x p = \eta \partial_z^2 v$, where $v(x, z, t)$ is the horizontal velocity and z is the vertical coordinate. Since the longest relaxation time of any polymer used here is of order 100 s, and all leveling times are significantly longer than this time, viscoelastic effects can safely be neglected. Assuming no slip at the solid-liquid interface and no stress at the liquid-air interface gives a Poiseuille velocity profile along z . Invoking conservation of volume and using the Laplace pressure introduced above leads to the thin film equation

$$\partial_t h + \frac{\gamma}{3\eta} \partial_x (h^3 \partial_x^3 h) = 0. \quad (1)$$

This differential equation can be nondimensionalized by letting $H = h/h_2$, $X = x/x_0$, and $T = \gamma h_2^3 t / 3\eta x_0^4$, where x_0 is a typical horizontal length scale of the problem [31]. Furthermore, introducing the variable

$$U = \frac{X}{T^{1/4}} = \left(\frac{3\eta}{\gamma}\right)^{1/4} \frac{x}{(h_2^3 t)^{1/4}}, \quad (2)$$

one can show that self-similar solutions of the first kind of the form $H(X, T) = F(U)$ exist [10,34–36]. Using a numerical scheme [37,38], we have shown that this self-similarity is satisfied for times $T \gtrsim 10^{-4}$ for a profile with $h_1 = h_2$. We have furthermore verified that the self-similarity is not sensitive to the initial height profile, provided that the heights at $U = \pm\infty$ are constant and different. Therefore, if the interface profile is self-similar, a rescaling of the horizontal axis must collapse all of the experimental data. In Fig. 2(b), we show the same data as in Fig. 2(a) but plotted as a function of $x/(h_2^3 t)^{1/4}$. Having done so, we see that the data for all three molecular weights do collapse onto three individual curves, thus demonstrating the self-similarity of the evolution through time. Examining the scaled curve for the 192 kg/mol PS in Fig. 2(b) closely, one can see that the early time data do not collapse perfectly onto one single curve. This result is due to the fact that it takes longer times to reach the self-similar solutions to Eq. (1) for higher molecular weights, at a given temperature.

In the previous rescaling, the horizontal length scale characterizing the transition between undisturbed film heights is different for each of the three data sets. Since the samples all started with the same initial condition, they have different leveling speeds because the viscosity varies with M_w . To obtain precise measurements of these leveling speeds, we numerically solve the dimensionless form of Eq. (1) with a stepped initial condition of aspect ratio $r = h_1/h_2$. We then fit the computed self-similar profile, $F_r(U)$, to the corresponding rescaled experimental

profile. Figures 3(a) and 3(b) show the rescaled measured profiles for two 15 kg/mol PS stepped films with different $\{h_1, h_2\}$ values as well as the corresponding fits to the numerical solutions of Eq. (1) [38]. Despite the initial transient flow not described by the lubrication approximation, all experimental profiles presented here approach the self-similar solutions obtained from Eq. (1). In the fitting procedure, the only free parameter is a horizontal stretch of the computed profile given by the factor $(\gamma/3\eta)^{1/4}$ according to Eq. (2). This procedure thus yields a measured value of the capillary velocity γ/η . Using $\gamma \approx 30 \text{ mJ/m}^2$ [39] for all polymers here, we get $\eta = 7.3 \times 10^3$, 1.4×10^5 , 1.1×10^6 , and $9.1 \times 10^6 \text{ Pa s}$ for $M_w = 15.5$, 55.5, 118, and 192 kg/mol PS at 140 °C. These viscosities follow the expected molecular weight dependence of the polymer melt viscosity [40] and are in agreement with viscosities measured in the bulk [27]. We have measured η/γ for nine additional 15.5 kg/mol PS stepped films all with different $\{h_1, h_2\}$ values. We find that the value obtained is independent of $\{h_1, h_2\}$, and the ratio of the standard deviation to the mean is 0.12.

Having exhibited the self-similarity of the profiles and having set up a robust method to measure the capillary velocity, we now turn to the study of the dissipation law in stepped films. The excess free energy per unit length along the dimension of invariance, $\Delta\mathcal{F}$, is dominated by the interfacial contribution. For small slopes

$$\Delta\mathcal{F} = \gamma\Delta L \approx \frac{\gamma}{2} \int dx (\partial_x h)^2, \quad (3)$$

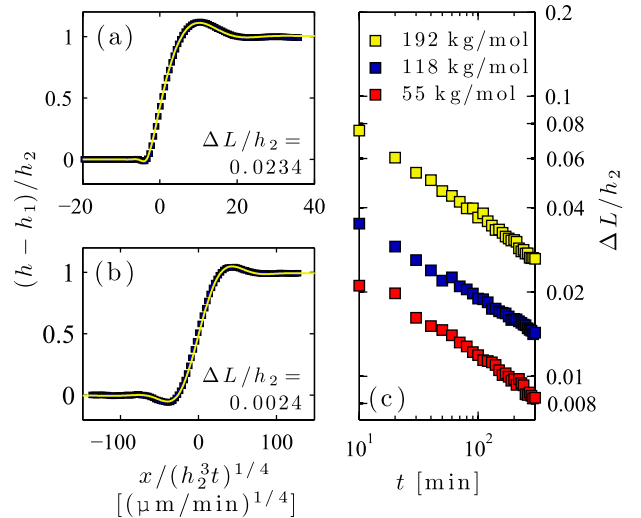


FIG. 3 (color online). (a) Rescaled measured profiles for a 15 kg/mol PS stepped film with $\{h_1, h_2\} = \{30, 193\}$ nm after 10 min of annealing at 140 °C; (b) an identically annealed stepped film with $\{h_1, h_2\} = \{174, 32\}$ nm. The lines in (a) and (b) are horizontally stretched numerical solutions from Eq. (1) using Refs. [37,38]. (c) Relative excess contour length of the data in Fig. 2 as a function of time; see Eq. (3).

where ΔL is the excess contour length of the profile with respect to the flat limit at infinite time. In Fig. 3(c), we plot the relative excess length as a function of time for the three samples of Fig. 2(b). It is evident that the individual data sets obey a power law in time. Referring also to the two stepped films shown in Figs. 3(a) and 3(b), we see that the contour lengths of these two profiles are not identical despite having been annealed under the same conditions. Therefore, there are temporal and geometrical dependencies on the energy dissipation.

In the following, we develop a theoretical model in order to understand the results of Fig. 3. Making the quantities in the integrand of Eq. (3) dimensionless as presented above and invoking the self-similarity of the profile, we find that the relative excess length remaining after time t satisfies

$$\Delta L = C(r) \left(\frac{\eta h_2^5}{\gamma t} \right)^{1/4}, \quad (4a)$$

$$\text{with } C(r) = \frac{3^{1/4}}{2} \int dU [F_r'(U)]^2, \quad (4b)$$

where $C(r)$ is determined by the sample geometry through the dimensionless self-similar profile $F_r(U)$.

The stepped film problem contains three relevant combinations of heights: h_2 for the step height, which provides the typical driving force for leveling, as well as h_1 and $h_1 + h_2$ for the thicknesses of the thin and thick regions of the film. Thus, having already extracted the h_2 dependence in Eq. (4a), the simplest ansatz for a height dependence of $C(r)$ is a power law of the form

$$C(r) = C(1) r^\alpha \left(\frac{1+r}{2} \right)^\beta. \quad (5)$$

This scaling expression connects the case of arbitrary aspect ratio, r , to the $r = 1$ geometry; normalization to $r = 1$ is ensured by the factor of 2. In order to determine the two exponents, we consider the limit $r \gg 1$, where the step is a small perturbation of the flat film. In this limit, Eq. (1) can be linearized and solved analytically and we find $C(r) \approx \xi r^{-3/4}$, where $\xi \approx 0.16$ [41]. By comparison to Eq. (5) when $r \gg 1$, we get $\alpha + \beta = -3/4$ and $\beta = \log[C(1)/\xi] / \log(2)$. Then, using the numerical solutions of Eq. (1) presented above, we calculate $C(1) \approx 0.12$ and thus $\beta \approx -0.42$. Finally, we obtain a master expression for the relative excess contour length,

$$\frac{\Delta L}{h_2} = \xi \left(\frac{h_2}{h_1} \right)^{3/4} \left(1 + \frac{h_2}{h_1} \right)^\beta \left(\frac{\eta h_2}{\gamma t} \right)^{1/4}. \quad (6)$$

Figure 4 shows the relative excess lengths for all samples and times presented in this study as a function of the combination of $\{h_1, h_2\}$, γ/η and t suggested by Eq. (6). The solid line corresponds to the theoretical prediction of Eq. (6) with *no free parameter*. The agreement between the data and Eq. (6) validates the dissipation law as well as the general scaling to the $r = 1$ symmetric case, within the range of our experimental data. As discussed above, the

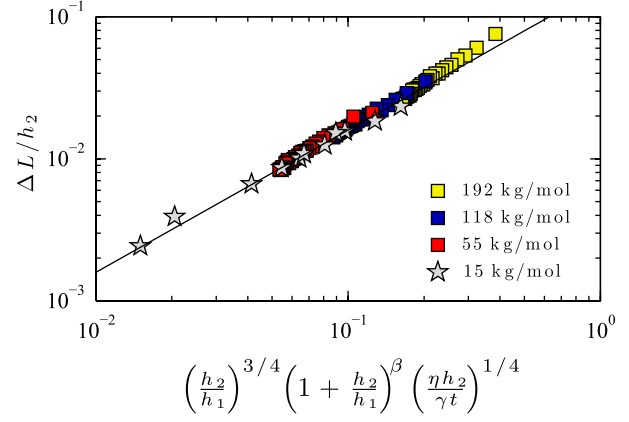


FIG. 4 (color online). Relative excess contour lengths as a function of time and the geometrical and physical parameters of the stepped films. We use $\beta = -0.42$. Data points represent 15 kg/mol films at $t = 10$ min with different $\{h_1, h_2\}$ values ($0.16 < r < 5.6$) and the temporal series in Fig. 3(c). The solid line is the theoretical prediction of Eq. (6) with no free parameter ($\xi = 0.16$).

dissipation law is modified for $t < 100$ min for the 192 kg/mol PS, where self-similarity or the lubrication approximation may not be valid. Although we have not accessed this limit here, we expect deviations when $r \rightarrow 0$, for which the dependency on h_1 may differ.

In conclusion, we have demonstrated that the thin film equation captures the time evolution of stepped polymer films for a wide range of aspect ratios and material properties. With the use of a numerical solution of this equation, it is now straightforward to precisely measure the capillary velocity of any nonvolatile fluid prepared as described. We further demonstrated the self-similarity of the evolution of the profiles. Finally, details of how the excess surface energy is dissipated by viscosity over time have been obtained. We have determined that the surface energy decreases with a $-1/4$ power law in time. The rate at which energy is dissipated depends on the capillary velocity and on the heights of the initial step. In particular, we have shown through a master expression that the evolution of any stepped film can be rescaled to the $h_1 = h_2$ symmetric step.

The authors thank NSERC of Canada, the École Normale Supérieure of Paris, the German Research Foundation (DFG) under Grant No. BA3406/2, the Chaire Total-ESPCI, and the Saint Gobain Fellowship for financial support.

*dalnoki@mcmaster.ca

- [1] K. Shin, S. Obukhov, J.-T. Chen, J. Huh, Y. Hwang, S. Mok, P. Dobriyal, P. Thiyagarajan, and T. Russell, *Nature Mater.* **6**, 961 (2007).
- [2] H. Bodiguel and C. Fretigny, *Phys. Rev. Lett.* **97**, 266105 (2006).

- [3] Z. Fakhraai and J. Forrest, *Science* **319**, 600 (2008).
- [4] L. Si, M. V. Massa, K. Dalnoki-Veress, H. R. Brown, and R. A. L. Jones, *Phys. Rev. Lett.* **94**, 127801 (2005).
- [5] O. Bäumchen, R. Fetzer, and K. Jacobs, *Phys. Rev. Lett.* **103**, 247801 (2009).
- [6] D. R. Barbero and U. Steiner, *Phys. Rev. Lett.* **102**, 248303 (2009).
- [7] A. Raegen, M. Chowdhury, C. Calers, A. Schmatulla, U. Steiner, and G. Reiter, *Phys. Rev. Lett.* **105**, 227801 (2010).
- [8] K. R. Thomas, A. Chenneviere, G. Reiter, and U. Steiner, *Phys. Rev. E* **83**, 021804 (2011).
- [9] R. N. Li, A. Clough, Z. Yang, and O. K. C. Tsui, *Macromolecules* **45**, 1085 (2012).
- [10] H. Huppert, *J. Fluid Mech.* **121**, 43 (1982).
- [11] F. Brochard-Wyart and J. Dailant, *Can. J. Phys.* **68**, 1084 (1990).
- [12] G. Reiter, *Phys. Rev. Lett.* **68**, 75 (1992).
- [13] R. Seemann, S. Herminghaus, and K. Jacobs, *Phys. Rev. Lett.* **87**, 196101 (2001).
- [14] A. Münch, B. Wagner, and T. Witelski, *J. Eng. Math.* **53**, 359 (2005).
- [15] T. Vilmin and E. Raphaël, *Eur. Phys. J. E* **21**, 161 (2006).
- [16] R. Fetzer, A. Münch, B. Wagner, M. Rauscher, and K. Jacobs, *Langmuir* **23**, 10559 (2007).
- [17] G. Reiter, S. Akhrass, M. Hamieh, P. Damman, S. Gabriele, T. Vilmin, and E. Raphaël, *Eur. Phys. J. Special Topics* **166**, 165 (2009).
- [18] J. H. Snoeijer and J. Eggers, *Phys. Rev. E* **82**, 056314 (2010).
- [19] O. Bäumchen, R. Fetzer, M. Klos, M. Lessel, L. Marquant, H. Hähl, and K. Jacobs, *J. Phys. Condens. Matter* **24**, 325102 (2012).
- [20] T. Kerle, Z. Lin, H.-C. Kim, and T. Russell, *Macromolecules* **34**, 3484 (2001).
- [21] E. Buck, K. Petersen, M. Hund, G. Krausch, and D. Johannsmann, *Macromolecules* **37**, 8647 (2004).
- [22] J. D. McGraw, N. M. Jago, and K. Dalnoki-Veress, *Soft Matter* **7**, 7832 (2011).
- [23] J. Teisseire, A. Revaux, M. Foresti, and E. Barthel, *Appl. Phys. Lett.* **98**, 013106 (2011).
- [24] L. Zhu, C. W. Brian, S. F. Swallen, P. T. Straus, M. D. Ediger, and L. Yu, *Phys. Rev. Lett.* **106**, 256103 (2011).
- [25] E. Rognin, S. Landis, and L. Davoust, *Phys. Rev. E* **84**, 041805 (2011).
- [26] E. Rognin, S. Landis, and L. Davoust, *J. Vac. Sci. Technol. B* **30**, 011602 (2012).
- [27] A. Bach, K. Almdal, H. Rasmussen, and O. Hassager, *Macromolecules* **36**, 5174 (2003).
- [28] We have verified that the leveling results are unchanged when annealing in a dry nitrogen atmosphere.
- [29] P.-G. de Gennes, F. Brochard-Wyart, and D. Quéré, *Capillarity and Wetting Phenomena: Drops, Bubbles, Pearls, Waves* (Springer, New York, 2003).
- [30] R. Seemann, S. Herminghaus, and K. Jacobs, *Phys. Rev. Lett.* **86**, 5534 (2001).
- [31] L. Stillwagon and R. Larson, *J. Appl. Phys.* **63**, 5251 (1988).
- [32] A. Oron, S. Davis, and S. Bankoff, *Rev. Mod. Phys.* **69**, 931 (1997).
- [33] R. Craster and O. Matar, *Rev. Mod. Phys.* **81**, 1131 (2009).
- [34] G. I. Barenblatt, *Scaling, Self-Similarity, and Intermediate Asymptotics* (Cambridge University Press, Cambridge, England, 1996).
- [35] A. Aradian, E. Raphaël, and P.-G. de Gennes, *Europhys. Lett.* **55**, 834 (2001).
- [36] M. Bowen and T. P. Witelski, *SIAM J. Appl. Math.* **66**, 1727 (2006).
- [37] A. L. Bertozzi, *Notices Am. Math. Soc.* **45**, 689 (1998).
- [38] T. Salez, J. D. McGraw, S. L. Cormier, O. Bäumchen, K. Dalnoki-Veress, and E. Raphaël, *J. Fluids* (to be published).
- [39] S. Wu, *Polymer Handbook* (Wiley-Interscience, New York, 1999), Vol. 4.
- [40] M. Rubinstein and R. Colby, *Polymer Physics* (Oxford University Press, New York, 2003).
- [41] T. Salez, J. D. McGraw, O. Bäumchen, K. Dalnoki-Veress, and E. Raphaël, *Eur. Phys. J. E* (to be published).

Manuscript iii

Plateau-Rayleigh instability in a torus: formation and breakup of a polymer ring

J.D. McGraw, J. Li, D.L. Tran, A.-C. Shi and K. Dalnoki-Veress, *Soft Matter*, **6**, 1258 (2010).

Plateau-Rayleigh instability in a torus: formation and breakup of a polymer ring

Joshua D. McGraw,^a Jianfeng Li,^{ab} David L. Tran,^a An-Chang Shi^a and Kari Dalnoki-Veress^{*a}

Received 21st September 2009, Accepted 11th December 2009

First published as an Advance Article on the web 29th January 2010

DOI: 10.1039/b919630g

A liquid jet can break up into a stream of droplets as a result of the Plateau-Rayleigh instability. The droplet formation decreases the jet's surface area and hence its free energy. Here we present the results of experiments in an unconventional geometry where this instability can be observed: a toroidal section. We discuss the formation of these polystyrene toroids with nanometer length scales. The constraints imposed by this geometry affect its observed instability in comparison to a simple linear jet. Specifically, we show that the additional curvature imposed by the torus can have a significant impact on the energy minimization route.

Introduction

The Plateau-Rayleigh (P-R) instability is responsible for the breakup that occurs when a long cylindrical fluid body with a free surface is allowed to evolve. A familiar example of this instability can be seen when water flows from a faucet and falls under the influence of gravity;¹ a less familiar example has recently been observed in a falling granular stream.² Near the point of exit a stream is cylindrical. Further away the system lowers its free energy *via* a sinusoidal undulation of the surface which eventually grows to the point of pinching off into a series of droplets. Much effort has been devoted to understanding the breakup of fluid streams in the last century and a half, and a comprehensive review can be found elsewhere.¹ However, comparatively little has even been observed of this effect in geometries other than long straight cylinders.

Recently, the creation and observed breakup of liquid toroids was reported in elegant experiments by Pairam and Fernández-Neives.³ These authors used a novel method of producing macroscopic water toroids suspended in viscous liquids with precise control of the overall ring radius, r , and the radius of the cylinder, a (see schematic in Fig. 1(a)). Pairam and Fernández-Neives carried out a systematic study of the breakup of individual toroids and the dependence on the aspect ratio, r/a . The liquid toroids eventually break up into a number of spherical droplets as a means of decreasing its surface energy. However, for a torus, the wavelength of the instability must be commensurate with the tube's circumference. This additional constraint imposed by the geometry of a torus undergoing the P-R instability was observed by Pairam and Fernández-Neives.³

Owing to the fact that a liquid torus is unstable, the difficulty in preparing them is noteworthy. Pairam and Fernández-Neives prepared toroids with a water filled needle immersed in a rotating bath of an immiscible viscous liquid.³ Recently it was shown that

a torus can form as a droplet falls in air as a result of the interactions between the droplet and its surrounding atmosphere. Interestingly, the breakup of that torus has a role to play in determining the distribution of drop sizes during rainfall.⁴ For these formation mechanisms, the short time interval between formation and breakup is the limiting factor in making observations on a torus. As we will show, an advantage of polymeric systems is that it is possible to prepare toroids in the glassy state which can then transition into the melt state in an easily controllable manner. The ability to transition from the melt to the glassy state enables observation of the toroids at any stage of the breakup process.

Here we report a method of preparing solid polystyrene (PS) toroids with micron sized ring radii and nanoscale cylinder radii. The method produces a collection of solid toroidal sections on a substrate with various aspect ratios. A typical example of such a toroidal section, before and after the P-R instability, is shown in the atomic force microscopy (AFM) topography images of

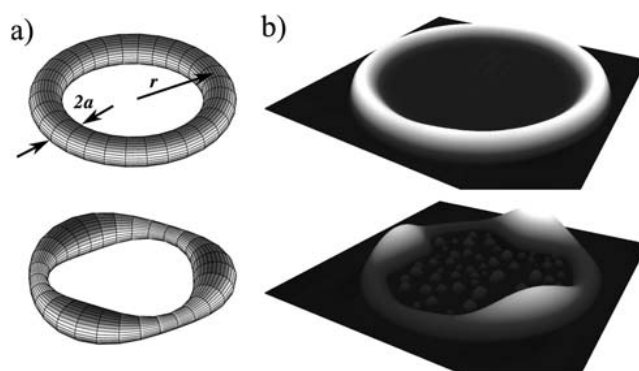


Fig. 1 (a) Schematic of a torus where r is the overall radius of the ring and a is the radius of the cylinder. Also shown is an intermediate stage of a liquid torus undergoing surface undulations due to the Plateau-Rayleigh instability. (b) AFM topography images analogous to the schematics shown in (a). For this example the polystyrene ring has a diameter of $28.5\ \mu\text{m}$ and toroidal section has a height of $135\ \text{nm}$. Note that the small droplets inside the ring are the result of a very thin film that has dewetted.

^aDepartment of Physics & Astronomy and the Brockhouse Institute for Materials Research, McMaster University, Hamilton, Canada. E-mail: dalnoki@mcmaster.ca

^bDepartment of Macromolecular Science, Fudan University, Shanghai, 200433, China

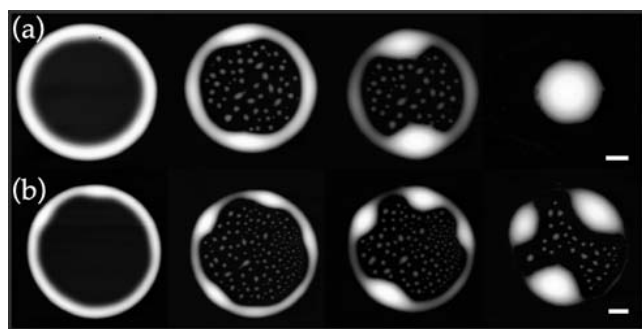


Fig. 2 Evolution of two PS toroidal sections as observed with AFM. The images were obtained by quenching the sample at various stages allowing the imaging to take place in the glassy state. The scale bars are $5\ \mu\text{m}$ wide; height scales are both approximately $160\ \text{nm}$ in (a) and (b); in the fourth column the height scales are $\sim 400\ \text{nm}$ for (a) and $\sim 230\ \text{nm}$ for (b).

Fig. 1(b). PS toroids can easily be made to undergo a transition from the solid to melt state and the approach to equilibrium can be recorded while the system is viewed under an optical microscope. The approach to equilibrium can be halted and any intermediate state can then be observed using AFM (see images in Fig. 2). As was the case for the macroscopic toroids of Pairam and Fernández-Neives,³ we find that the evolution of the nano-scale toroidal sections are influenced by the geometric constraints.

Experimental

To create the glassy polystyrene toroids, we place a bath of methanol onto a $1 \times 1\ \text{mm}^2$ Si substrate (University Wafer). The

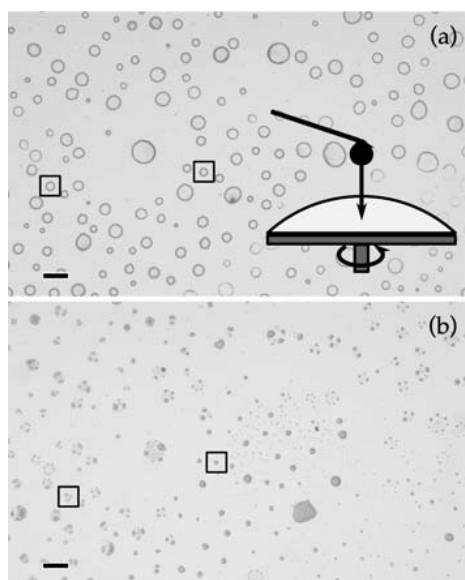


Fig. 3 The schematic illustrates the sample preparation: a small droplet of PS dissolved in toluene falls from a small syringe needle onto a substrate covered with methanol. Spincoating is immediately initiated and most of the three component solution is ejected from the substrate. After spincoating is completed, toroidal sections of PS are found on the substrate as shown in the optical microscopy image (a). The image in (b) is obtained after annealing the sample in a toluene saturated atmosphere for time periods of order two hours or less. The boxes indicate the two rings shown in the first and fourth columns of Fig. 2. The scale bars are $100\ \mu\text{m}$.

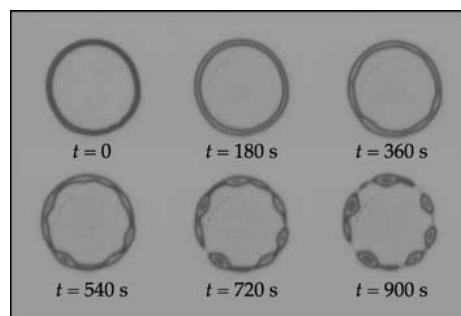


Fig. 4 The observed evolution of a PS torus in an atmosphere saturated with toluene. N , the number of wavelengths observed was counted at the onset of the P-R instability similar to the image shown at $t = 540\ \text{s}$.

substrate is on a stationary spincoater over which a syringe filled with PS dissolved in toluene is placed (see schematic in Fig. 3(a)). The PS (Polymer Source Inc.) has molecular weight $M_w = 221\ \text{kg/mol}$ and polydispersity index of 1.03. A small drop of the solution is allowed to fall into the methanol bath and spincoating ($\sim 4000\ \text{rpm}$) is immediately initiated as indicated schematically in Fig. 3(a). Toluene is a good solvent for PS and is miscible with methanol. Methanol is a non-solvent for PS. The spincoating process ejects most of the fluid and upon completion leaves behind a collection of toroidal sections with distributions of radii r , and cylinder widths w . Here we assume that the contact angle with the substrate is constant for all toroids and hence the cylinder radius $a \propto w$. Concentrations of 0.1 to 1 wt% PS have been observed to produce toroidal sections. A typical image of the resulting sample is shown in Fig. 3(a).

Once toroidal sections have been prepared, the samples are placed in a toluene saturated atmosphere.^{5,6} Since toluene is a good solvent for PS, the toroidal sections absorb toluene which causes them to transition from the glassy to the melt state. The geometry in which the toroids are prepared is unstable and the rings eventually dewet to form droplets which minimize the free energy of the system. Images are taken with a CCD camera at periodic intervals using optical microscopy. The end result of this process is shown in Fig. 3(b). In Fig. 4 a series of optical microscopy images illustrating the evolution of the instability for a single torus is shown. For several samples, the dewetting process has been paused at various stages by removing the toluene atmosphere and quenching into the glassy state. Once the evolution was halted, the samples were imaged with AFM (Veeco Caliber). The evolution could be commenced simply by re-immersing the sample in the toluene saturated atmosphere. Results of this process are shown in Fig. 2.

Results and discussion

Formation of toroids

There has been significant interest in the formation of ‘rings’ especially as a result of work done by Deegan and coworkers which was inspired by the formation of coffee stains.⁷ It was shown by these authors that the formation of a ring resulting from a drying drop of a colloidal suspension was in part the result of greater evaporation near the contact line. The enhancement of evaporation causes an outward flow

towards the edge of the droplet and subsequent ring formation due to aggregation of the colloids at the contact line. Similar results are obtained for the drying of a droplet of polymer solution.^{8–10} The concentration gradients in a drying droplet were recently visualized directly using fluorescence microscopy by Kajiya and coworkers for a polymer solution drying in air.⁸ In these systems large polymeric rings ($r \sim$ millimeters) were formed similar to the ones described in the study presented here. Poulard and Damman⁹ investigated the importance of the substrate properties and the various interfacial tensions to the formation of a ring at the edge of a drying droplet. In the system discussed here there is no droplet that is drying in air, though we propose a mechanism that borrows from what has been learned from such systems.^{7–9}

Although we cannot directly observe the formation of polymer toroids, we propose the following mechanism for their formation. As the PS and toluene solution enters the methanol reservoir, spin coating is immediately initiated. The spinning substrate accelerates and shears the three component mixture and produces tiny droplets of the PS solution in methanol, a fraction of which land on the Si substrate and make some contact angle with the surface. This initial step is highly complex and we cannot experimentally follow this process directly because of the rapid speed with which this occurs (fraction of a second). The size distribution of the tori, and even the presence of tori, is sensitive to the timing and spin speed. We find that the spinning must be initiated immediately as the droplet of PS and toluene solution hits the methanol. If the process takes too long, the PS precipitation has proceeded too far and a fine dispersion of PS particles is found on the substrate rather than tori. With careful timing of the process the results are reproducible with tori distributed randomly on the substrate and ring radii ranging from several micrometers to a few tens of micrometers. The second step proceeds once small droplets of PS in toluene surrounded by methanol contact the substrate. We suggest that the process by which the rings form is analogous to the outward flow responsible for ring formation in drying droplets of polymer solutions^{8–11} or colloidal dispersions.⁷ In our case the PS precipitates out of the toluene solutions as soon as the miscible methanol and toluene mix at the interface of the droplet. As in the case of a colloidal dispersion, the PS precipitate is driven towards the contact line both because of pinning at the substrate and the higher flux of toluene near the contact line.^{7–11} As shown by Poulard and Damman⁹ the Marangoni effect can drive flow at the interface especially for the case of droplets drying in air. Because the interface between the PS solution droplet and the methanol vanishes rapidly due to the miscibility of the two solvents, the flow driven by the osmotic pressure is dominant.⁷ We note that the enhanced flux at the contact line is the result of the boundary imposed by the substrate causing an anisotropy in the diffusion of toluene and methanol. The final result is a toroidal ring of polymer on a substrate with a very thin film of polymer inside the ring (see Fig. 1(b)).

In order to further substantiate the proposed mechanism for the formation of the toroids, we turn to simulations of the phase separation of a ternary mixture composed of methanol, toluene and PS. Methanol is known to be miscible with toluene but immiscible with PS, whereas toluene is miscible with PS. The

free energy of the ternary mixture can be described by the Flory-Huggins¹² theory supplemented with the de Gennes¹³ gradient contribution,

$$\Delta f = \phi_m \ln \phi_m + \phi_t \ln \phi_t + \frac{\phi_p \ln \phi_p}{N_p} + \chi_{m,p} \phi_m \phi_p + \chi_{m,t} \phi_m \phi_t + \chi_{t,p} \phi_t \phi_p + \sum_{i=m,t,p} \bar{\kappa}_{ii} (\nabla \phi_i)^2 \quad (1)$$

where ϕ_i is the local volume fraction of component i and is a function of position; $\chi_{i,j}$ is the Flory-Huggins interaction parameter between components i and j ; the subscripts m , t and p represent methanol, toluene and polystyrene respectively; and N_p is the degree of polymerization of the PS. The gradient energy coefficients, $\bar{\kappa}_{ii}$, are assumed to be constant for a system with constant overall concentrations, $\bar{\phi}_i$. For a given initial polymer concentration, which is in general not at equilibrium, the dynamics of the system can be described by the time-dependent Ginzburg-Landau (TDGL) theory.¹⁴

In our simulation boxes (ranging in size from $100 \times 100 \times 25$ to $400 \times 400 \times 100$), we start with a spherical cap that has a contact angle $\theta = \pi/6$. The cap is filled by a homogeneous ‘PS’ and ‘toluene’ mixture ($\phi_p = 0.0025$, $\phi_t = 1 - \phi_p$ and $\phi_m = 0$) with $\chi_{t,p} = 0.0$ and $N_p = 2000$. Outside the spherical cap, the box is filled with ‘methanol’ ($\phi_p = \phi_t = 0$ and $\phi_m = 1$). The interaction parameters are specified by $\chi_{m,t} = 0$ and $\chi_{m,p} = 8$.¹⁵ These parameters reflect the fact that, toluene and methanol are miscible, PS is miscible with toluene, and PS is immiscible with methanol. The boundary conditions are chosen to be reflective at the substrate. All the other boundaries are such that when a toluene molecule comes in contact with the wall it is replaced by methanol in order to simulate the infinite methanol bath. With this initial condition, the equations of motion defined using eqn (1) have been evolved in time. Fig. 5 shows the evolution of one such simulation, clearly demonstrating that the phase separation coupled with solvent mixing can produce polymer toroids. The simulation does not include the evaporation of the two solvents from the system and the eventual freezing of the polymer. We assume that during the final evaporation stage, the structure collapses onto the substrate and freezes leaving the tori resembling the integrated PS concentration shown in 5(b).

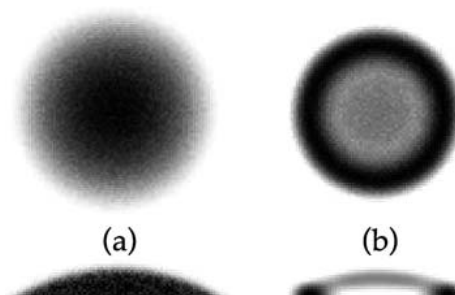


Fig. 5 The formation of a PS torus for a simulation box with dimensions $100 \times 100 \times 25$. The initial, homogeneous state of the spherical cap is shown in (a). Some time later a ring is formed, as shown in (b). The gray level is proportional to the integrated PS concentration from the top to the bottom of the simulation box (top row), or the radially integrated PS concentration (bottom row). White indicates no PS.

Instability

Having discussed the formation of the toroids, we now turn to the instability which occurs when a torus is free to flow (for a typical example see Fig. 4). When a toroidal section is exposed to a toluene saturated atmosphere, the PS, which is in the glassy state at room temperature in air, is plasticized by the toluene and is in the melt state. The PS becomes mobile and flow proceeds in the direction that decreases free energy the fastest. The P-R instability drives the toroidal section to break up into droplets. The number of droplets formed is determined by the wavelength of the instability. Using either linear stability analysis or Rayleigh's work principle, it can be shown that the 'most dangerous' (fastest growing) wavelength is proportional to the cylinder radius, a . It is this wavelength that we associate with the onset of the instability observed in our experiments.^{1,16} From an image as shown in Fig. 4 at $t = 540$ s it is possible to measure the number of wavelengths, N , that fit in the toroidal section. Since the width, w , of the toroidal section is proportional to the radius of the cylinder, a , we can write $N \sim r/w$.

As shown in Fig. 3, the method of producing the solid polymer toroids presented here yields sections with a variety of values of overall ring radii, r , and section widths, w . In Fig. 6(a), the line intensity profile of a toroidal section as observed in an optical microscopy image is shown. From line profiles such as these, one can measure values of r and w . In Fig. 6(b) a plot of the number of wavelengths that fit on the toroids, N , as a function of the measured ratio r/w is shown. The value of r/w is measured just prior to the observation of the P-R instability. As expected from the simple linear stability analysis,^{1,16} N is linear in r/w .

The preceding argument has assumed that the curvature of the overall ring radius, r , of the toroidal sections does not contribute to their evolution in the liquid state. However, a torus has two routes by which the free energy can be reduced: 1) the P-R instability, as discussed above; and 2) by evolving towards a ring with a smaller radius, r , while the width of the ring, w , increases to maintain a constant volume. For the latter route, letting $r_\epsilon = r - \epsilon$ and with volume conservation, it is easy to show that the ratio of the areas of the torus before and after a small change in r is, to first order in ϵ ,

$$\frac{\mathcal{A}_\epsilon}{\mathcal{A}} = 1 - \frac{\epsilon}{2r} \quad (2)$$

Note that this ratio is less than unity for all $\epsilon > 0$; therefore, a torus can reduce its surface area and hence its free energy by

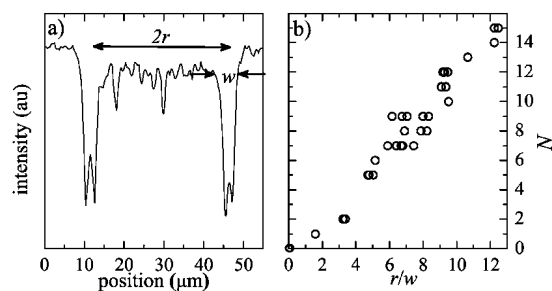


Fig. 6 (a) A line profile of a ring similar to the one shown in Fig. 4 at $t = 180$ s. From this line profile, r , and w , are easily obtained. (b) A plot of the number of wavelengths around a torus as a function of the ratio of the overall radius to the section width, r/w at similar stages of development. N is linear in r/w as expected from the P-R instability.

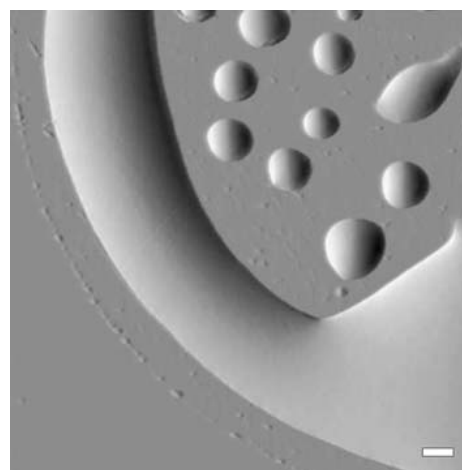


Fig. 7 AFM error signal of the ring shown in the third column of Fig. 2(a). About $1 \mu\text{m}$ from the three phase contact line of the main ring, a thin concentric halo is clearly visible which suggests that r is decreasing with time. The scale bar is $1 \mu\text{m}$.

decreasing r . Because volume is conserved, this decrease in r is accompanied by an increase in the width, w , of the torus on the substrate. The balance between these two mechanisms depends on which timescale dominates. If the curvature $1/r$ becomes comparable to the curvature that dominates the timescale of the P-R instability, $1/a$ (or $1/w$), then we would expect the ring radius to shrink during the experiment.

In Fig. 7, we show a detail of the AFM error signal (roughly, the derivative of the topography) of the ring shown in the third column of Fig. 2(a). Around the outer three phase contact line of the ring, there is a clearly visible remnant of the ring in its initial state. As expected in cases where the time scale of the P-R instability does not dominate, this example shows that the torus decreases its radius, r . Because of the observation that the ring radius can decrease prior to the onset of the P-R instability (Fig. 7) the values of r/w in Fig. 6 are obtained just prior to the onset of the P-R instability.

The effect of decreasing the free energy by reducing the ring radius is to decrease the ratio r/w as a function of time until the P-R instability dominates. In order to validate this second mechanism we followed the time evolution of the outer diameter of a ring using AFM during the onset of the instability. In Fig. 8

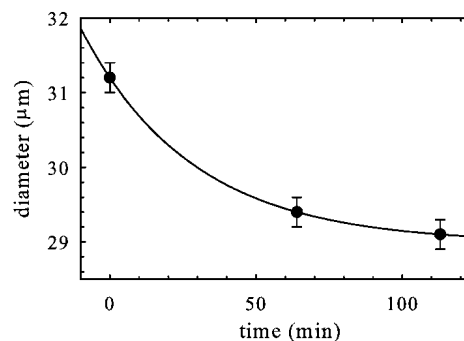


Fig. 8 A plot of the outside diameter of a torus as a function of annealing time during the evolution of the instability (solid line to guide the eye). The data in this plot corresponds to the first three AFM images shown in Fig. 2a).

the shrinking of the ring with time is clearly visible indicating that the two mechanisms, the P-R instability and decreasing ring radius, compete with the balance set by the curvatures given by $1/a$ and $1/r$ respectively.

Taking into account both the cylinder curvature which drives the P-R instability, $1/a$, and the curvature, $1/r$, which drives the ring radius to decrease, a complex interplay between these two mechanisms emerges. The maximally unstable wavelength for the P-R instability may not be commensurate with the torus, thus the free energy is reduced *via* a decrease in the ring radius. Eventually the torus becomes commensurate with a P-R wavelength which dominates the reduction of the surface area. While for simplicity we have discussed these mechanisms as two subsequent steps, in fact both mechanisms are competing with the P-R instability dominating in the last stage.

Conclusion

We have presented a novel method by which a collection of solid PS toroidal sections with micro- and nano-scale dimensions can be prepared on a substrate. The method requires a solution of the polymer in a good solvent to be dropped into a miscible bath of poor solvent for the polymer. Here the ternary system used was PS, toluene, and methanol. We provide evidence for a formation mechanism which is similar to the way in which coffee stains form or polymer solution droplets dry.⁷⁻¹¹ Experiments have been carried out in which the polymer toroids were allowed to evolve in the melt state. As would be the case for a linear jet, the P-R instability is responsible for their breakup. In contrast to the straight liquid jet we have shown that the additional curvature of the torus provides a second mechanism by which these structures can minimize their free energy – the ring radius can decrease. In

order for the P-R instability to grow the wavelengths of the instability must be commensurate with the circumference of each torus. In the cases where the fastest growing P-R wavelength for a torus does not drive the instability too quickly, the competing mechanism which acts to shrink the ring radius can be observed.

Acknowledgements

Financial support from NSERC of Canada is gratefully acknowledged.

References

- 1 J. Eggers, *Rev. Mod. Phys.*, 1997, **69**, 865.
- 2 J. Royer, D. Evans, L. Oyarte, Q. Guo, E. Kapit, M. Möbius, S. Waitukaitis and H. Jaeger, *Nature*, 2009, **459**, 1110.
- 3 E. Pairam and A. Fernández-Nieves, *Phys. Rev. Lett.*, 2009, **102**, 234501.
- 4 E. Villermaux and B. Bossa, *Nat. Phys.*, 2009, **5**, 697.
- 5 L. Xu, T. Shi, P. Dutta and L. An, *J. Chem. Phys.*, 2007, **127**, 144704.
- 6 S. Lee, P. Yoo, S. Kwon and H. Lee, *J. Chem. Phys.*, 2004, **121**, 4346.
- 7 R. Deegan, O. Bakajin, T. Dupont, G. Huber, S. Nagel and T. Witten, *Nature*, 1997, **389**, 827.
- 8 T. Kajiyi, D. Kaneko and M. Doi, *Langmuir*, 2008, **24**, 12369.
- 9 C. Poulard and P. Damman, *Europhys. Lett.*, 2007, **80**, 64001.
- 10 H. Hu and R. G. Larson, *Langmuir*, 2005, **21**, 3963.
- 11 F.-I. Li, P. H. Leo and J. A. Barnard, *J. Phys. Chem. B*, 2008, **112**, 16497.
- 12 M. Rubinstein and R. Colby, *Polymer Physics*, Oxford University Press, 2003.
- 13 P. de Gennes, *J. Chem. Phys.*, 1980, **72**, 4756.
- 14 C. Huang, M. de La Cruz and B. Swift, *Macromolecules*, 1995, **28**, 7996.
- 15 N. Schuldt and B. Wolf, *Polymer Handbook*, John Wiley & Sons, Inc., 1999, vol. 4, (ch. VII), p. 247.
- 16 L. E. Johns and R. Narayanan, *Interfacial Instability*, Springer, 2002.

Manuscript iv

Dynamics of interacting edge defects in copolymer lamellae

J.D. McGraw, I.D.W. Rowe, M.W. Matsen, and K. Dalnoki-Veress, *European Physical Journal E*, **34**, 131 (2011).

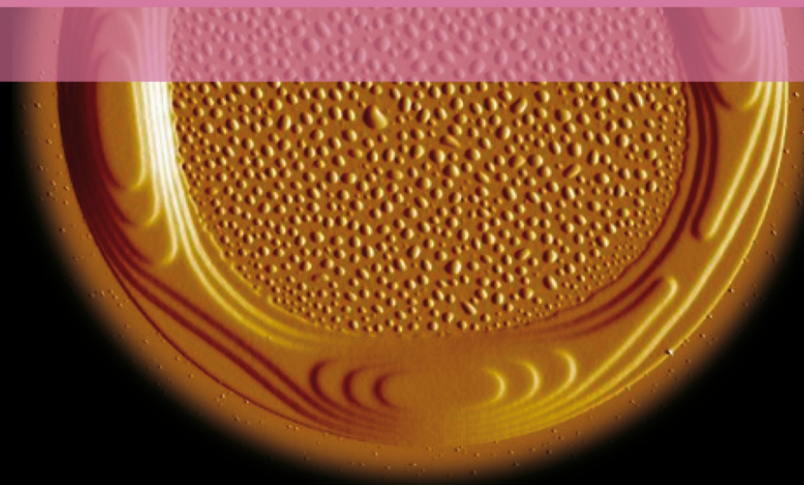
EPJ E

FOUNDED BY PIERRE-GILLES DE GENNES

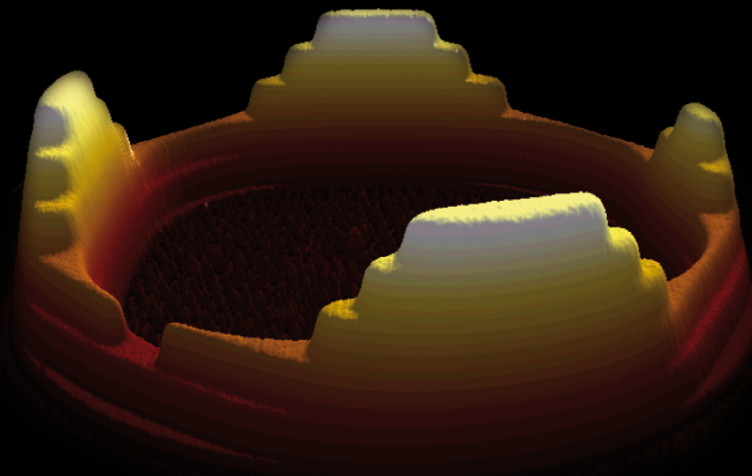


Recognized by European Physical Society

Soft Matter and Biological Physics



From: Dynamics of interacting edge defects
in copolymer lamellae
by J.D. McGraw et al.



Dynamics of interacting edge defects in copolymer lamellae

J.D. McGraw¹, I.D.W. Rowe¹, M.W. Matsen², and K. Dalnoki-Veress^{1,a}

¹ Department of Physics & Astronomy and the Brockhouse Institute for Materials Research, McMaster University, Hamilton, ON, Canada

² School of Mathematical and Physical Sciences, University of Reading, Whiteknights, Reading, UK

Received 16 August 2011

Published online: 21 December 2011 – © EDP Sciences / Società Italiana di Fisica / Springer-Verlag 2011

Abstract. It is known that terraces at the air-polymer interface of lamella-forming diblock copolymers do not make discontinuous jumps in height. Despite the underlying discretized structure, the height profiles are smoothly varying. The width of a transition region of a terrace edge in isolation is typically several hundreds of nanometres, resulting from a balance between surface tension, chain stretching penalties, and the enthalpy of mixing. What is less well known in these systems is what happens when two transition regions interact with one another. In this study, we investigate the dynamics of the interactions between copolymer lamellar edges. We find that the data can be well described by a model that assumes a repulsion between adjacent edges. While the model is simplistic, and does not include molecular level details, its agreement with the data suggests that some of the underlying assumptions provide insight into the complex interplay between defects.

1 Introduction

Diblock copolymers are formed when two chemically distinct polymer chains, “*A*” and “*B*”, are covalently bonded together. Self-assembly of these molecules into compositionally periodic structures occurs when different species of the molecules have a sufficiently unfavourable interaction energy [1]. For the simplest case in which the molecules’ *A* and *B* blocks are roughly the same size, a lamellar morphology is observed. Within the lamellae of a well-ordered system, the periodic change in the concentration of a given chemical species depends on the size of the molecule. The repeat period has a well-defined value, H_o , and each lamella consists of a bilayer of molecules: $A - B/B - A$. The characteristic lengthscale of the morphology given by H_o is the result of a balance between an enthalpic repulsion of the *A* and *B* blocks, and the entropy which favours a random coil configuration. The repeat period of the bilayers is on the order of the radius of gyration of the molecule (~ 10 nm) and is controlled by the product χN ; where N is the number of monomers in the polymer chain and χ is the Flory-Huggins parameter which defines the chemical incompatibility of the *A* and *B* segments [2]. Similarly, the degree of ordering is also determined by χN . Values of χN much greater than 10 lead to strong segregation of the blocks, with the *A*–*B* junction points of the diblocks confined to nearly two-dimensional planes. χ is a decreasing function of the temperature since the degree of order must also decrease with temperature. When χN

decreases, the junctions make increasingly greater excursions from their strongly confined two-dimensional planes until finally all order is lost in passing through the order disorder transition (ODT). More exotic morphologies can be observed when the lengths of the two blocks differ, thereby encouraging curvature at the interfaces [1, 3].

Diblock copolymers serve as model systems for studying self-assembly, with promise for data storage [4, 5], adhesion [6], and photonics applications [7], among others [7]. The phase behaviour and morphology of these systems in the bulk is well established both theoretically and experimentally [1, 8–12]. However, when confinement dimensions approach those of the micro-phase separation, novel structures emerge. In such cases, the molecules pay an energy penalty in conforming to the geometry of confinement. Furthermore, it is typical for there to be a preference for either the *A* or *B* block to contact the confining interface. The preferential interaction can provide further frustration from the ideal bulk morphology and even induce order at temperatures above the bulk ODT [13–17]. Confinement of a diblock copolymer by a non-deformable interface has been termed *hard confinement*. Such systems have received much attention, resulting in a rich variety of phases that have been predicted and observed for systems under planar, cylindrical and spherical confinement [7, 18–23].

Soft confinement of diblock copolymer systems, where the confining interface itself may deform as a result of the underlying diblock morphology, reveals an additional complexity to the interplay between the optimal bulk mor-

^a e-mail: dalnoki@mcmaster.ca

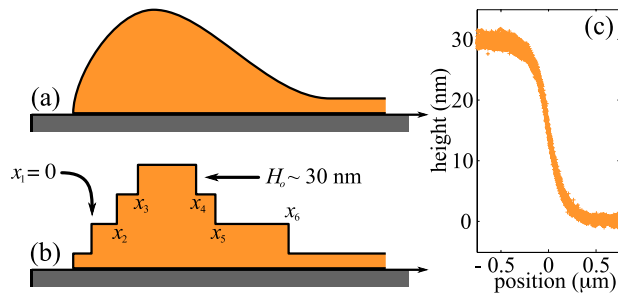


Fig. 1. Schematic cross-section of a) an as-prepared ring, and b) its condition upon annealing for a short period of time. The positions, x_i , of lamellar edges for a stack with 3 bilayers ($n = 6$) are also shown schematically; in this study, $x_n - x_1 \sim 7 \mu\text{m}$ is typical. c) AFM topography line profiles of isolated edges.

phology and the interface. Perhaps the simplest example of soft confinement is provided by the free interface of a thin symmetric diblock film supported on a substrate. In such a case the hard confinement of the substrate will typically show a preference for one of the blocks which orients the lamellae parallel to the substrate. However, the soft free interface is able to deform to minimize the free energy of the system which has a profound effect on the morphology of the air-polymer interface [24, 25]. For the case of a lamellae-forming diblock, the ability of the free surface to accommodate the layers can result in a terraced height profile, with steps in the height of the film that correspond to a molecular bilayer with height H_o .

To understand the formation of terraces on the free surface, take for example a diblock film with thickness h under *symmetric wetting* conditions (the substrate and free interface favour the same block). In the ordered state, the ideal thickness at any point in the film is commensurate with an integer number of bilayers, $h = kH_o$, where k is an integer. That is, a continuously varying topography will develop into a terraced free surface upon ordering. The transition from continuously varying topography to a terraced height profile is shown in figs. 1a) and b) for the *asymmetric wetting* case. For asymmetric wetting, the substrate and free surface favour the opposite species. In this case there exists an additional diblock *monolayer* at the substrate to satisfy the wetting condition of A at one interface and B at the other [25]. Asymmetric wetting is observed in the work discussed here and illustrated by the nearest-to-substrate monolayer shown in fig. 1b).

Away from the transition region where the topography changes by one lamellar step, the preferred lamellar spacing, H_o , is the result of an interplay between the chain stretching and interfacial energies [2]. However, in the transition from one terrace to the next, a discrete step function results in a significant cost to the free energy because of the excess surface area. Instead the transition region is broadened by the Laplace pressure. Thus, a larger surface tension will result in a broader transition. The detailed shape and morphology of the transition between terraces has been studied by several groups in the past decades [26–29]. It has been found that the transition re-

gion can induce a number of different morphologies depending on the polymer and substrate combination as the underlying equilibrium morphology is frustrated by the non-ideal confinement of the interface. The internal structure can be a dislocation [26, 27], lamellae oriented perpendicular to the interface [28], and cylindrical domains [29]. The morphology of asymmetric diblock copolymer liquids which favour morphologies more complex than lamellae can also be affected by the thickness gradient in the transition region [30].

In fig. 1c) is shown an atomic force microscopy (AFM) measurement of the topography of several lamellar transition regions in a poly(styrene-methyl methacrylate) (PS-PMMA) thin film. While the experimental details are described below, it is immediately clear that the edge is not discontinuous, but is smoothly varying. The resulting topography is an edge defect with a cost to the free energy of the system that is minimised by an interplay between the interfacial and stretching energies as discussed above. Recent studies by Croll and coworkers [31] and Kim and Matsen [32] have investigated the detailed shape of symmetric diblock copolymer droplets in the ordered state. It was found that when the distance between two edges becomes small, there is an interaction between the defects. In the work by Croll and coworkers, AFM images revealed that the droplets self-assemble into a nearly conical shape of terraced disks reminiscent of Mayan temples. The shape of the droplets was understood in terms of a model which included a repulsive interaction between the edges.

Qualitatively, the origin of the repulsive interaction is easily understood. As two edges, each with an equilibrium height profile similar to that shown in fig. 1c) approach each other, their shapes must change from ideal which results in an energy penalty. In [31] an empirical, exponentially decaying, repulsive interaction was found to give good agreement with the experiments; however, the agreement was not sensitive to the exact functional form of the interaction. Furthermore, while the morphologies of diblock droplets were remarkable, the cylindrically symmetric geometry results in a complexity not related to the edge interaction alone. Specifically, the disks which make up the droplet have curvature, resulting in an *edge tension* contribution to the free energy that scales linearly with the radius of the disk. The equilibrium nature of the study and dependence on edge tension resulted in an inherent insensitivity to the functional form of the defect interaction [31].

With a view towards gaining a more general understanding of the interaction between topological defects we focus here on the dynamics of the interplay between the transition region in a simplified geometry. We have recently learned to prepare polymer tori on a substrate [33]. These structures form much like a nanoscale version of a rim left behind by an evaporating droplet, *e.g.* the stain left behind by a coffee spill [34–36]. These rings are not perfect tori: upon preparation the cross-section of the ring is asymmetric and also forms a very thin layer interior to the ring as shown by the schematic in fig. 1 [33]. If the rings are prepared so that they are thin but have a large

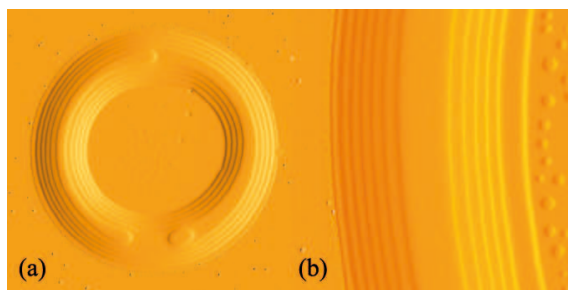


Fig. 2. a) AFM tapping amplitude of a copolymer ring that has been annealed at 180 °C for 2 hr; the image is 20 μm wide. b) A close up of another ring, a 10 μm scan.

radius so that the in-plane curvature is small, then we will show that it is possible to ignore the contribution of the edge tension to the change in free energy. Neglecting the edge tension simplifies the system significantly.

These samples provide an ideal geometry for the study of the edge interactions for two reasons. First, we can treat the system as 2-D with no change in the free energy due to edge tension. Second, once the terraces develop (see fig. 1b)), the only interaction that drives changes in the morphology is the interaction between edges. In equilibrium all layers must be centred such that the stack is symmetric about the midpoint of the rim (*e.g.*, in fig. 1b), this corresponds to $(x_1 + x_6) = (x_2 + x_5) = (x_3 + x_4)$). By studying the evolution from the initial asymmetric edge distribution towards a symmetric one, it is possible to investigate the form of the repulsive interaction between edges.

2 Experiment

The ring samples were prepared using the method as described previously [33]. Briefly, a droplet of methanol covers the surface of a $1 \times 1 \text{ cm}^2$ Si wafer (University Wafer). A small syringe ($\sim 0.5 \text{ mm}$ diameter) filled with polymer dissolved in toluene is suspended just above the methanol bath. A small droplet of the polymer solution is allowed to fall into the methanol bath and spin coating at approximately 4000 rpm is immediately initiated. Here the polymer is soluble in toluene, and toluene is miscible with methanol. However, the polymer is not soluble in methanol. As the droplet of polymer solution falls into the methanol bath, the rapid shearing during spincoating breaks the drop into many tiny droplets, some of which land on the substrate. Toluene within these droplets exchanges with the methanol causing the diblock to precipitate and form rings [33]. With appropriate timing it is possible to find polymer ring sections scattered randomly over the substrate. Typical dimensions for the rings are approximately 200 nm in height, 50 μm in diameter and 5 μm wide, making them ideally suited for study by AFM (Veeco Caliber). In contrast with our previous work on the evolution of homopolymer rings [33], here a symmetric diblock copolymer, PS-PMMA, was used (Polymer

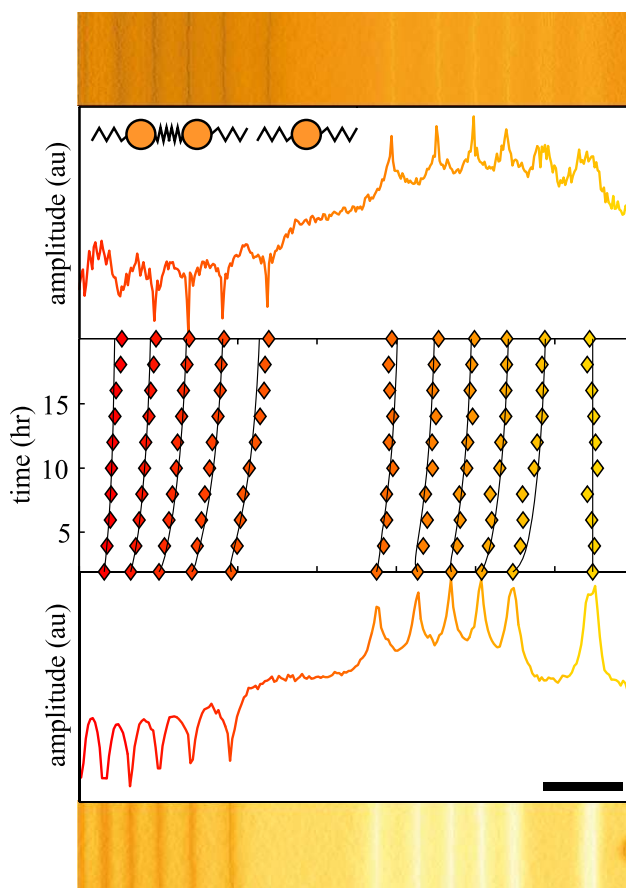


Fig. 3. From the bottom up: a portion of an AFM image as in fig. 2b) for $t = 2 \text{ hr}$ of annealing; its vertically averaged line profile; data points for the extrema which correspond to the lamellar edges from AFM scans after cumulative annealing times; the top two panels are analogous to the bottom two, except they are for data taken after $t = 20 \text{ hr}$ of annealing. The scale bar and separations between adjacent tick marks on the horizontal scale in the central portion are 1 μm wide. All portions of the figure have the same horizontal scale. The “spring-and-bead” schematic represents the mechanical system discussed in the text with the potential given by eq. (4).

Source Inc. Dorval, Canada). The total molecular weight was 46 kg/mol, with a polydispersity index of 1.05. Solutions of toluene and PS-PMMA were prepared with a polymer mass fraction of approximately 0.5%.

The ring samples supported on the Si substrate were placed on a heating stage (Linkam Scientific) and annealed at 180 °C for two-hour periods in ambient conditions. Prior to the first annealing step, polymers are in the disordered state and the rings are topographically indistinguishable from those of a homopolymer ring, as shown schematically in fig. 1a). After the first two-hour annealing step, the polymer chains phase separated into fully developed lamellar structures. The terrace edges were easily identified with the AFM tapping amplitude signal, as shown in figs. 2 and 3 (the AFM tapping amplitude or

error signal can be interpreted as roughly the gradient of the topography). The subsequent annealing steps allow us to gather time-dependent edge positions, $x_i(t)$ as defined in fig. 1a). The edge positions were determined by finding the extrema in the tapping amplitude line profiles (fig. 3).

To obtain the data presented in fig. 1c) of an isolated terrace edge, a thin film of PS-PMMA was spincoated onto a $1 \times 1 \text{ cm}^2$ Si wafer. The resulting film, prepared such that it was incommensurate with the lamellar spacing of the diblock, resulted in a surface perforated with holes upon annealing at 180°C for several hours. The holes were of various lateral sizes and had a constant depth corresponding to the height of a single bilayer, $H_o \sim 30 \text{ nm}$. AFM in tapping mode was used to obtain topography data of holes with radii ranging from $2 \mu\text{m}$ to $7 \mu\text{m}$ (note that this is larger than the transition region between two lamellar terraces). Furthermore, all line profiles were taken perpendicular to the transition between the two lamellar terraces present at the air-polymer interface. Transition profiles, irrespective of the diameter of the holes studied, were identical and are shown in fig. 1c). The perturbation due to the transition from one terrace to the next ranges approximately $0.5 \mu\text{m}$, which compares favourably with results of previous workers [26, 28, 29].

3 Experimental results

The perturbation induced by an edge results in a cost to the free energy as two edges approach one another [31]. Starting from the asymmetric distribution of the edges, the equilibrium configuration should result in a symmetric topography. In the central panel of fig. 3 the position of each edge is shown as a function of increasing time as the topography evolves. As expected, the last measurement at 20 hours of annealing is symmetric, with intermediate times providing the evolution of the edges. The ring observed contained $n = 12$ edges (six bilayer lamellae). In addition to the twelve bilayer edges, there is one edge in contact with the substrate. This edge corresponds to the monolayer carpet of molecules which forms because of the asymmetric wetting conditions of our experimental system (see fig. 1b)). During the course of the experiment, there is no observable change to this monolayer. Just as in earlier work on droplets [31], the monolayer position does not measurably affect the remaining lamellae in the stack. Thus, here we focus only on the stack of lamellae on top of the monolayer. The positions of the edges as shown in fig. 3 are always measured with respect to the bilayer edge furthest from the centre of the ring, *i.e.* $x_1 = 0$ as shown in fig. 1b).

Measurements of lamellar edge dynamics as shown in fig. 3 were made for multiple rings. The rings studied had five, six and seven bilayers, all with slightly different initial conditions. Due to the fabrication procedure, the ring profile always has a steep side facing the substrate and a shallower side facing the central portion of the ring, and the initial edge configurations are always similar to that shown schematically in fig. 1b). For all the rings studied,

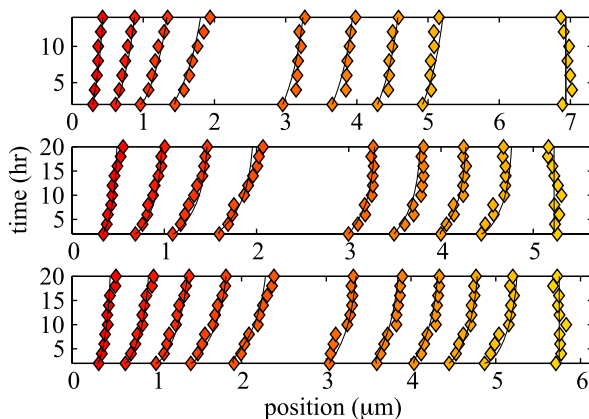


Fig. 4. Three plots of edge position as a function of annealing time for different rings. The black lines are best fits of the model described by eqs. (2), (3) and (4) to the experimental data.

the data is qualitatively similar to that shown in fig. 3. To demonstrate this consistency, three additional edge trajectories from distinct rings with five or six bilayers are shown in fig. 4.

4 Model

Figure 3 demonstrates that the configuration of lamellar edges is not static in time. Rather, there is an interplay of forces which causes them to move toward a state of lower free energy. To describe the evolution of these trajectories quantitatively, we resort to a simplified classical picture. We stress that in this tentative model we have not attempted to rigorously derive a molecular level description, as that currently eludes us. However, given the existence of an unfavourable repulsive interaction between edges, it is possible to elucidate the form of that interaction.

The model can be understood in its simplest terms from the following ingredients: 1) As is clear from fig. 2, there is little curvature of the edges in the lateral direction. Thus, the edge tension does not significantly contribute to changes in the free energy. 2) We assume that volume is conserved within the region that we are investigating. The validity of this is easily verified experimentally as discussed below. 3) While the molecular details are complex, we can think of the edges as being acted upon by a repulsive force. The edges move, while conserving volume, so as to minimise the total interaction. 4) The system is highly dissipative because of the viscous environment. While complex molecular mechanisms are at play, we model the dissipation in the simplest possible way: the velocity with which the edges move is proportional to the force acting upon them.

Before the details of the model are developed further, we provide a few more comments about the link between the simple classical model, and the real molecular system. Clearly, it is not the case that the edges represent

a rigid interface upon which a force acts, akin to pistons responding to a force in a viscous fluid. The molecules within each lamella exchange with neighbouring lamellae in response to a pressure or difference in potential. This exchange conserves volume, is dissipative, acts to minimize the free energy of the entire system, and should be taken as analogous to the simpler mechanical model we discuss here. It is the hope that a future detailed theoretical model, including the cost of the defects, can provide a more rigorous treatment.

In the simple classical picture, the energy of two adjacent lamellar edges is a function of the distance between them. For a given lamellar stack, as shown schematically in fig. 1, the total free energy is the sum of contributions from all pairs of edges,

$$\mathcal{F}(\{x_i\}) = F_o \sum_{i=1}^{n-1} g(w_i), \quad (1)$$

where $w_i = x_{i+1} - x_i$ is the distance between edges, F_o is a constant which sets the energy scale and n is the number of lamellar edges in the stack of $n/2$ bilayers. $g(w)$ is the function that describes how the free energy of two lamellar edges changes when they approach one another; only nearest neighbour edge interactions are taken into account. In principle the interaction between the edges that represent the top layer might have an interaction that differs from $g(w)$. For simplicity we have assumed this interaction to be of the same form.

The dissipation is included with an energy term of the form $\dot{W}_i = -\zeta \dot{x}_i^2/2$ [37], where ζ is a constant and the dot denotes differentiation with respect to time. As stated above, we limit ourselves to systems where the volume is conserved. In fact, material flows tangentially along the rings, changing the volume within the cross-section of the ring studied. A clear example of significant tangential flow is shown in fig. 5. However the flow on this larger length scale occurs on a longer time scale than that for which we apply the model. Conservation of volume is equivalent to stating that the sum of the lamellar widths is constant. That is, $\mathcal{L} = \sum_{i=1}^{n/2} (x_{n-i+1} - x_i)$ remains constant. Multiplying \mathcal{L} by H_o gives the area of the stack, and so $\mathcal{L}H_o$ can be seen as the differential volume element of the ring. Strictly speaking, the edge perturbs the thickness of the lamellae near the edge (see fig. 1c) which accounts for the flow around the circumference of the ring which breaks up into individual droplets (fig. 5). The morphology is reminiscent of the Plateau-Rayleigh instability observed in our previous work on homopolymer rings [33], although the mechanism for the development of the morphology in the symmetric diblock case is much more complex. Barnard and co-workers have observed similar layered structures prepared with dendrimers [35, 36].

The system under consideration is highly viscous and we assume that inertial effects play a negligible role in the evolution of the lamellar stacks. With this assumption and using eq. (1) along with the constant volume constraint, the Euler-Lagrange equations predict the classical trajec-

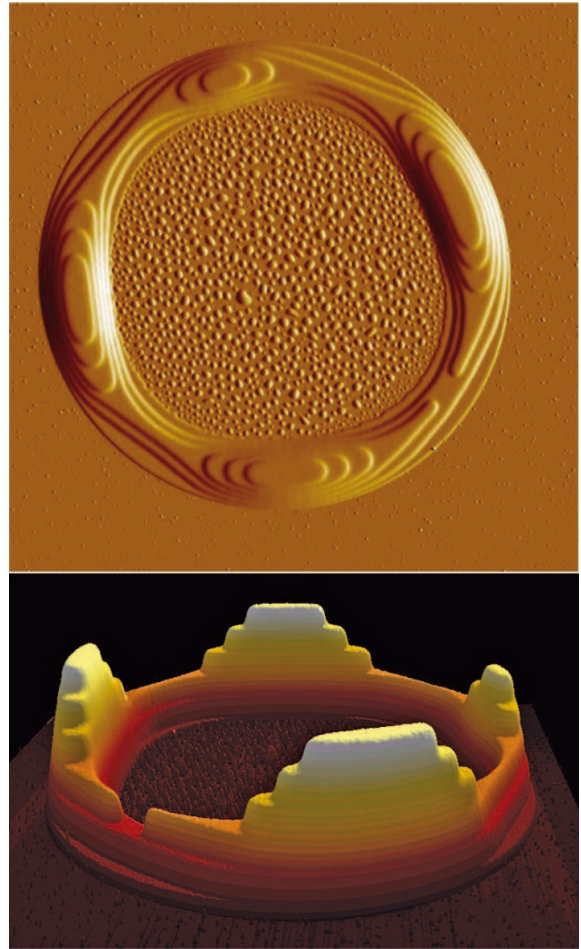


Fig. 5. AFM tapping amplitude (top) and topography (bottom) signal of a diblock ring in the late stages of annealing. A Plateau-Rayleigh-like instability has developed and the ring is showing the formation of four distinct droplets. The scan area is approximately $54 \times 54 \mu\text{m}^2$.

tories of lamellar edges:

$$\frac{Q\dot{x}_i}{w_o^2} = g'(w_{i-1}) - g'(w_i) \pm \tau, \quad (2)$$

$$\tau = \frac{1}{n-2} [g'(w_1) + g'(w_{n-1}) - 2g'(w_{n/2})]. \quad (3)$$

Here, $Q = w_o^2\zeta/F_o$ is the time scale of the system, w_o sets the range of the interaction. Furthermore, τ is the Lagrange multiplier introduced by the constraint of constant volume. The first two terms result from the condition $\dot{x}_1 = \dot{x}_n = 0$ which we impose based on our experimental data. The Lagrange multiplier represents the difference in net forces acting on the left- and right-hand sides of the lamellar stack.

To compare the model to experimental data, we need to choose the potential, $g(w_i)$, in eq. (1). As demonstrated in [31] and [32], the approach of two lamellar edges forces chains to deviate from their preferred lamellar structures

and must cause a rise in the free energy. The potential, $g(w_i)$, describes that interaction. We assume that the potential is a monotonically decreasing function of the distance between the lamellae. In [31], an exponential form was assumed for analytical convenience, however that experiment was sensitive to the strength but not the form of the interaction. We have found that an exponential form does not describe the evolution of the edges acceptably. Here we propose a simple potential that gives rise to a distance-dependent repulsion: a truncated quadratic potential of the form

$$g(w_i) = \begin{cases} \left(1 - \frac{|w_i|}{w_o}\right)^2, & \text{if } |w_i| \leq w_o, \\ 0, & \text{otherwise.} \end{cases} \quad (4)$$

This functional form is appealing as it is a purely repulsive Hookean potential which smoothly drops to zero when the distance between edges increases to $|w_i| = w_o$ (as depicted by the bead-and-spring schematic in fig. 3). With an initial condition supplied to eq. (2), it is possible to compute edge trajectories using the potential described in eq. (4). The trajectories were computed for various values of w_o and Q , using a fourth-order Runge-Kutta algorithm.

5 Discussion

As seen in figs. 3 and 4, the model provides a good fit to the experimental data with $w_o = 0.49 \pm 0.02 \mu\text{m}$ and $Q = 0.5 \pm 0.2 \text{ hr}$. We note that the fits are strongly dependent on the length scale, but less sensitive to the time scale. The uncertainties reflect the statistical distribution of the best fitting parameters of our nine measured edge trajectories (four of which are shown in figs. 3 and 4). In selecting rings to analyze, we have discarded any data that do not satisfy the constant volume constraint described in sect. 4. Thus, whenever the net circumferential flux of molecules at the point of measurements becomes non-zero, we cease consideration of the data set. For this reason the time scales in fig. 4 are not all the same.

Having demonstrated that the model is consistent with the data, we now discuss some implications and limitations of the analysis and experiment. The results presented provide further credence to the idea that the edges of diblock copolymer terraces *repel* one another. Furthermore, the data is sensitive to the chosen potential. While we have tried to model the data using an exponential potential (as in [31]) it was not possible to obtain acceptable fits for all data sets. Additionally, even only considering data sets for which acceptable fits were possible using the exponential potential, the fit parameters were not consistent with one another. In contrast, the Hookean form of the repulsion provided satisfactory fits to multiple rings with a range of initial conditions while the *two* fitting parameters were consistent for each case.

As discussed, the quadratic potential does not capture the complete picture: 1) While the Hookean model is appealing for its simplicity and consistent with experimental

results, we cannot exclude the possibility of other forms of the interaction which may also provide satisfactory results. 2) We have not considered molecular level details, but have instead attempted to give a minimal description which captures the essence of the problem. The potential described by eq. (4) is purely repulsive for edge separations less than w_o . One can compare the value of w_o as determined from best fits of the dynamical edge trajectories, $w_o \sim 0.5 \mu\text{m}$, to the profile width of isolated edges as shown in fig. 1c). From the figure it is clear that the lengthscale over which the presence of an isolated edge relaxes away is similar to w_o . Clearly a repulsive interaction cannot exist until these perturbed regions between two edges overlap. To put it another way, it is the profile width of isolated edges in equilibrium that controls the dynamic response of interacting lamellar edges. This comparison gives a consistency which provides further support for the proposed model.

The time scale is set by the parameter $Q = w_o^2 \zeta / F_o$. Thus, having obtained the best fit values for the distance and time scales, we can determine the ratio of the driving force and the dissipation. That is, $F_o / \zeta = w_o^2 / Q \approx 10^{-12} \text{ cm}^2/\text{s}$. While dimensionally like a diffusion constant, the process we have investigated in this study is driven, so care must be taken in direct comparisons to diffusion of diblocks. The dynamics of diblock copolymers have been discussed by many authors in the past and diffusion coefficients for a variety of diblock copolymers span a broad range of values including $10^{-12} \text{ cm}^2/\text{s}$ [38–40].

6 Conclusion

Understanding topological defects, and the interplay between them, underpins the control of morphologies. Here we have used the simplest form of soft confinement, that is, the confinement induced by a free interface, to investigate the interaction between steps in lamellae formed by a symmetric diblock copolymer. The underlying bilayer structure responds to a continuously varying topography by forming terraces—steps which correspond to the height of one bilayer. If the variation in the height is steep enough, then the terrace edges form close to one another, and the edge defects interact via a long-range repulsion. While the molecular details remain elusive, the source of the repulsion is intuitive: an edge is a defect which perturbs the surface profile with an associated cost to the surface energy. As two isolated edges approach, the perturbation deviates further, thereby deforming the equilibrium edge structure and increasing the free energy. We have performed measurements of the dynamics of interacting edges in structures with an asymmetric topography which, for all practical purposes, varies only in one dimension. These structures are nanoscale rims that form on a substrate much like the rim left by a coffee stain [33–36]. The asymmetric shape of the rim's cross-section, steep towards the outside of the ring and shallow towards the middle, ensures that the steps associated with the terraces have various distances between them. However, when only

the repulsive interaction of the edges is present the equilibrium morphology must be symmetric. By monitoring the evolution towards that symmetric structure one can elucidate the nature of the repulsive interaction using a simple classical model: in a dissipative system, the rate of change in the position of an edge is proportional to the force acting upon it, which in turn is dependent on the gradient of the repulsive potential. Here we have found that a Hookean repulsion between the edges is in good agreement with the data. While we cannot exclude the existence of other equally successful repulsive interactions, the best fit parameters provide additional evidence for a Hookean form. Specifically, the width over which the interaction acts is of the same length scale as the equilibrium perturbation of an interface by an isolated lamellar edge.

The authors thank Professor A.-C. Shi for valuable discussions. Financial support from NSERC of Canada is gratefully acknowledged.

References

- M.W. Matsen, J. Phys.: Condens. Matter **14**, R21 (2002).
- G. Strobl, *The Physics of Polymers: Concepts for Understanding their Structures and Behaviour*, 3rd edn. (Springer, 2007).
- A.K. Khandpur, S. Förster, F.S. Bates, I.W. Hamley, A.J. Ryan, W. Bras, K. Almdal, K. Mortensen, *Macromolecules* **28**, 8796 (1995).
- T. Thurn-Albrecht, J. Schotter, G.A. Kästle, N. Emley, T. Schibauchi, L. Krusen-Ebaum, K. Guarini, K.T. Black, M.T. Tuominen, T.P. Russell, *Science* **290**, 2126 (2000).
- C. Tang, E.M. Lennon, G.H. Fredrickson, E.J. Kramer, C.J. Hawker, *Science* **322**, 429 (2009).
- C. Creton, E.J. Kramer, H.R. Brown, C.Y. Hui, *Adv. Polym. Sci.* **156**, 53 (2002).
- I.W. Hamley, *Progr. Polym. Sci.* **34**, 1161 (2009).
- E. Helfand, *J. Chem. Phys.* **62**, 999 (1975).
- F.S. Bates, *Science* **251**, 898 (1991).
- M.W. Matsen, F.S. Bates, *Macromolecules* **29**, 1091 (1996).
- D.S. Herman, D.J. Kinning, E.L. Thomas, L.J. Fetters, *Macromolecules* **20**, 2940 (1987).
- H. Hirokazu, H. Tanaka, K. Yamasaki, T. Hashimoto, *Macromolecules* **20**, 1651 (1987).
- G.H. Fredrickson, *Macromolecules* **20**, 2535 (1987).
- M. Foster, M. Sikka, N. Singh, F. Bates, S. Satija, C. Majkrzak, *J. Chem. Phys.* **96**, 8605 (1992).
- A. Menelle, T. Russell, S. Anastasiadis, S. Satija, C. Majkrzak, *Phys. Rev. Lett.* **68**, 67 (1992) ISSN 1079-7114.
- K. Shull, *Macromolecules* **25**, 2122 (1992) ISSN 0024-9297.
- H. Tan, D. Yan, A. Shi, *Macromolecules* **37**, 9646 (2004).
- P. Lambooy, T.P. Russell, G.J. Kellogg, A.M. Mayes, P.D. Gallagher, S.K. Satija, *Phys. Rev. Lett.* **72**, 2899 (1994).
- W. Li, R.A. Wickham, R.A. Garbary, *Macromolecules* **39**, 806 (2006).
- B. Yu, P. Sun, T. Chen, Q. Jin, D. Ding, B. Li, A.C. Shi, *Phys. Rev. Lett.* **96**, 138306 (2006).
- P. Chen, H. Liang, A.C. Shi, *Macromolecules* **41**, 8938 (2008).
- P. Dobriyal, H. Xiang, M. Kazuyuki, J.T. Chen, H. Jinnai, T.P. Russell, *Macromolecules* **42**, 9082 (2009).
- M. Ma, E.L. Thomas, G.C. Rutledge, B. Yu, B. Li, Q. Jin, D. Ding, A.C. Shi, *Macromolecules* **43**, 3061 (2010).
- B. Collin, D. Chatenay, G. Coulon, D. Auserre, Y. Gallot, *Macromolecules* **25**, 1621 (1992).
- P. Green, R. Limary, *Adv. Colloid Interface Sci.* **94**, 53 (2001).
- M. Maaloum, D. Auserre, D. Chatenay, G. Goulon, Y. Gallot, *Phys. Rev. Lett.* **68**, 1575 (1992).
- K. Niihara, U. Matsuwaki, N. Torikai, K. Satoh, M. Kamigaito, H. Jinnai, *Polym. J.* **39**, 1105 (2007).
- B.L. Carvalho, E.L. Thomas, *Phys. Rev. Lett.* **73**, 3321 (1994).
- Y. Liu, M.H. Rafailovich, J. Sokolov, S.A. Schwarz, S. Bahal, *Macromolecules* **29**, 899 (1996).
- A. Horvat, A. Knoll, G. Krausch, L. Tsarkova, K.S. Lyakhova, G.J.A. Sevink, A.V. Zvelindovsky, R. Magerle, *Macromolecules* **40**, 6930 (2007).
- A.B. Croll, M.V. Massa, M.W. Matsen, K. Dalnoki-Veress, *Phys. Rev. Lett.* **97**, 204502 (2006).
- J.U. Kim, M.W. Matsen, *Soft Matter* **5**, 2889 (2009).
- J.D. McGraw, J. Li, D.L. Tran, A.C. Shi, K. Dalnoki-Veress, *Soft Matter* **6**, 1258 (2010).
- R. Deegan, O. Bakajin, T. Dupont, G. Huber, S. Nagel, T. Witten, *Nature* **389**, 827 (1997).
- F.I. Li, P.H. Leo, J.A. Barnard, *J. Phys. Chem. B* **112**, 16497 (2008).
- F.I. Li, P.H. Leo, J.A. Barnard, *J. Phys. Chem. C* **112**, 14266 (2008).
- H. Goldstein, *Classical Mechanics*, 2nd edn. (Addison-Wesley, 1980).
- H. Yokoyama, *Mater. Sci. Eng. R* **53**, 199 (2006).
- G.H. Fredrickson, F.S. Bates, *Annu. Rev. Mater. Sci.* **26**, 501 (1996).
- T.P. Lodge, M.C. Dalvi, *Phys. Rev. Lett.* **75**, 657 (1995).

Manuscript v

Swelling molecular entanglement networks in polymer glasses

J.D. McGraw and K. Dalnoki-Veress, Physical Review E, **82**, 021802 (2010).

Swelling molecular entanglement networks in polymer glasses

Joshua D. McGraw and Kari Dalnoki-Veress*

Department of Physics and Astronomy and the Brockhouse Institute for Materials Research, McMaster University, Hamilton, Canada

(Received 3 December 2009; revised manuscript received 21 May 2010; published 9 August 2010)

Entanglements in a polymer network are like knots between the polymer chains, and they are at the root of many phenomena observed in polymer systems. When a polymer glass is strained, cracklike deformations called crazes may be formed and the study of these regions can reveal much about the nature of entanglements. We have studied crazes in systems that are blends of long polymer chains diluted with chains of various small molecular weights. The range of diluting chain lengths is such that a fraction of them have conformations leading to entanglements. It has been found that a system with more short chains added acts like one in which the entanglement density is smaller than that in an undiluted system. We propose a model that quantitatively predicts the density of effective entanglements of a polydisperse system of polymer chains which is consistent with our experimental data.

DOI: [10.1103/PhysRevE.82.021802](https://doi.org/10.1103/PhysRevE.82.021802)

PACS number(s): 61.41.+e, 61.25.hk, 61.25.hp, 82.35.Lr

I. INTRODUCTION

Much of what makes polymer systems distinct from other forms of condensed matter can be traced to the fact that they are composed of long, chainlike molecules whose backbones cannot pass through one another [1]. In a melt of long polymers, thermal fluctuations cause chain conformations to be such that a given chain entangles with other chains in the space that it explores. As a result of these interactions, the mobility of the molecule is severely reduced as compared to smaller molecules. Entanglements restrict the chain's motion perpendicular to its contour length and are affected by several parameters including the volume occupied by the chain and the *pervaded volume*—the volume explored by the chain [1–4].

In equilibrium, polymer chains in the melt state are considered *ideal*, that is, they take on conformations corresponding to random walks [1]. While the volume taken up by a chain scales simply as the molecular weight, $V_c \propto M$, the actual volume explored by the chain through its random path is typically much larger. The pervaded volume of a polymer chain, V_p , can be defined by a sphere whose radius is given by the radius of gyration, R (the root-mean-square distance of all monomers from the center of mass of the chain). For random walks $R \propto M^{1/2}$ [1]. Since the pervaded volume increases with the molecular weight as $V_p \propto R^3 \propto M^{3/2}$, the ratio V_c/V_p is *decreasing* with M : on average a longer chain interacts with more other chains. As we will see, because the pervaded volume of a chain is, on average, occupied by more other chains as M increases, it is more likely for higher molecular weight chains to be entangled. Simply put, the more chains a given polymer chain interacts with the more likely it is to be entangled.

Of fundamental importance in polymer systems are the questions of whether chains are entangled and the nature of the spacing between entanglements. Rheological and glassy state properties of polymers depend crucially on the answers to these questions [5–7] and underpin polymer theory

[1,8–10]. The former of these questions receives significant attention in the polymer literature [1,5,11–14]. There is growing consensus in theoretical, computational, and experimental studies that in a monodisperse system of sufficiently long chains the average molecular weight of a segment between entanglements, M_e , is constant [9,11–13]. In blends of two or more weight fractions of the same polymer species, however, the case is not so clear. Even when the molecular weights of blend components are quite long compared to M_e , it is possible to describe M_e as having been diluted. Recent theoretical and experimental treatments have demonstrated this dilation [10,14] for blends of a long component with either a short or another long component (here “long” or “short” is always in comparison to M_e).

The question of whether a chain is entangled has received considerably less attention. Kavassalis and Noolandi have addressed this question and propose a model which predicts an abrupt transition from zero to finite probability of entanglement as M passes through some critical molecular weight [15]. Here we present a model that also has a low- M region for which the probability of entangling with other molecules is zero, while the transition to finite values is continuous. Our model is compared to measurements of the density of effective entanglements in blends of long- and short-chain polymers shown schematically in Fig. 1(a). The model can be applied to systems with any number of molecular weight components, so we have prepared ternary systems to test the model beyond binary systems. Previous works have focused on blends of long chains with the second component either much shorter than [14,16,17] or significantly longer than M_e [10,14]. In contrast with these studies our work focuses on the transition *through* M_e where one cannot assume that the short chains do not entangle. The questions we seek to answer are, (1) what is the effect of swelling the entanglements that connect a polymer network; and, (2) how does the length of a polymer chain relate to the *probability* that it will be entangled with other chains?

When a polymer glass is strained, microscopic cracklike deformations called crazes may be formed [18–20]. Crazes are composed of a load bearing, interconnected fibrillar structure bridging a gap between undeformed material, and they exist because polymers are entangled [18,19]. Previous

*dalnoki@mcmaster.ca

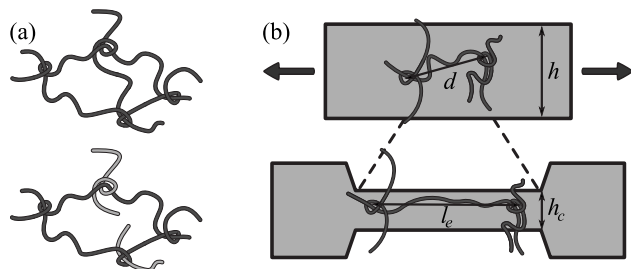


FIG. 1. (a) The entanglements that exist on the vertically oriented chain are rendered ineffective when replaced by short segments. (b) Schematic of the crazed and uncrazed system before and after straining, overlaid with a representation (not to scale) of one polymer molecule, aligned along the strain direction, before and after straining.

studies have focused on understanding the microscopic processes that govern the nucleation, growth, and failure of crazes as the strain increases [18–25]. Drawing on these seminal studies, recent work used atomic force microscopy (AFM) of crazes to probe the configurations of polymers in confinement [26]. It is the aim of this work to continue the use of crazing experiments to understand properties of molecular entanglement in equilibrium. We stress from the outset that the work presented here is done on glassy systems which is in contrast to many dynamic studies of entanglements (e.g., rheology, neutron spin echo). However, since the structure of a glass is inherited from that of the melt, entanglement properties can be elucidated through the use of crazing [18–25]. In this work, we find that there is a range of molecular weights for which the entanglement density can be interpreted as having been reduced from that of long chains. The reduction in the entanglement density is even apparent for chains with molecular weights well above M_e .

In the thin films we study here, crazes are characterized by the ratio of the deformation-induced neck height to the height of the undeformed film, h_c/h . A schematic of a craze region is shown in Fig. 1(b), while an AFM topography image of a craze is seen in Fig. 2. The connection between the essentially macroscopic quantity h_c/h and the microscopic M_e was made some time ago in experiments by Donald and Kramer [18,21,22]; simulations by Rottler and Robbins have further verified the connection [20]. The average distance between entanglements prior to crazing is $d \propto M_e^{1/2}$ since polymers in the melt are random walks. After crazing, the random network of entanglements is expanded in the strain direction. It was shown by Kramer and co-workers that after straining $l_e \propto M_e$ [18,21,22]. Rottler and Robbins determined the proportionality constant in this relationship using simulations [20]. The lengths d and l_e are shown schematically in Fig. 1(b) for the specific case of an entanglement strand aligned along the strain direction (in a random network all orientations are equally probable). Since the deformation of the chains is reflected in the macroscopic deformation of the thin film, it is easy to show that $h_c/h \propto d/l_e \propto 1/M_e^{1/2}$.

A system of very long polymer chains whose molecular weights $M_\ell \gg M_e$ will have a density of entanglements, $\nu \propto 1/M_e$, which is large compared to a system of chains whose molecular weights are small. Just as a string must be

long enough to tie a knot, if the molecular weight of the short chains is too small, then there can be no entanglements. However, because of the random configurations of polymer chains in the melt, an intermediate case also exists, where some short chains are entangled and others are not. Here we consider a *blended* system of very long chains to which one adds some mass fraction, ϕ , of short chains, see Fig. 1(a). The blending approach allows us to elucidate the importance of the entanglement behavior of the shorter chains where this would be much more difficult in monodisperse systems (for example, in the work by Kramer and co-workers [27] it was found that stable crazes could not be observed in monodisperse 37 and 50 kg/mol systems). In a blended system we can say that the entanglements of the large M system have been *swelled* or *diluted* by the small M chains [14,16,17]. We define a density of effective entanglements, $\nu_{eff} \propto 1/M_{eff}$, dependent on the blend concentration, ϕ , that will be intermediate to that of the long- and short-chain systems, $0 < \nu_{eff}(\phi) < \nu$. Since $h_c/h \propto 1/M_{eff}^{1/2}$, we have

$$\left(\frac{h_c}{h}\right)^2 \propto \nu_{eff}. \quad (1)$$

II. EXPERIMENT

Samples were prepared by blending long and short chains of polystyrene (PS) with various mass fractions of the short component, ϕ , in toluene (all PS obtained from Polymer Source Inc.). The number averaged molecular weight of the long chains was $M_\ell = 734$ kg/mol, and that of the short chains was $M_s = 4.8$ or 18.4 kg/mol. Ternary systems were prepared in which the mass fraction of long chains with $M_\ell = 734$ kg/mol is always 0.50. A mass fraction ϕ , of $M_s^{(1)} = 18.4$ kg/mol chains was added while $M_s^{(2)} = 64.0$ kg/mol chains made up the rest of the system. The polydispersity index for all PS was ≤ 1.07 . Films approximately 110 nm thick were spincast from solution onto freshly cleaved mica substrates and annealed for 12 h at 120 °C to remove residual stress and solvent. Films were floated onto

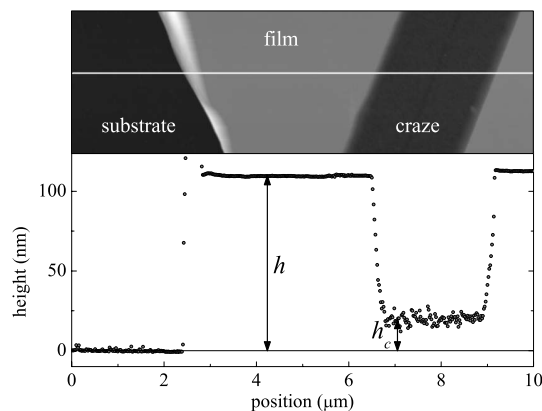


FIG. 2. An atomic force microscope image of a crazed sample showing the substrate, regions of the sample that have been deformed by crazing, and undeformed regions. The plot is a line profile corresponding to the white line.

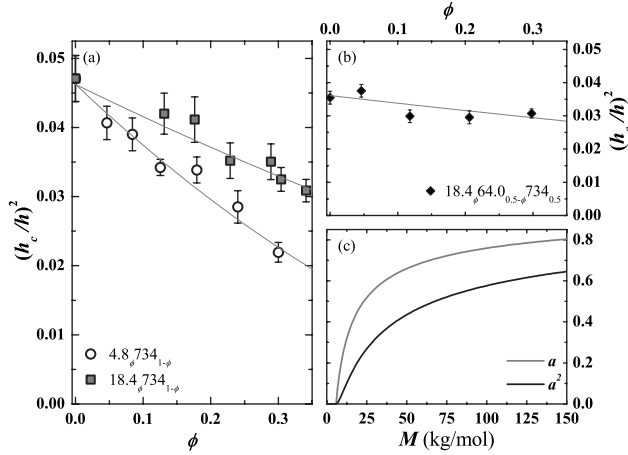


FIG. 3. (a) A plot of $(h_c/h)^2$ as a function of ϕ for the two binary systems with $M_\ell = 734$ kg/mol and $M_s = 4.8$ kg/mol (\circ) or $M_s = 18.4$ kg/mol (\square). (b) A plot of $(h_c/h)^2$ as a function of ϕ for the ternary system with $M_l = 734$ kg/mol, $M_s^{(1)} = 18.4$ kg/mol, and $M_s^{(2)} = 64.0$ kg/mol. The solid lines in (a) and (b) are best fits of the model obtained with $\mu = 5.8$ kg/mol. (c) The functions $a(M)$ and $a(M)^2$ as given by Eq. (3) with $\mu = 5.8$ kg/mol for $0 < M < 150$ kg/mol.

the surface of a clean water bath (Milli Q) and picked up across a 1.5 mm gap between two aluminum blocks with sharp edges and allowed to dry. One of the blocks was fastened to a single-axis translation stage (Newport MFA-CC, SMC100CC), and slowly pulled apart at room temperature until crazes were formed. A constant strain rate of $\dot{\gamma} = 2 \times 10^{-4}$ s $^{-1}$ was used and samples were strained to about $\gamma = 0.1$.

Berger and Kramer [28] have performed crazing experiments at temperatures approaching the glass transition. In these experiments, they observe that an enhanced mobility as the temperature is increased and T_g is approached affects the crazing measurements. These same studies found that deep in the glassy state (approximately 40 K below T_g) the results were independent of temperature. Since the measurements reported here were carried out approximately 80 K below T_g , they are a robust probe of the entangled network in the melt state.

The strained PS samples were transferred to a Si substrate by placing them onto the Si surface and letting surface forces pull the film into contact with the substrate [26]. A scratch was made along the sample exposing the substrate, and the heights h_c and h were measured using AFM in tapping mode (Veeco-Digital Instruments Multimode), an example is shown in Fig. 2. In the image one can see the substrate, the craze, and the unstrained film simultaneously. As suggested by Eq. (1), we plot $(h_c/h)^2$ as a function of ϕ in Fig. 3 [31].

III. RESULTS AND DISCUSSION

Examining the data of Fig. 3(a), we see that as the mass fraction of short chains increases, a decrease in ν_{eff} results. Furthermore, the smaller molecular weight diluent shows stronger attenuation of ν_{eff} . These results can be interpreted

as follows: a crazed polymer system whose constituents are a blend, with $M_\ell \gg M_e$ and other chains with M_s in the vicinity of M_e , acts like a system whose entanglement density is less than the long chain ν of the polymer.

To understand how adding short chains to the network affects ν_{eff} we first suggest how to find the probability that an individual chain with molecular weight M is effectively entangled, and then generalize to the case of a blend. The model is an extension of the chain packing ideas presented by Fetters *et al.* [2,3]: for a given chain to participate in the entanglement network, it must share its pervaded volume with a sufficient number of other chains. The average fraction of interactions a specific chain has with other chains is the same as the average amount of space in the pervaded volume that is available to other chains:

$$a(M) = \left\langle 1 - \frac{V_c}{V_p} \right\rangle. \quad (2)$$

Since $V_c \propto M$ and $V_p \propto R^3 \propto M^{3/2}$ on average, we find

$$a(M) = 1 - \sqrt{\frac{\mu}{M}}, \quad (3)$$

where μ is a constant that is proportional to M_e .

A more rigorous derivation of Eq. (3) can be obtained by averaging over all possible conformations of an ideal chain. Since $V_c = M/\rho_n$, where ρ_n is the polymer's molar mass density, all that remains to evaluate Eq. (2) is to obtain $\langle 1/V_p \rangle \propto \langle 1/R^3 \rangle$ as a function of M . For an ensemble of random walks with a given number of steps (or molecular weight, M), Rudnick and Gaspari [30] have calculated an approximate probability distribution of their radii of gyration. They obtain

$$P(R, M) \propto \left(\frac{R^2}{\beta M} \right)^{1/2} \exp\left(-\frac{3}{2} \frac{R^2}{\beta M} \right), \quad (4)$$

where the proportionality constant is chosen such that $\langle R^2 \rangle = \beta M$. Using this probability distribution, we can calculate $\langle 1/R^3 \rangle$ and thus find that $\langle V_c/V_p \rangle \propto (\rho_n^2 \beta^3 M)^{-1/2}$. Having calculated the second term in Eq. (2), we obtain Eq. (3), with $\mu \propto 1/\rho_n^2 \beta^3$ a polymer specific constant that is proportional to M_e . The proportionality between μ and M_e is demonstrated in Refs. [2,3] where Fetters and co-workers argue that the onset of entanglement occurs when the molecular weight of a chain in the melt is large enough such that V_c/V_p is sufficiently small. These authors use the relations $V_c = M/\rho_n$ and $V_p \propto (\beta M)^{3/2}$ to obtain the result stated above: $M_e \propto 1/\rho_n^2 \beta^3 \propto \mu$.

As in the work by Si *et al.* [26], we assume that the total number of entanglements is given by the sum of the interchain and self-entanglements in a system; a is the fraction of interchain entanglements. Clearly a negative value of a is unphysical and $a = 0$ for $M \leq \mu$. The interpretation of the cutoff, $M = \mu$, is physically intuitive: a chain must have some

minimum length, μ , before it can entangle. Since there is a distribution of entanglement lengths, with M_e being the average, μ must be less than and on the order of M_e .

To determine the degree to which a network of polymer chains with molecular weights M is entangled, we consider that an entanglement is the result of an interaction between two chains. In order for an entanglement to contribute to the network integrity, both chains must be entangled. Above we have calculated $a(M)$ which is the probability of having an interchain entanglement. As is implicit in the chain packing models [2,3] and discussed in the work of Si *et al.* [26], we also assume that the effective entanglements, those that contribute to the network integrity, are with *other* chains. Since the probability of having an interchain entanglement is $a(M)$, the probability that the interaction between two chains contributes to the network is a^2 . Hence, the density of effective entanglements in a network is given by $\nu_{eff} = \nu a^2$, where ν is the entanglement density of a system composed of infinitely long chains ($a=1$).

The previous analysis is easily extended to polydisperse systems. The bimodal blend is made up of long and short chains with molecular weights M_ℓ and M_s . There are three distinct entanglements between the chains: those between like chains (M_ℓ - M_ℓ and M_s - M_s) as well as those between unlike chains (M_ℓ - M_s). The probability that any one entanglement in a system involves a short or long chain is given by the mass fraction of that type of chain in the system, ϕ or $1-\phi$, respectively. The probability that a short chain in a binary system is effectively entangled is then the product $a_s\phi$, where $a_s=a(M_s)$ is given by Eq. (3). Furthermore, the probability that an entanglement between two short chains is effective is $a_s^2\phi^2$. If we take into account the other two types of interactions, we can write down an expression for the effective entanglement density of the system as the sum of contributions from distinct types of entanglements: $\nu_{eff} = \nu[a_s^2\phi^2 + 2a_s a_\ell \phi(1-\phi) + a_\ell^2(1-\phi)^2]$ [32]. This analysis is not limited to binary systems, since one only needs to account for all possible types of interactions between chains in a polymer blend to model the expected entanglement behavior. Taking all interactions into account one obtains

$$\nu_{eff} = \nu \left[\sum_{i=1}^k a_i \phi_i \right]^2, \quad (5)$$

where a_i is given by Eq. (3), ϕ_i is the volume fraction of the M_i molecular weight component, and k is the number of components in the blend.

The data in Fig. 3(a) were fit using Eqs. (1), (3), and (5), with the only free parameters being μ and a prefactor (taking the place of ν in Eq. (5)). The best fit was obtained with $\mu = 5.8 \pm 0.8$ kg/mol. Given this value of μ , we show a plot of $a(M)$ and $a(M)^2$ for PS in Fig. 3(c). Using the parameters obtained for the two binary systems, one can easily extend to the *ternary blends* shown in Fig. 3(b). The fit of the model with only two free parameters for three distinct blend systems (two binary systems and a ternary system) is excellent. Furthermore the value obtained for μ is less than and on the order of M_e for PS as expected ($M_e \sim 13.5$ kg/mol [3]). Indeed we find that $\mu \sim M_e/2$.

The boundary set by $\mu=5.8$ kg/mol indicates that $a_s=0$ for chains with $M_s \leq \mu$. Indeed, for $M_s=4.8$ kg/mol, the smallest value of M_s used in this study, $a_s=0$ is a good description of the data for the binary blend. Blends of PS chains where the short chains are much less than M_e have been studied in similar experiments by Kramer and co-workers [16]. The molecular weight of the diluting chains used in their study was approximately 2 kg/mol which corresponds to $a_s=0$. Our simple model, with a_s set to 0 in Eq. (5), results in $\nu_{eff} \propto (1-\phi)^2$ which gives a satisfying description of the data obtained in [16].

In the blending experiments presented we have been able to probe not only the case where the small chain diluent can be assumed to be entirely nonentangling (i.e., $a=0$), but also the intermediate case where $0 < a < 1$. Because the binary blends with the short-chain diluent $M_s=18.4$ kg/mol show a change in the effective entanglement density that is not equivalent to that of $M_s=4.8$ kg/mol, we must conclude that $a \neq 0$ [see Fig. 3(a)]. The data with $M_s=18.4$ kg/mol indicate that there is some range of molecular weights for which $0 < a < 1$. Hence, there is a range of molecular weights for which $0 < \nu_{eff} < \nu$; this is in contrast to the often assumed idea that polymers are unentangled below M_e and entangled above M_e . Since the 18.4 kg/mol chains have M which is similar to M_e , it may be remarked that this result is not surprising. However, the ternary data shown in Fig. 3(b) provides us with strong evidence that even for a blend with molecular weights considerably above M_e the network is diluted. In particular for the case of the ternary blend with $\phi=0$, the high molecular weight is diluted with only 64.0 kg/mol chains and ν_{eff} is reduced from that of a pure high molecular weight system. To reiterate, even though $M_s=64$ kg/mol chains are well above M_e , we must conclude that some of these chains are diluting the entanglements of the very high molecular weight network. The degree to which a specific molecular weight will contribute to the entanglement network is given by $a(M)$ in Fig. 3(c).

IV. CONCLUSIONS

Polystyrene blends have been prepared and their thin films have been crazed and measured using AFM. We observe that systems with lower overall molecular weight show crazing behavior consistent with a system that has a lower entanglement density. As in the chain packing models [2,3] and the work of Si *et al.* [26], a model that assumes the effective entanglements are those with *other* chains in the system is proposed. We assume that the fraction of space in a chain's pervaded volume occupied by other chains in the system is equal to the probability of interchain entanglements. The density of effective entanglements that are predicted by this model are quantitatively consistent with our measurements for two binary blend systems and a ternary blend with only two fitting parameters. Furthermore, the model is easily extended to the broad molecular weight distributions found in many industrial polymers. The parameter μ is physically significant and represents the length a chain must have before it is even possible to entangle. This cutoff

1982 chain length is found to be approximately one half of the entanglement molecular weight. Our model predicts a continuous change in the entanglement density as a function of molecular weight. The polymer melt is not unentangled below M_e and entangled above M_e , as is often assumed. Rather, we find that low molecular weight chains ($M \leq \mu$) have zero probability to be found in the entangled state, but for

$M > \mu$ the probability rises continuously from zero and asymptotes to unity for infinitely long chains.

ACKNOWLEDGMENT

The authors thank NSERC of Canada for financial support.

-
- [1] P. de Gennes, *Scaling Concepts in Polymer Physics* (Cornell University Press, Ithaca, NY, 1979).
- [2] L. Fetters, D. Lohse, D. Richter, T. Witten, and A. Zirkel, *Macromolecules* **27**, 4639 (1994).
- [3] L. Fetters, D. Lohse, and W. Graessley, *J. Polym. Sci., Part B: Polym. Phys.* **37**, 1023 (1999).
- [4] S. Wang, *Macromolecules* **40**, 8684 (2007).
- [5] J. Ferry, *Viscoelastic Properties of Polymers*, 3rd ed. (Wiley, New York, 1980).
- [6] G. Berry and T. Fox, *Adv. Polym. Sci.* **5**, 261 (1968).
- [7] R. Kusy and D. Turner, *Polymer* **15**, 394 (1974).
- [8] M. Doi and S. Edwards, *The Theory of Polymer Dynamics* (Oxford University Press, New York, 1986).
- [9] A. Likhtman and C. McLeish, *Macromolecules* **35**, 6332 (2002).
- [10] S. Park and R. Larson, *Macromolecules* **37**, 597 (2004).
- [11] R. S. Hoy, K. Foteinopoulou, and M. Kröger, *Phys. Rev. E* **80**, 031803 (2009).
- [12] M. Zamponi, M. Monkenbusch, L. Willner, A. Wischniewski, and D. Richter, *EPL* **72**, 1039 (2005).
- [13] A. Wischniewski, M. Monkenbusch, L. Willner, D. Richter, A. E. Likhtman, T. C. B. McLeish, and B. Farago, *Phys. Rev. Lett.* **88**, 058301 (2002).
- [14] D. Auhl, P. Chambon, T. C. B. McLeish, and D. J. Read, *Phys. Rev. Lett.* **103**, 136001 (2009).
- [15] T. A. Kavassalis and J. Noolandi, *Phys. Rev. Lett.* **59**, 2674 (1987).
- [16] A. Yang, E. Kramer, C. Kuo, and S. Phoenix, *Macromolecules* **19**, 2020 (1986).
- [17] J. Roovers, *Polym. J. (Tokyo, Jpn.)* **18**, 153 (1986).
- [18] E. Kramer, *Adv. Polym. Sci.* **52-53**, 1 (1983).
- [19] E. Kramer and L. Berger, *Adv. Polym. Sci.* **91/92**, 1 (1990).
- [20] J. Rottler and M. O. Robbins, *Phys. Rev. E* **68**, 011801 (2003).
- [21] A. Donald and E. Kramer, *J. Polym. Sci., Polym. Phys. Ed.* **20**, 899 (1982).
- [22] A. Donald and E. Kramer, *Polymer* **23**, 461 (1982).
- [23] H. Brown, *Macromolecules* **24**, 2752 (1991).
- [24] B. Lauterwasser and E. Kramer, *Philos. Mag. A* **39**, 469 (1979).
- [25] H. Brown, *J. Mater. Sci.* **14**, 237 (1979).
- [26] L. Si, M. V. Massa, K. Dalnoki-Veress, H. R. Brown, and R. A. L. Jones, *Phys. Rev. Lett.* **94**, 127801 (2005).
- [27] A. Yang, E. Kramer, C. Kuo, and S. Phoenix, *Macromolecules* **19**, 2010 (1986).
- [28] L. Berger and E. Kramer, *Macromolecules* **20**, 1980 (1987).
- [29] J. Lin and A. Yang, *Macromolecules* **34**, 3698 (2001).
- [30] J. Rudnick and G. Gaspari, *Science* **237**, 384 (1987).
- [31] Lin and Yang [29] and Si *et al.* [26] have shown that AFM can be used to obtain information consistent with the well established transmission electron microscopy (TEM) technique of Kramer and Brown [24,25]. We have further verified this assumption here by directly comparing TEM and AFM measurements.
- [32] If the short component is too short to entangle, then $a_s=0$. In this case the expression is equivalent to the one found elsewhere [14,16,17].

Manuscript vi

Relaxation of non-equilibrium entanglement networks in thin polymer films

J.D. McGraw, P.D. Fowler, M.L. Ferrari and K. Dalnoki-Veress, submitted to European Physical Journal E on 11/10/12, e120229: 8 pages.

Relaxation of non-equilibrium entanglement networks in thin polymer films

Joshua D. McGraw¹, Paul D. Fowler¹, Melissa L. Ferrari¹, and Kari Dalnoki-Veress^{1a}

Department of Physics & Astronomy and the Brockhouse Institute for Materials Research, McMaster University, Hamilton, Canada

Received: date / Revised version: date

Abstract. It is known that polymer films, prepared by spin coating, inherit non-equilibrium configurations which can affect macroscopic film properties. Here we present the results of crazing experiments that support this claim; our measurements indicate that the as-cast chain configurations are strongly stretched as compared to equilibrium Gaussian configurations. The results of our experiments also demonstrate that the entanglement network equilibrates on a time scale comparable to one reptation time. Having established that films can be prepared with an equilibrium entanglement network, we proceed by confining polymers to films in which the thickness is comparable to the molecular size. By stacking two such films, a bilayer is created with a buried entropic interface. Such an interface has no enthalpic cost, only an entropic penalty associated with the restricted configurations of molecules that cannot cross the mid-plane of the bilayer. In the melt, the entropic interface heals as chains from the two layers mix and entangle with one another; crazing measurements allow us to probe the dynamics of two films becoming one. Healing of the entropic interface is found to take less than one bulk reptation time.

1 Introduction

The dynamics of a sufficiently long polymer chain in a melt of like chains will be restricted by topological constraints called entanglements. To a good approximation, each chain in the melt has the configuration of a random walk. Such chains have an ‘end-to-end’ distance – the distance between the ends of the molecule – that scales as the square root of the number of monomers that make up the chain: $R_{ee} \propto N^{1/2}$. While random walks are not space filling, polymer melts are [1,2]. The result of this dichotomy is that each melt chain shares its pervaded volume and interacts with many other chains. A fraction of these interactions are entanglements. Though the precise nature of what constitutes an ‘entanglement’ is still unknown, the chains suffer a restricted mobility as a result of these interactions. The collective effect of the entanglements is to create a ‘tube’ in which the molecule is confined [1,2]. The chain’s motion, termed ‘reptation’, is restricted predominantly to directions along the tube. It is well known that these entanglement constraints are largely responsible for many phenomena in polymer physics, such as: high melt viscosity [3,2] and viscoelasticity [4–6]; enhanced adhesion [7,8]; glassy failure mechanisms [9–11]; pronounced confinement effects [12,13]; and altered hydrodynamic boundary conditions [14,15].

Since the entanglement network of a polymer melt greatly influences many properties, it is important to make

the distinction between equilibrium and non-equilibrium melts. If the chain statistics in a melt are not at equilibrium, then the entanglement network will also be out of equilibrium. As such, measurements of the properties listed above are typically affected. There has been significant interest in non-equilibrium network effects: several studies have investigated the effects of preparation and annealing treatments on the viscosity [16,17], capillary wave spectra [18], thermal expansion [19] and residual stress [20–26] in polymer films. In these studies, the non-equilibrium structure is inherited from the film casting process. During the preparation of films by casting from solution, polymer chains vitrify at non-zero solvent content. The presence of solvent results in chains that are swollen in comparison to melt conformations. Since the solvent is volatile, most of it leaves the system and the chains are forced into configurations that are not typical of the equilibrium melt. Since the lateral extent of a film does not change, the structure must compress in the direction normal to the film as solvent leaves – annealing above the glass transition temperature, T_g , allows these perturbed networks a chance to evolve towards equilibrium. A schematic of the typical experiment, showing a chain with a ‘non-equilibrium configuration’ being annealed towards an ‘equilibrium configuration’ is seen in Fig. 1(a).

The interface of a film also perturbs chain conformations, which results in another method of preparing non-equilibrium samples. Chains at a neutral interface, like

^a email: dalnoki@mcmaster.ca

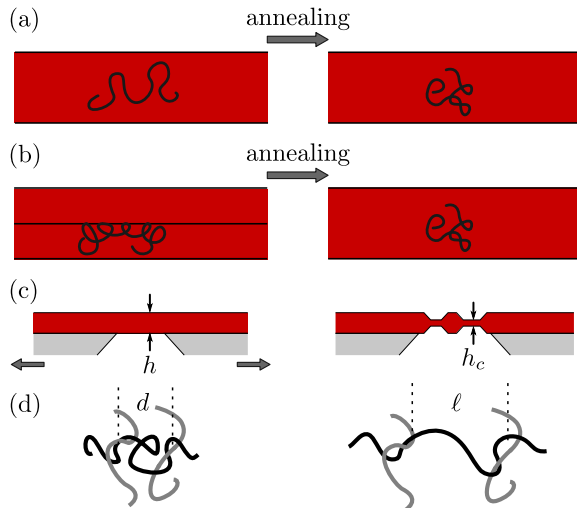


Fig. 1. Schematics of the experiments presented in this work. (a) A chain with a swollen configuration in after spin coating. The ensemble of chains recovers equilibrium chain statistics after some period of annealing above T_g . (b) A chain at the ‘entropic interface’ of a bilayer film prepared by stacking two glassy films. Upon annealing above T_g , the Brownian motion of segments allows the entropy deprived ensemble to relax towards equilibrium. (c) In a crazing experiment, a glassy free standing film with thickness h is strained and necks of material, with thickness h_c are formed. (d) Microscopically, the segments of chains between entanglements have typical size d before straining, and are pulled to a length of ℓ during the crazing experiment.

a free air or vacuum surface, were described by Silberberg [27]. According to Silberberg’s reflection principle, chains that in the absence of a boundary would cross it are instead reflected back into the melt. These chains are thus unable to explore some conformations resulting in a loss of entropy. The significance of this entropy loss has been discussed in relation to the number of inter-chain entanglements, those between two different chains, that exist near an interface [12]. In [12], Brown and Russell suggest that there is a reduction in the number of inter-chain entanglements near an interface; corresponding measurements support this idea [13, 15, 28]. In these studies, a distinction is made between inter-chain entanglements and those that occur between two segments far apart on the same chain. In light of the chain packing models [29, 30] which define entanglements through the interactions of a test chain with other chains, in [13] it was proposed that inter-chain entanglements and intra-chain entanglements do not contribute equally to the integrity of the network. The topological difference between inter- and intra-chain entanglements was suggested to be responsible for the observed thickness dependence of crazing experiments on thin glassy films [13].

While it is possible for polymer chains in a film to be in equilibrium with a reflective boundary, it is also possible to destroy that equilibrium by stacking two such films.

This bilayer film results in a sample with what we will refer to as an ‘entropic interface’ – an interface that has an entropic cost associated with the restricted configurations of the molecules that do not cross the mid-plane of the bilayer. As chain segments undergo Brownian motion when annealed above T_g , entropy is recovered as the chains explore a larger pervaded volume. This experiment is schematically depicted in Fig. 1(b).

The literature on chains crossing such entropic interfaces is vast. In particular, early experiments by Klein [31] and others [32–34] were some of the first to put on firm footing the reptation arguments [1, 2, 35] that have been crucial to understanding the physics of long chain polymer melts. In other experiments, the fracture energy is measured as a function of annealing time between the interfaces [36]. Reptation arguments have been employed to understand these results [37, 7, 38] and simulations are used to investigate these problems [39]. Up to now however, direct measurements of the entanglement density across an atomically smooth entropic interface have not been made, in part because we have few experimental probes to quantify this property.

As mentioned above, entangled polymeric materials can fail in a way that is distinct from many other modes of glassy failure. The difference arises from the glass being composed of an entangled polymer network. This failure mode, called crazing [9, 10, 40, 41], is like the ductile failure that occurs in metals in that a drawing stress can produce ‘necks’ of deformed material. However, the crazing process is quite different on a molecular level, as the drawn material has a fibrillar structure in which the polymer chains have configurations that are strongly non-Gaussian. The fibrillar material in a craze is characterized by an extension ratio, λ , defined by the ratio of the craze width, to the width of undeformed material that went into forming the craze. If a thin film with thickness h is crazed, using conservation of volume and assuming that the density of the crazed film and unperturbed film are the same, it can be shown that $\lambda \propto h/h_c$, where h_c is the average thickness of crazed material [13, 42–44]. A schematic of the crazing process in a thin film is shown in Fig. 1(c).

Donald and Kramer [45, 46] proposed that for equilibrated polymer films the extension ratio can be understood by assuming that entanglements act like chemical cross links, which remain fixed throughout the crazing process. While a polymer glass is being crazed, the chain segments between entanglements (entanglement strands), with entanglement molecular weight M_e , are extended such that the distance between entanglements after crazing is $\ell \propto M_e$. Polymer chains undergo random walks down to length scales approaching the monomer size, thus the end-to-end distance of the entanglement strand before crazing was $d \propto M_e^{1/2}$. Since the macroscopic response is a result of the microscopic process, the extension ratio of the craze is the same as that for an average entanglement strand. Therefore, we have $(h_c/h)^2 \propto (d/\ell)^2 \propto 1/M_e$. By recognizing that the density of entanglements is inversely proportional to the mass of a chain segment between en-

tanglements, we have the relation

$$\left(\frac{h_c}{h}\right)^2 \propto \nu_{\text{eff}}, \quad (1)$$

where ν_{eff} is the density of effective entanglements that would be present in a system of equilibrated Gaussian chains. Therefore, by making a measurement of the essentially macroscopic extension ratio, we directly gain information about the microscopic entanglement network. This model was verified by Donald and Kramer [45,46] in experiments, was observed in molecular dynamics simulations by Rottler and Robbins [40,41], and has since been used in many other experiments [10,13,44,47].

In this work, we take advantage of the fact that measuring the craze extension ratio provides information about the entanglement network [13,44] to gain insight into the equilibration process of two non-equilibrium polymer entanglement networks. In the first case, we examine the dependence of the measured $(h_c/h)^2$ on the casting temperature and subsequent annealing time. After learning how to equilibrate an entanglement network, inasmuch as the crazing measurement is concerned, we turn to the creation and healing of the entropic interface provided by a bilayer film.

2 Experiment

Polystyrene (PS) with weight averaged molecular weights $M_w = 785$ and 1144 kg/mol and polydispersity indices ≤ 1.07 (Polymer Source, Inc.) were used to prepare the samples; we refer to these as PS(785k) and PS(1144k). Polymer of a given molecular weight was dissolved into toluene (Fisher Scientific, Optima grade) in various weight fractions ($0.5 < \phi < 2.5$ wt%) and spin coated onto freshly cleaved, 30×30 mm² mica sheets (Ted Pella, Inc., Hi-Grade, V2). Spin coating was predominantly carried out under ambient conditions; however, in order to explore the effects of temperature several films were also prepared with the substrate attached to a temperature controlled spin coater chuck. The chuck, an aluminum plate in intimate contact with the substrate, ranged in temperature from $5 \leq T \leq 40$ °C. Since the thermal mass of the mica substrate and PS/toluene solution is small compared with that of the spin coater chuck, we assume that the solution temperature at the onset of spin coating is close to that measured on the chuck. Because the temperature gradients are large due to the evaporative cooling of the solvent, the temperature controlled measurements serve only to vary the ‘ambient’ conditions of spin coating. For all monolayer experiments of the type depicted in Fig. 1(a), samples were 105 ± 10 nm thick and composed of PS(785k). Note that we use the terminology ‘monolayer’ to describe a sample consisting of a single film, rather than a molecular monolayer; we refer to two such films stacked on top of one another as a bilayer. For the study of spin coating effects, monolayers were annealed at 130 ± 1 °C $> T_g \approx 97$ °C in a home built vacuum oven (pressure $\sim 10^{-5}$ mbar provided by a turbo molecular

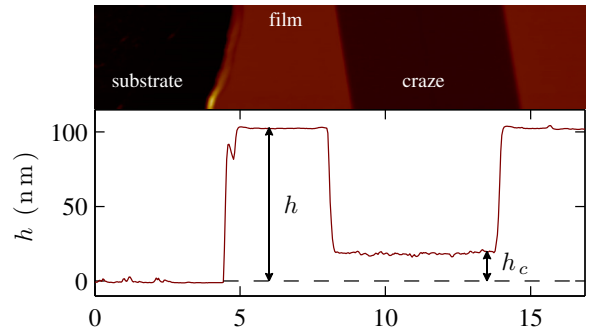


Fig. 2. Height as a function of position from an AFM experiment for a typical crazed thin film after transfer to a Si substrate. From data sets such as these, the film height h , and the craze height h_c are easily determined.

pump), for times $0 \leq t_m \leq 348$ hr. Here and throughout, the subscript ‘m’ refers to monolayer samples.

In order to prepare bilayer films, we first followed the above procedure for monolayer preparation, except that the monolayers were prepared from PS(1144k), were 50 ± 3 nm thick, and annealed at 150 °C for $t_m = 48$ hr¹. After annealing, a monolayer was floated onto the surface of an ultra pure water bath (18.2 M Ω cm, Pall, Cascada LS) and a second monolayer, still on a mica substrate, was placed onto the floating monolayer with the polymer-side down, thus creating a PS bilayer². After preparation, the bilayers were annealed for periods $0.5 \leq t_b \leq 90$ hr at 130 °C (subscript ‘b’ refers to bilayers) in vacuum ovens or on a microscope hot stage (Linkam) under ambient conditions. The temperature is always known to within 1 °C.

With mono- and bilayers prepared, $\sim 9 \times 9$ mm² sections of the films were floated onto the surface of an ultra clean water bath and were picked up using a set of two polished and sharp aluminum blocks. The blocks had a fixed gap of $l = 1.5$ mm between the two sharp edges. After drying, one of the blocks was held in place while the other was attached to a translation stage (Newport MFA-CC, SMC100CC). The blocks were then un-fixed and the film was deformed with a strain rate of $\Delta l/l = 2 \times 10^{-4}$ s⁻¹ until crazes were visible under an optical microscope, see Fig. 1(c). The samples were typically strained to $\Delta l/l = 0.1$, which resulted in a film with both crazed and undeformed material. Typical craze widths were ~ 10 μ m.

¹ As will become clear below, this time is sufficient to ensure an equilibrium entanglement network within the resolution of our experiment

² One particular advantage of doing these experiments with spin coated monolayers is that the surfaces have a highly uniform topography (rms roughness ~ 0.3 nm as measured with AFM), ensuring intimate contact between the interfaces. A second advantage of this approach is the fact that we prepare an entropic interface while ensuring that the chains at that interface will not have suffered chain scission. Thus, we can assume a monodisperse chain length distribution at the interface.

Crazed PS films ($\sim 1.5 \times 9 \text{ mm}^2$) were placed onto $10 \times 10 \text{ mm}^2$ Si wafers. Surface forces pull the crazed film that bridges the aluminum gap into contact with the wafer, thereby transferring the delicate sample to the robust Si surface [13,44]. Scratches were put into the film using a scalpel blade. By measuring an appropriate spot along the edge of a scratch, we are able to simultaneously measure the undeformed film height, h , and the height of the craze, h_c relative to the Si substrate surface. An example of such a measurement is shown in Fig. 2.

3 Results and discussion

This section is broken into two parts. First, we describe the results of experiments on simple monolayer PS films as shown in Fig. 1(a): both the state of as-cast films, and the evolution of these films towards equilibrium will be discussed. We establish that, with extensive annealing above T_g , films may be prepared such that they display the same entanglement density as that of the bulk. Then, we discuss our results on bilayer films with a buried entropic interface, as shown schematically in Fig. 1(b).

3.1 Monolayers

as-cast films

In Fig. 3(a) is shown a plot of the measured ratio $(h_c/h)^2$ as a function of the temperature of the spin coater chuck on which films were prepared. Additionally, the inset of Fig. 3(a) shows the data obtained at $T = 20^\circ\text{C}$ in the main figure. For each trial number, data is grouped according to preparation under a given set of experimental conditions. The data in the inset was obtained under ambient conditions using various initial solution concentrations, while adjusting the spin speed to ensure constant resultant thickness. Additionally, we varied the toluene solvent content in the atmosphere during spin coating. It is clear from the inset that there is great scatter in the resulting $(h_c/h)^2$.

In Fig. 3(b) are shown two histograms of $(h_c/h)^2$ for films prepared on a spin coater chuck at $T = 5$ and 30°C ; N is the number of measurements of the type shown in the plot of Fig. 2. Each data point in Figs. 3, 4 and 5 is the mean value of such a distribution: in Figs. 3 and 4, the distance from the bottom to the top of an error bar is one standard deviation of the distribution. As such, the reported error in these figures indicates the range of expected values one might obtain from an experimental measurement of $(h_c/h)^2$.

The data of Fig. 3 indicate that $(h_c/h)^2$ of as-cast films is sensitive to the temperature at which they are prepared. Furthermore, at a given temperature, this quantity is non-trivially dependent on the preparation conditions; even under ambient conditions, the data spread is 20% of the mean value measured at room temperature. Despite our best efforts, we find that there is great variation in the

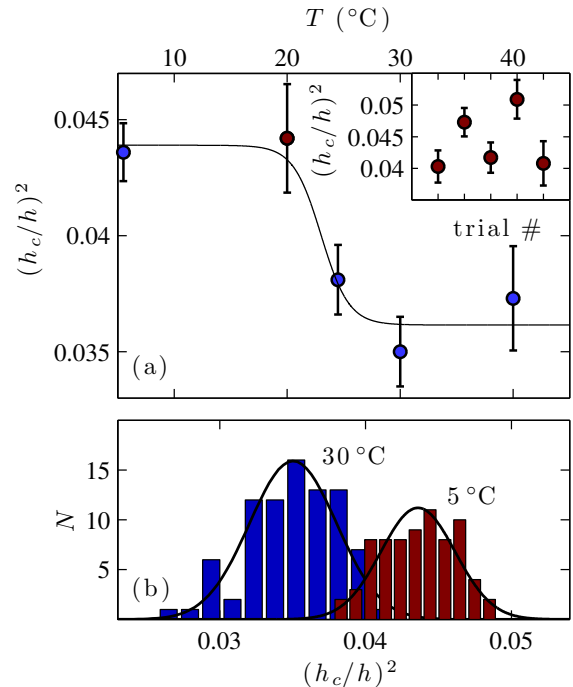


Fig. 3. (a) Plot of $(h_c/h)^2$ as a function of spin coating temperature. The data point in red at $T = 20^\circ\text{C}$ is detailed in the inset. There, data from films prepared under different ambient conditions is shown. The solid black line is a guide for the eye. (b) Histograms for a number of measurements of the type shown in Fig. 2. For all data in (a), error bars are standard deviations from distributions of the type shown (b).

measured values of $(h_c/h)^2$ for films cast under ambient conditions.

In Fig. 4, we see that the values of $(h_c/h)^2$ at $t_m = 0$ (no annealing above T_g) are enhanced as compared to the data at late times. As explained in detail below, chain stretching can account for an enhanced $(h_c/h)^2$ as compared to the measured equilibrium values at long times in Fig. 4. Thus, we will now describe two mechanisms by which chains in the as-cast state may become swollen or stretched as compared to their melt equilibrium. We note that while the experimental results provide a robust characterization of the films, the interpretation of the as-cast data is speculative.

The first mechanism we consider results from the fact that chains in the presence of an athermal solvent are swollen in comparison to the melt. The well established crazing model, described in the introduction, tells us that $(h_c/h)^2 \sim \nu_{\text{eff}}$ is valid for equilibrated films because it is based on the Gaussian random statistics of polymer chains: $d \propto M_e^{1/2}$. Clearly, we must take care to interpret the measured values of $(h_c/h)^2$ plotted in Figs. 3 and 4 as simply proportional to the entanglement density. More generally, the entanglement segments can have end-to-end distance $d \propto M_e^n$, see Fig. 1(d). While for equilibrated polymer films, $n = 1/2$, here we assume $n > 1/2$ since

the chain configurations are formed during the spin coating process while still swollen by solvent. After crazing, the segments between entanglements are stretched and we have $\ell \propto M_e$. Following the same logic that precedes Eq. 1, we have $h_c/h \propto d/\ell \propto M_e^{n-1}$. Thus, if $n > 1/2$ for stretched chains, then for constant M_e , the measured value of $(h_c/h)^2$ will be larger as compared to an equilibrated system. The enhancement is due to the fact that swollen chains can be stretched less before having to draw new material into a craze³.

The second mechanism which can explain an enhanced value of $(h_c/h)^2$ for as-cast films is due to the hydrodynamics of spin coating. During spin coating a polymer solution is deposited onto a substrate at rest. From rest, the substrate is rapidly rotated, producing considerable shear at the substrate-solution interface. As described by Em-slie and co-workers several decades ago [48], the height profile of the liquid atop the substrate quickly becomes flat and there is a radial flow that is balanced by a viscous Poiseuille flow in the vertical direction. This flow produces shear both in the plane of and in the direction normal to the substrate. The shear may be large enough for polymer chains to become oriented to the flow. At vitrification, these flow oriented chains would become trapped in configurations that are stretched in comparison to Gaussian chains. This stretching would result in an enhanced value of $(h_c/h)^2$.

In the studies by Steiner and co-workers [16,17], the apparent viscosity of as-cast polymer films is measured using an electro-hydrodynamic method. Their films, prepared from PS and toluene solutions, showed a decrease in the viscosity of the as-cast state as compared to annealed films. Tsui and co-workers [18] also measure the viscosity of PS films cast from solvents of various quality, ranging from $T \lesssim \Theta$, with Θ the temperature at which chain dimensions are indistinguishable from the melt, to $T > \Theta$ (by contrast, our films are always prepared with $T \gg \Theta$). Using a method of spectral analysis, they find the viscosity of as-cast films to be reduced from its value at long annealing times. Reiter and co-workers [19,22,23,26] have used dewetting to probe the behaviour of as-cast films. They observe that the radius of a dewetting hole is larger for an as-cast film when compared to a hole grown for an identical period in a film aged below T_g . All of these results are consistent with a reduced entanglement density in as-cast films, and this idea is often invoked to explain these observations. If the interpretation of our results for as-cast films is to be consistent with the reduced entanglement density claimed by others, then it must be that the chain configurations trapped in the as-cast films are stretched beyond that of typical Gaussian chains (either due to swelling by solvent or hydrodynamic shearing effects). Since we measure an enhanced $(h_c/h)^2$ in the as-cast state, it must be that the degree of chain stretching we observe is quite severe. A lower entanglement density

³ In [42,43], it is shown that crazes grow in width by continuously drawing new material from the undeformed film and maximally stretching this new material, before drawing in more.

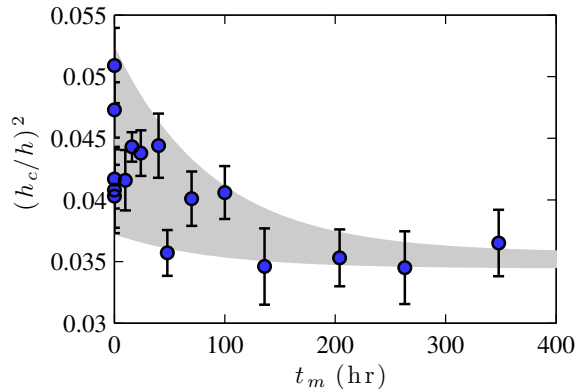


Fig. 4. $(h_c/h)^2$ for monolayers spin cast and annealed for times t_m . Since the non-equilibrium state at $t_m = 0$ could not be well controlled, there are a range of values reported. We expect a measurement at subsequent annealing times to be found anywhere within the shaded region.

with Gaussian statistics would lead to a depressed $(h_c/h)^2$; thus, the stretching and swelling must be enough to dominate this effect. Support for this idea can be found in the systematic studies of the pre-stress in spin coated polymer films [20–24]. In these works, the idea of molecular chain stretching is precisely the supposed origin of the studied pre-stress.

We now turn to the dependence of $(h_c/h)^2$ on the temperature of the spin coating chuck. The temperature range shown in Fig. 3 is high enough so that the PS chain statistics in toluene can be considered as athermal; that is, the average size of an isolated chain in solution does not vary significantly with temperature. Therefore, with this solvent we cannot attribute the observed temperature dependence of $(h_c/h)^2$ to changes in the solvent quality of the film preparation. This was claimed as the dominant effect responsible for some of the rheological behaviour seen in previous studies [18,19,23]. During the spin coating process, solvent continuously evaporates and the sample vitrifies at a non-zero solvent content. At a lower spin coating temperature, the sample vitrifies with a higher solvent concentration than at a higher temperature. Therefore, without considering the highly violent, non-equilibrium process of spin coating, the chains in films prepared at lower temperatures are necessarily more swollen than their counterparts prepared at higher temperatures. As discussed above, crazing a sample in which the chains were trapped in pre-stretched configurations may account for the general trend of higher $(h_c/h)^2$ observed at lower temperatures in Fig. 3.

To summarize our results on the as-cast monolayer films, we find that the measured value of $(h_c/h)^2$ is enhanced in an as-cast film as compared to a film annealed above T_g for long times (see Fig. 4). We propose that the enhancement is due to pre-stretching of the chains during the spin coating process that may occur because of solvent swelling or hydrodynamic shearing. Lastly, the tempera-

ture at which spin coating proceeds greatly affects the nature of entanglements in as-cast films, even for films prepared from an athermal solvent.

temporal evolution of as-cast films towards equilibrium

Given the sensitive temperature and environmental dependence of the as-cast extension ratio, the as-cast chain configurations cannot represent those of the equilibrium melt. As such, high temperature annealing, with $T > T_g$, is expected to result in an evolution towards the equilibrium melt chain statistics. Following a quench to room temperature after an annealing treatment, we would expect to observe differences in $(h_c/h)^2$. In Fig. 4 is shown the results of experiments, using PS(785k), for which films were annealed for various times, t_m , before crazing. The data in the inset of Fig. 3(a) is shown at $t_m = 0$. As described above, it can be seen that the as-cast state has a larger $(h_c/h)^2$ than for longer annealing times. The data plateaus on a time scale $\tau_m \approx 80$ hr. To extract this time scale, we have performed a best fit to all the data using an exponential function: $(h_c/h)^2 = A_m + B_m e^{-t_m/\tau_m}$. The best fit parameters were $A_m = 0.035$, $B_m = 0.001$ and $\tau_m = 80$ hr.

From the data at $t_m = 0$ in Fig. 4, we can see that our preparation under standard laboratory conditions yields a spread of measured $(h_c/h)^2$. However, independent of the preparation, thermal annealing brings all samples toward the same equilibrium state. Within the error of our experiment, all values of $(h_c/h)^2$ after $t_m = 100$ hr are the same. The longest relaxation time of a polymer melt is the reptation time, τ_{rep} , which represents the typical time taken for a molecule in the bulk to lose memory of all previous strains [2]. For PS(785k) at 130 °C, the reptation time is approximately 35 hr [49]. Thus we conclude that the out-of-equilibrium network of the as-cast films relaxes on a time scale ($\tau_m = 80$ hr) that is on the order of one reptation time ($\tau_{rep} \sim 35$ hr).

In the work by Steiner and co-workers [16, 17] as well as Tsui and co-workers [18] described above, the viscosity is probed. In these cases, the time constants for the evolution of the viscosity towards equilibrium is found to be between two and five orders of magnitude longer than the bulk reptation time. These measurements are in stark contrast to the crazing results presented here. As a possible explanation for the discrepancy, we note that in the measurements of Steiner and coworkers, the film surface is perturbed by only ~ 5 nm – a distance that is similar to the distance between entanglement points, or tube-diameter, of PS [29]. Similarly, in the experiments of Tsui and co-workers, it is the capillary wave spectra that are measured, and variations in the height of the samples in the sub-nanometre regime are typical. In addition, the capillary wave measurements are carried out on 14 nm thick samples, which may already be thin enough to observe confinement effects. By contrast, in the crazing measurement the entire film of ~ 100 nm thickness is probed – crazing reports a ‘bulk’ film property. It is then possible that the origin of the significant discrepancy in relaxation timescales

is the result of a subtle and interesting effect which is particular to the interfacial regions of the polymer films studied in [16–18].

3.2 Bilayers

In the previous section, we discussed that as-cast films are characterized by a non-equilibrium entanglement network. Furthermore, we established that the as-cast films can be equilibrated on timescales comparable to the longest relaxation time of the polymer. We now turn to the results observed in another non-equilibrium entanglement network: bilayer films with a buried entropic interface, as shown schematically in Fig. 1(b).

As discussed in the introduction, chains at an interface are subject to the Silberberg reflection principle [1, 12, 27], which states that chain segments that would have crossed the interface are instead reflected back into the polymer melt. These chains thus share their pervaded volumes with fewer other chains, compared to chains in the bulk (see p. 61 in [1]). The influence of the reflection principle on the measurement of $(h_c/h)^2$ was exploited by Si and co-workers [13]. It was found that a film whose thickness is similar to the unperturbed coil radius has a lower $(h_c/h)^2$. The results were interpreted as being due to a reduced inter-chain entanglement density at an interface, similar to ideas first proposed by Brown and Russell [12].

In our experiments, the monolayers used to prepare the bilayers were thin enough to have $(h_c/h)^2$ values that are markedly different from the thick film regime as measured by Si and co-workers [13]; while the end-to-end distance of PS(1144k) is approximately 70 nm [50], the bilayers were made from two films with $h \approx 50$ nm. These monolayers were annealed as described in the experimental section, with annealing times $t_m > 10 \tau_{rep}$ [49]. Given the results of Fig. 4, we assume that the resulting monolayers had chain statistics described by the equilibrium value corresponding to the confined films. We stress that the thickness of the monolayers was chosen specifically: the monolayers are thin enough such that they exhibit a reduced effective entanglement density, while a film thickness corresponding to twice that thickness has a bulk-like entanglement density according to the work by Si and co-workers [13]. Thus, a bilayer film will show a reduced $(h_c/h)^2$ which approaches the bulk value upon annealing.

In Fig. 5 are shown the results of measurements on bilayer films annealed for times t_b at $T = 130$ °C, well above T_g . The errors reported are the standard error of the mean as taken from distributions similar to those in Fig. 3(b). The data in Fig. 5 is well described by an exponential: $(h_c/h)^2 = A_b - B_b e^{-t_b/\tau_b}$. The best fit to the data corresponds to $A_b = 0.0363$, $B_b = 0.0051$ and $\tau_b = 5.1$ hr. Given that the reptation time of PS(1144k) at 130 °C is approximately equal to 120 hr, we find that the relaxation across the entropic interface is achieved much faster than one bulk reptation time. Since at $t_b = 0$ there are no entanglements across the interface, and after equilibration the bulk-like entanglement density is achieved, we can in-

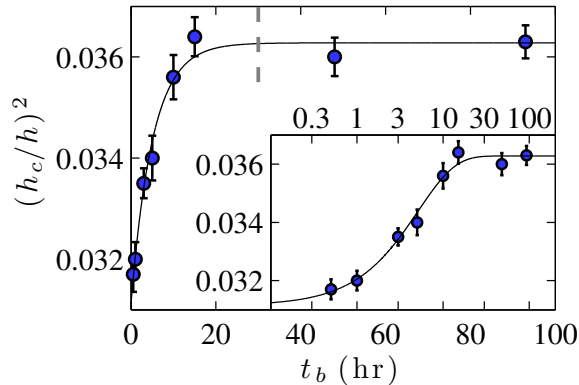


Fig. 5. $(h_c/h)^2$ as a function of annealing time, t_b , for bilayer samples prepared by stacking two monolayer films with thickness ~ 50 nm. The vertical dashed line indicates $\tau_{\text{rep}}/4$. To emphasize the data at early times and the agreement with an exponential relaxation, the inset shows the same data as in the main figure, except with a logarithmic time axis.

interpret the increase in $(h_c/h)^2$ as a direct measure of the change in entanglement density across the interface.

Here we consider the scenario in which a molecule is most severely confined by the entropic interface. This occurs when the molecule's centre of mass would have been found at the location of the interface in the absence of a barrier (see Fig. 1(b)). In this case, the chain's average pervaded volume is exactly half of that in the bulk. Since a molecule in this state is maximally perturbed, this scenario provides an upper bound on the time it takes the bilayers to lose memory of the entropic interface. Even though polymer chains are confined near a reflecting boundary, we expect the molecules to move predominantly by reptation. This is the assumption that has been made in models used to explain, for example the recovery of fracture toughness of polymer-polymer interfaces, and more generally the diffusive processes across these interfaces [7,36,37]. A molecule that is maximally perturbed must relax such that its pervaded volume increases by a factor of two. By analogy with molecular relaxation in the bulk, the molecule must diffuse by a distance of roughly $R_{ee}/2$ to lose the memory of its confinement. Notwithstanding the possibility that the dynamics of polymer chains at an interface may be altered by confinement [28], the diffusion equation dictates that the time it takes for a typical bulk polymer chain to diffuse by a distance $R_{ee}/2$ corresponds to a time $\tau_{\text{rep}}/4$. Thus, by making a simple bulk reptation argument, and invoking the reflection principle, we find that the maximum time taken to lose memory of the bilayer interface is less than τ_{rep} . In Fig. 5, we have inserted a vertical dashed line at $t_b = \tau_{\text{rep}}/4$. The data has clearly saturated by this time. The relaxation time that we measure, τ_b , is representative of the average relaxation time for perturbed chains near the interface, with $\tau_{\text{rep}}/4$ being an upper bound.

3.3 Equilibria of as-cast monolayer and bilayer films

A condition for equilibrium is that a system can arrive at the state independent of the initial condition. In the previous two sections of this work, we have described the preparation and evolution towards equilibrium of two non-equilibrium states: as-cast monolayer films and bilayers prepared with an entropic interface. In both cases, we observe that after a sufficient relaxation time $(h_c/h)^2$ reaches a plateau. Examining the long time behaviour of Figs. 4 and 5 we see that, within error, both non-equilibrium systems reach the same plateau value having started from different initial conditions. That $(h_c/h)^2$ is independent of the preparation after long annealing times is a strong indication that these films are at true equilibrium. To qualify this statement, we cannot rule out long term changes beyond the resolution of the crazing measurement.

4 Conclusion

We have performed a series of crazing measurements designed to probe non-equilibrium states of thin polymer films. In the first case, we examine the effect of spin coating on the resulting craze characteristic, $(h_c/h)^2$. We find that the as-cast films display strongly non-equilibrium behaviour that is difficult to control even under ambient conditions. The measured values of $(h_c/h)^2$ can be reconciled with results from other researchers [16–19,22,23,26] if we interpret the as-cast films as having trapped molecular configurations that are stretched compared to the equilibrium Gaussian statistics. Thermal annealing of these films results in an exponential approach to a plateau in $(h_c/h)^2$, and the equilibration time is consistent with relaxation on a time scale comparable to the polymer reptation time.

Having established that it is possible to prepare monolayer films with an equilibrium entanglement density, we measured $(h_c/h)^2$ in bilayers prepared by stacking two monolayer films. Such a bilayer film is then equivalent to a film with the thickness of two monolayers, but differs in that there is an entropic interface. The interface has no enthalpic penalty and only a diminished entropy due to fewer available molecular configurations. The monolayers were chosen such that they confine the long chain molecules resulting in a reduced effective entanglement density, while a film of twice the monolayer thickness exhibits a bulk-like entanglement density. We find that the as-prepared bilayers craze in a way that is consistent with previously reported measurements on confined monolayers. Thermal annealing above T_g causes the entropic interface in the middle of the bilayer to heal, effectively converting the bilayer into a single film. The healing of the entropic interface occurs on a time scale that is shorter than one bulk reptation time.

Financial support from NSERC of Canada is gratefully acknowledged.

References

1. P.G. de Gennes. *Scaling Concepts in Polymer Physics*. Cornell University Press, 1979.
2. M. Rubinstein and R.H. Colby. *Polymer Physics*. Oxford University Press, 2003.
3. G.C. Berry and T.G. Fox. *Adv. Polym. Sci.*, **5**, 261 (1968).
4. J.D. Ferry. *Viscoelastic Properties of Polymers, 3rd ed.* John Wiley & Sons, Inc., 1980.
5. T.C.B. McLeish. *Advances in Physics*, **51**, 1379 (2002).
6. A.E. Likhtman and T.C.B. McLeish. *Macromolecules*, **35**, 6332 (2002).
7. H.H. Kausch and M. Tirrell. *Annual Reviews of Materials Science*, **19**, 341 (1989).
8. C. Cretton, E.J. Kramer, H.R. Brown, and C.-Y. Hui. *Advances in Polymer Science*, **156**, 53 (2001).
9. E.J. Kramer. *Adv. Polym. Sci.*, **52/53**, 1 (1983).
10. E.J. Kramer and L.L. Berger. *Adv. Polym. Sci.*, **91/92**, 1 (1990).
11. H.R. Brown. *Macromolecules*, **24**, 2752 (1991).
12. H.R. Brown and T.P. Russell. *Macromolecules*, **29** 798 (1996).
13. L. Si, M.V. Massa, K. Dalnoki-Veress, H.R. Brown, and R.A.L. Jones. *Phys. Rev. Lett.*, **94** 127801 (2005).
14. F. Brochard-Wyart, P.G. de Gennes, H. Hervet, and C. Redon. *Langmuir*, **10**, 1566 (1994).
15. O. Bäümchen, R. Fetzer, and K. Jacobs. *Physical Review Letters*, **103**, 247801 (2009).
16. D.R. Barbero and U. Steiner. *Physical Review Letters*, **102**, 248303, (2009).
17. K.R. Thomas, A. Chenneviere, G. Reiter, and U. Steiner. *Physical Review E*, **83**, 1 (2011).
18. N.R. Li, A. Clough, Z. Yang, and O.K.C. Tsui. *Macromolecules*, **45**, 1085 (2012).
19. A. Clough, M. Chowdhury, K. Jahanshahi, G. Reiter, and O.K.C. Tsui. *Macromolecules*, **45**, 6196 (2012).
20. S.G. Croll. *Journal of Applied Polymer Science*, **23**, 847 (1979).
21. G. Reiter, M. Hamieh, P. Damman, S. Slavons, S. Gabriele, T. Vilmin, and E. Raphaël. *Nature Materials*, **4**, 754 (2005).
22. P. Damman, S. Gabriele, S. Coppée, S. Desprez, D. Villers, T. Vilmin, E. Raphaël, M. Hamieh, S. Al Akhrass, and G. Reiter. *Physical Review Letters*, **99**, 036101 (2007).
23. A. Raegen, M. Chowdhury, C. Calers, A. Schmatulla, U. Steiner, and G. Reiter. *Physical Review Letters*, **105**, 227801 (2010).
24. K.R. Thomas and U. Steiner. *Soft Matter*, **15**, 7839 (2011).
25. F. Closa, F. Zeibert, and E. Raphaël. *Physical Review E*, **83**, 051603 (2011).
26. M. Chowdhury, P. Freyberg, F. Zeibert, A. C.-M. Yang, U. Steiner, and G. Reiter. *Physical Review Letters*, **109**, 136102 (2012).
27. A. Silberberg. *Journal of Colloid and Interface Science*, **90**, 86 (1982).
28. H. Bodiguel and C. Fretigny. *Physical Review Letters*, **97**, 266105 (2006).
29. L.J. Fetters, D.J. Lohse, D. Richter, T.A. Witten, and A. Zirkel. *Macromolecules*, **27**, 4639 (1994).
30. L.J. Fetters, D.J. Lohse, and W.W. Graessley. *J. Polym. Sci. Pol. Phys.*, **37**, 1023 (1999).
31. J. Klein. *Nature*, **12**, 144 (1978).
32. P.F. Green and E.J. Kramer. *Macromolecules*, **19**, 1108 (1986).
33. Y. Liu, G. Reiter, K. Kunz, and M. Stamm. *Macromolecules*, **26**, 2134 (1993).
34. A. Karim, G.P. Felcher, and T.P. Russell. *Macromolecules*, **27**, 6973 (1994).
35. P.G. de Gennes. *J. Chem. Phys.*, **35(7)**, 572 (1971).
36. K. Jud, H.H. Kausch, and J.G. Williams. *Journal of Materials Science*, **16**, 204 (1981).
37. S. Prager and M. Tirrell. *The Journal of Chemical Physics*, **75**, 5194 (1981).
38. F. Brochard-Wyart. *Fundamentals of Adhesion*, chapter 6. Plenum Press, New York, 1991.
39. F. Pierce, D. Perahia, and G.S. Grest. *Europhysics Letters*, **95**, 46001 (2011).
40. J. Rottler and M.O. Robbins. *Phys. Rev. E.*, **68**, 011801 (2003).
41. J. Rottler. *Journal of Physics: Condensed Matter*, **21**, 463101 (2009).
42. H.R. Brown. *J. Mater. Sci.*, **14**, 237 (1979).
43. B.D. Lauterwasser and E.J. Kramer. *Phil. Mag. A*, **39(4)**, 469 (1979).
44. J.D. McGraw and K. Dalnoki-Veress. *Physical Review E*, **82**, 021802 (2010).
45. A.M. Donald and E.J. Kramer. *J. Polym. Sci. Pol. Phys.*, **20**, 899 (1982).
46. A.M. Donald and E.J. Kramer. *Polymer*, **23**, 461 (1982).
47. A.C.M. Yang, E.J. Kramer, C.C. Kuo, and S.L. Phoenix. *Macromolecules*, **19**, 2020 (1986).
48. A.G. Emslie, F.T. Bonner, and L.G. Peck. *Journal of Applied Physics*, **20**, 858 (1958).
49. A. Bach, K. Almdal, H. K. Rasmussen, and O. Hassager. *Macromolecules*, **36**, 5174 (2003).
50. J.P. Cotton, D. Decker, H. Benoit, B. Farnoux, J. Higgins, G. Jannink, R. Ober, C. Picot, and J. des Cloizeaux. *Macromolecules*, **7**, 863 (1974).

Appendix B

Other Contributions

Paper 2.i

Numerical solutions of thin film equations for polymer flows

T. Salez, J.D. McGraw, S.L. Cormier, O. Bäümchen, K. Dalnoki-Veress and E. Raphaël, *European Physical Journal E*, **35**, 114 (2012) .

As the space limitations of *Physical Review Letters* prevent the inclusion of long derivations or explanations of methods, we have made two contributions as follow-ups to the manuscripts described in Papers 1.ii and 2.iii. The first of these is a detailed description of the numerical method used to simulate lubrication flows in the two geometries presented here. This numerical method derives from the algorithm presented by Bertozzi [75], and was implemented by T. Salez for the specific cases of our interest. This work allowed us to determine the capillary velocities of all stepped films, and provided crucial information for the expression of the master plot of Paper 1.ii. We also used the method detailed in this paper for simulations of spherical caps on films. The implementation of this numerical technique was also crucial for the analysis of the master plot shown at the end of Paper 2.iii. For Paper 2.i, I collected experimental data, prepared some figures and edited the manuscript after it was prepared by T. Salez.

Paper 2.ii

Capillary-driven flow induced by a stepped perturbation atop a viscous film

T. Salez, J.D. McGraw, O. Bäumchen, K. Dalnoki-Veress and E. Raphaël, *Physics of Fluids*, **24**, 102111 (2012).

In a second follow up to Paper 1.ii we considered the case where the step in the film is only a small perturbation of the film height on the substrate. In this case, it is possible to linearize the governing equation (Eq. 1.35) and an analytical solution is thus possible using Fourier analysis. The resulting linear equation is similar in form to a diffusion equation, and the methods used for solving the classical second order equation are used extensively in this analysis. As we were motivated to undertake this study as a result of the experimental findings in Paper 1.ii, useful relations concerning the geometric dependence are derived. Also, we determined the analytical form for the energy dissipation as a function of time and film geometry. Extrapolating the ansatz proposed for the general $h_2 \approx h_1$ geometry to the small h_2 limit, and comparing to the analytical expression for small h_2 , allowed us to formulate the master plot in Paper 1.ii. Although it was not known to us at the time of publication, we found in the interim period that the equations describing the stepped perturbation can be exactly applied to a system that contains a small mobile layer in the surface layer of an otherwise glassy polymer film.

For this paper, I collected the experimental data, prepared some of the figures, and suggested that the stepped perturbation analysis might provide some insights to the general problem. T. Salez wrote the first draft of this manuscript, and I was involved in all other steps of the editing before submission.

Paper 2.iii

*Beyond Tanners Law: Crossover between Spreading Regimes of a Viscous Droplet on an Identical Film*¹

S.L. Cormier, J.D. McGraw, T. Salez, E. Raphaël and K. Dalnoki-Veress, Physical Review Letters, **109**, 154501 (2012).

We also pursued the capillary levelling of ‘almost flat films’ in a cylindrically symmetric geometry. Here we place PS spherical caps with micrometre dimensions onto a pre-existing PS film. In the case where the film is much smaller than the typical height of the overlaid droplet, the evolution proceeds in close accord with the well known Tanner’s law for droplets spreading on a smooth wettable substrate: $d_0 \sim t^{-0.2}$. Here d_0 is the central height of the droplet. As we increase the height of the film, the physics changes from dissipation dominated at the contact line to dissipation more evenly distributed through the entirety of the droplet. The power law of the spreading transitions smoothly from the Tanner limit to the thick film limit where $d_0 \sim t^{-0.5}$. We find that a droplet levels much faster on a thicker film.

In both of Papers 2.i and 2.iii, it is claimed that self-similarity of the profiles according to Eq. 1.41 was verified using AFM. Since this data does not explicitly appear in either of these manuscripts, it is presented here. In Fig. B.1 is shown a time series of AFM profiles for a 118 kg/mol PS droplet on a PS film of 118 kg/mol. The droplet-and-film was annealed at 140 °C for the cumulative periods of time indicated. Although the early time data does not satisfy the self-similarity, we see that the scaled data asymptotically approaches the self-similar profile for later times, shown in Fig. B.1(b).

All of the experimental data presented in this paper was collected by S. Cormier. I was heavily involved in the experiments at the beginning of this project, and helped with the experimental design, collaborated with S. Cormier on the interpretation of optical data, and helped with data analysis using MATLAB. I was also involved with preparation of the manuscript, including help with some of the figures and editing of the initial manuscript as prepared by S. Cormier.

¹The idea for the experiments presented in this work were inspired by G. Grest’s invited talk during session J4 at the 2010 APS March Meeting in Portland, Oregon.

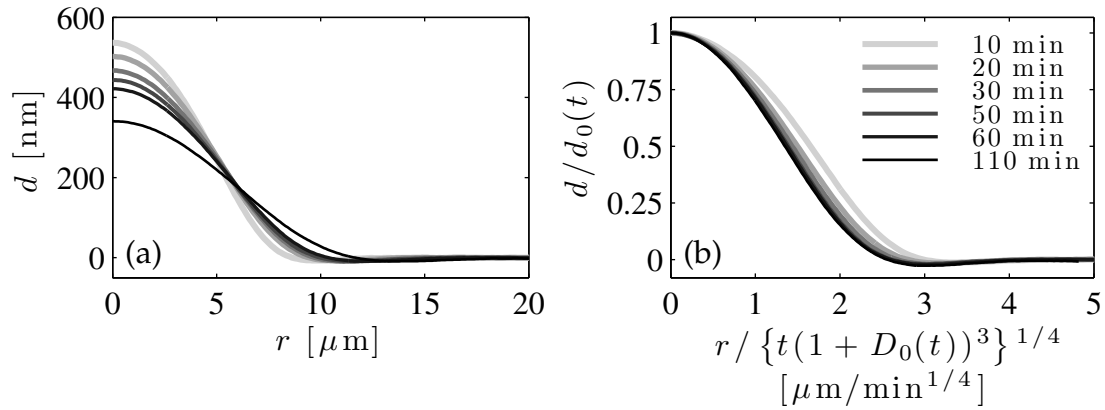


Figure B.1: (a) Droplet levelling profiles for a droplet on a film with $e = 590$ nm. the times are the same for those indicated in (b), where scaled versions of the same profiles are shown. In (b), we have used the self-similar scaling suggested in Eq. 1.41, where $D_0 = d_0/e$.

Paper 2.iv

Step edges in thin films of lamellar-forming diblock copolymer

P. Stasiak, J.D. McGraw, K. Dalnoki-Veress and M.W. Matsen, submitted to *Macromolecules* on 12/10/12, ma-2012-02143q: 10 pages.

A thin film composed of nearly symmetric ($f \approx 0.5$) diblock copolymers typically orders with lamellae oriented parallel to the substrate; however, It is only for special cases that the film thickness is commensurate with the lamellar spacing. In the more general case for which the lamellar spacing is not commensurate with the film height, the surface becomes terraced, and it is perforated with islands, holes, or a bicontinuous structure. The regions between terrace heights impose deformations on the preferred lamellar structure and are thus associated with an energy cost. This paper is mainly a theoretical investigation, using self consistent field theory, of the different structures that form as a result of a terraced topography. We find that the structure of the defects is governed by the fraction of A blocks, f , and depends on the relative sizes of the surface tensions between the two blocks and air, and the interfacial tension between the blocks.

The theoretical work presented in this paper was performed by P. Stasiak. I collected experimental data and was involved with editing later versions of the manuscript.

Paper 2.v

Reduced Glass Transition Temperatures in Thin Polymer Films: Surface Effect or Artifact?

O. Bäümchen, J.D. McGraw, J.A. Forrest and K. Dalnoki-Veress, Physical Review Letters, **109** 055701 (2012).

The glass transition in thin polymer films has attracted tremendous attention in the nearly 20 years since Keddie, Jones and Cory [60] published their first results on T_g depressions in thin supported films. In this Paper, we investigate the effect of changing the number of air-polymer interfaces from two to one. The novelty of this measurement arises from the fact that we measure T_g in the same film for both cases. We find that a polymer film whose glass transition is reduced as measured by ellipsometry in the free standing state, moves to a state in which its glass transition is the bulk value after transfer to a Si substrate. By using the same film with no additional annealing between the free-standing and supported states, we negate the claim that T_g reductions reported elsewhere are entirely due to improper annealing.

All of the experimental data presented in this paper was collected by O. Bäümchen. I was involved with the experimental design, wrote MATLAB analysis codes that were used to extract the thickness and index of refraction from ellipsometry data, and helped in the editing of later versions of the manuscript.

Bibliography

- [1] P.G. de Gennes. *Scaling Concepts in Polymer Physics*. Cornell University Press, 1979.
- [2] M. Rubinstein and R.H. Colby. *Polymer Physics*. Oxford University Press, 2003.
- [3] M. Doi and S.F. Edwards. *The Theory of Polymer Dynamics*. Oxford University Press, 1986.
- [4] G.C. Berry and T.G. Fox. The viscosity of polymers and their concentrated solutions. *Advances in Polymer Science*, 5:261, 1968.
- [5] L.J. Fetters, D.J. Lohse, D. Richter, T.A. Witten, and A. Zirkel. Connection between polymer molecular weight, density, chain dimensions, and melt viscoelastic properties. *Macromolecules*, 27:4639, 1994.
- [6] L.J. Fetters, D.J. Lohse, and W.W. Graessley. Chain dimensions and entanglement spacing in dense macromolecular systems. *Journal Polymer Science: Polymer Physics*, 37:1023, 1999.
- [7] W.W. Graessley. The entanglement concept in polymer rheology. *Advances in Polymer Science*, 16:1, 1974.
- [8] P.G. de Gennes, F. Brochard-Wyart, and Quéré. *Capillarity and Wetting Phenomena: Drops, Bubbles, Pearls, Waves*. Springer, New York, 2003.
- [9] J.N. Israelachvili. *Intermolecular and Surface Forces*. Academic Press, 3rd edition, 2011.

-
- [10] M.W. Matsen. The standard gaussian model for block copolymer melts. *Journal of Physics: Condensed Matter*, 14:R21, 2002.
- [11] M.G. Dunbar, B.M. Novak, and K. Schmidt-Rohr. *Trans* content in atactic polystyrene estimated by double-quantum solid-state nmr. *Solid State Nuclear Magnetic Resonance*, 12:119, 1998.
- [12] J.P. Cotton, D. Decker, H. Benoit, B. Farnoux, J. Higgins, G. Jannink, R. Ober, C. Picot, and J. des Cloizeaux. Conformation of polymer chain in the bulk. *Macromolecules*, 7:863, 1974.
- [13] N. Clisby. Accurate Estimate of the Critical Exponent ν for Self-Avoiding Walks via a Fast Implementation of the Pivot Algorithm. *Physical Review Letters*, 104:055702, February 2010.
- [14] F.S. Bates and G.H. Fredrickson. Block copolymers—designer soft materials. *Physics Today*, 52:32, 1999.
- [15] C. Creton, E.J. Kramer, H.R. Brown, and C.-Y. Hui. Adhesion and fracture of interfaces between immiscible polymers: from the molecular to the continuum scale. *Advances in Polymer Science*, 156:53, 2001.
- [16] I.W. Hamley. Ordering of thin films of block copolymers: fundamentals to applications. *Progress in Polymer Science*, 34:1161, 2009.
- [17] F.S. Bates. Polymer-polymer phase behavior. *Science*, 251:898, 1991.
- [18] R.A.L. Jones. *Soft Condensed Matter*. Oxford University Press, 2002.
- [19] M.W. Matsen and F.S. Bates. Unifying weak- and strong-segregation block copolymer theories. *Macromolecules*, 29:1091, 1996.
- [20] G.H. Fredrickson. Surface ordering phenomena in block copolymer melts. *Macromolecules*, 20:2535, 1987.
- [21] B. Collin, D. Chatenay, G. Coulon, D. Ausserre, and Y. Gallot. Ordering of copolymer thin films as revealed by atomic force microscopy. *Macromolecules*, 25:1621, 1992.

- [22] P.G. de Gennes. Reptation of a polymer chain in the presence of fixed obstacles. *Journal of Chemical Physics*, 35(7):572–579, 1971.
- [23] T.C.B. McLeish. Tube theory of entangled polymer dynamics. *Advances in Physics*, 51:1379, 2002.
- [24] J.D. McGraw. Entanglement swelling in polymer glasses: Chain length dependence on participation in network events. Master’s thesis, McMaster University, Hamilton, 2008.
- [25] J.D. Ferry. *Viscoelastic Properties of Polymers*, 3rd ed. John Wiley & Sons, Inc., 1980.
- [26] D.I. Bower. *An Introduction to Polymer Physics*. Cambridge University Press, 2002.
- [27] R. Hoy. Why is understanding glassy polymer mechanics so difficult? *Journal of Polymer Science Part B: Polymer Physics*, 49(979), 2011.
- [28] E.J. Kramer. Microscopic and molecular fundamentals of crazing. *Advances in Polymer Science*, 52/53:1–56, 1983.
- [29] E.J. Kramer and L.L. Berger. Fundamental processes of craze growth and fracture. *Advances in Polymer Science*, 91/92:1–68, 1990.
- [30] A.C.M. Yang, E.J. Kramer, C.C. Kuo, and S.L. Phoenix. Crazes in diluted networks of polystyrene. *Macromolecules*, 19:2020–2027, 1986.
- [31] A.M. Donald and E.J. Kramer. Effect of molecular entanglements on craze microstructure in glassy polymers. *Journal of Polymer Science: Polymer Physics*, 20:899–909, 1982.
- [32] A.M. Donald and E.J. Kramer. Craze microstructure and molecular entanglements in polystyrene-poly(phenylene oxide) blends. *Polymer*, 23:461, 1982.
- [33] H.R. Brown. Measurement of craze density by quantitative transmission electron microscopy. *Journal of Materials Science*, 14:237–239, 1979.

- [34] L. Si, M.V. Massa, K. Dalnoki-Veress, H.R. Brown, and R.A.L. Jones. Chain entanglement in thin freestanding polymer films. *Physical Review Letters*, 94:127801, 2005.
- [35] B.D. Lauterwasser and E.J. Kramer. Microscopic mechanisms and mechanics of craze growth and fracture. *Philosophical Magazine A*, 39(4):469–495, 1979.
- [36] E.J. Kramer and L.L. Berger. Fundamental processes of craze growth and fracture. *Advances in Polymer Science*, 91/92:1–68, 1990.
- [37] J. Rottler and M.O. Robbins. Growth, microstructure, and failure of crazes in glassy polymers. *Physical Review E*, 68:011801, 2003.
- [38] J. Rottler. Fracture in glassy polymers : a molecular modeling perspective. *Journal of Physics: Condensed Matter*, 21:463101, 2009.
- [39] A. Silberberg. Distribution of Conformations and Chain Ends near the Surface of a Melt of Linear Flexible Macromolecules. *Journal of Colloid and Interface Science*, 90:86, 1982.
- [40] H.R. Brown and T.P. Russell. Entanglements at polymer surfaces and interfaces. *Macromolecules*, 29:798, 1996.
- [41] K. Shin, S. Obukhov, J.-T. Chen, J. Huh, Y. Hwang, S. Mok, P. Dobriyal, P. Thiyagarajan, and T.P. Russell. Enhanced mobility of confined polymers. *Nature Materials*, 6:961, 2007.
- [42] H. Bodiguel and C. Fretigny. Reduced Viscosity in Thin Polymer Films. *Physical Review Letters*, 97:266105, 2006.
- [43] H. Bodiguel and C. Fretigny. Viscoelastic properties of ultrathin polystyrene films. *Macromolecules*, 40:7291, 2007.
- [44] H.D. Rowland, W.P. King, J.B. Pethica, and G.L.W. Cross. Molecular confinement accelerates deformation of entangled polymers molecular confinement accelerates deformation of entangled polymers during squeeze flow. *Science*, 322:720, 2008.

- [45] P.A. O’Connell and G.B. McKenna. Rheological measurements of the thermo-viscoelastic response of ultrathin polymer films. *Science*, 307:1760, 2006.
- [46] P.A. O’Connell and G.B. McKenna. Dramatic stiffening of ultrathin polymer films in the rubbery regime. *European Physical Journal E*, 20:143, 2007.
- [47] E. Lauga, M.P. Brenner, and H.A. Stone. *Handbook of Experimental Fluid Mechanics*, chapter 19. Springer, New York, 2007.
- [48] O. Bäumchen, R. Fetzer, M. Klos, M. Lessel, L. Marquant, H. Hähl, and K. Jacobs. Slippage and nanorheology of thin liquid polymer films. *Journal of Physics: Condensed Matter*, 24:325102, 2012.
- [49] P.G. de Gennes. *Soft Interfaces: The 1994 Dirac Memorial Lecture*. Cambridge University Press, 1997.
- [50] O. Bäumchen, R. Fetzer, and K. Jacobs. Reduced interfacial entanglement density affects the boundary conditions of polymer flow. *Physical Review Letters*, 103:247801, 2009.
- [51] S.G. Croll. The Origin of Residual Internal Stress in Solvent-Cast Thermoplastic Coatings. *Journal of Applied Polymer Science*, 23:847–858, 1979.
- [52] H.A. Schneider and E.A. Di Marzio. The glass temperature of polymer blends : comparison of both the free volume and the entropy predictions with data. *Polymer*, 33:3453, 1992.
- [53] G. Reiter, M. Hamieh, P. Damman, S. Slavovs, S. Gabriele, T. Vilmin, and E. Raphaël. Residual stresses in thin polymer films cause rupture and dominate early stages of dewetting. *Nature Materials*, 4:754, 2005.
- [54] P. Damman, S. Gabriele, S. Coppée, S. Desprez, D. Villers, T. Vilmin, E. Raphaël, M. Hamieh, S. Al Akhrass, and G. Reiter. Relaxation of residual stress and reentanglement of polymers in spin-coated films. *Physical Review Letters*, 99:036101, 2007.

- [55] A. Raegen, M. Chowdhury, C. Calers, A. Schmatulla, U. Steiner, and G. Reiter. Aging of thin polymer films cast from a near-theta solvent. *Physical Review Letters*, 105:227801, 2010.
- [56] K.R. Thomas, A. Chenneviere, G. Reiter, and U. Steiner. Nonequilibrium behavior of thin polymer films. *Physical Review E*, 83:1, 2011.
- [57] M. Chowdhury, P. Freyberg, F. Zeibert, A. C.-M. Yang, U. Steiner, and G. Reiter. Segmental relaxations have macroscopic consequences in glassy polymer films. *Physical Review Letters*, 109:136102, 2012.
- [58] D.R. Barbero and U. Steiner. Nonequilibrium Polymer Rheology in Spin-Cast Films. *Physical Review Letters*, 102:248303, June 2009.
- [59] N.R. Li, A. Clough, Z. Yang, and O.K.C. Tsui. Equilibration of polymer films cast from solutions with different solvent qualities. *Macromolecules*, 45:1085, 2012.
- [60] J.L. Keddie, R.A.L. Jones, and R.A. Cory. Size-dependent depression of the glass transition temperature in polymer films. *Europhysics Letters*, 27, 1994.
- [61] C.J. Ellison and J.M. Torkelson. The distribution of glass-transition temperatures in nanoscopically confined glass formers. *Nature Materials*, 2:695, 2003.
- [62] K. Dalnoki-Veress, J.A. Forrest, C. Murray, C. Gigault, and J.R. Dutcher. Molecular weight dependence of reductions in the glass transition temperature of thin, freely standing polymer films. *Physical Review E*, 63:031801, 2001.
- [63] A. Serghei, H. Huth, C. Schick, and F. Kremer. Glassy dynamics in thin polymer layers having a free upper glassy dynamics in thin polymer layers having a free upper interface. *Macromolecules*, 41:3636, 2008.
- [64] M. Tress, M. Erber, E.U. Mapesa, H. Huth, J. Müller, A. Serghei, C. Schick, K.-J. Eichorn, B. Voit, and F. Kremer. Glassy dynamics and glass transition in nanometric thin layers of polystyrene. *Macromolecules*, 43:9937, 2010.

- [65] G.T. Dee and B.B. Sauer. The molecular weight and temperature dependence of polymer surface tension: Comparison of experiment with interface gradient theory. *Journal of Colloid and Interface Science*, 152:85, 1992.
- [66] G.T. Dee and B.B. Sauer. The surface tension of polymer liquids. *Advances in Physics*, 47:161, 1998.
- [67] A. Oron, S.H. Davis, and S.G. Bankoff. Long-scale evolution of thin liquid films. *Reviews of Modern Physics*, 69:931, 1997.
- [68] M.V. Craster and O.K. Matar. Dynamics and stability of thin liquid films. *Reviews of Modern Physics*, 81:1131, 2009.
- [69] A. Aradian, E. Raphaël, and P.-G. de Gennes. “marginal pinching” in soap films. *Europhysics Letters*, 55:834, 2001.
- [70] P.G. de Gennes. Wetting: statics and dynamics. *Reviews of Modern Physics*, 57:827, 1985.
- [71] L.H. Tanner. The spreading of silicone oil drops on horizontal surfaces. *Journal of Physics D: Applied Physics*, 12:1473, 1979.
- [72] S.L. Cormier. Polymer droplets levelling on thin films of identical polymer. Master’s thesis, McMaster University, 2012.
- [73] L.E. Johns and R. Narayanan. *Interfacial Instability*. Springer, New York, 2002.
- [74] E. Pariam and A. Fernández-Neives. Generation and stability of toroidal droplets in a viscous liquid. *Physical Review Letters*, 102:234501, 2009.
- [75] A.L. Bertozzi. The mathematics of moving contact lines in thin liquid films. *Notices of the American Mathematical Society*, 45:689, 1998.
- [76] L.E. Stillwagon and R.G. Larson. Fundamentals of topographic substrate leveling. *Journal of Applied Physics*, 63:5251, 1988.
- [77] R.D. Deegan, O. Bakajin, T.F. Dupont, G. Huber, S.R. Nagel, and T.A. Witten. Capillary flow as the cause of ring stains from dried liquid drops. *Nature*, 389:827, 1997.

-
- [78] J.S. Sharp and J.A. Forrest. Free surfaces cause reductions in the glass transition temperature of thin polystyrene films. *Physical Review Letters*, 91:235701, 2003.
- [79] C.J. Ellison and J.M. Torkelson. The distribution of glass-transition temperatures in nanoscopically confined glass formers. *Nature Materials*, 2:695, 2003.
- [80] K. Paeng, R. Richert, and M.D. Ediger. Molecular mobility in supported thin films of polystyrene, poly(methyl methacrylate), and poly(2-vinyl pyridine) probed by dye reorientation. *Soft Matter*, 8:819, 2012.
- [81] L. Zhu, C.W. Brian, S.F. Swallen, P.T. Straus, M.D. Ediger, and L. Yu. Surface self-diffusion of an organic glass. *Physical Review Letters*, 106:256103, 2011.
- [82] M. Bowen and T.P. Witelski. The linear limit of the dipole problem for the thin film equation. *SIAM Journal on Applied Mathematics*, 66:1727, 2006.
- [83] L. Léger, H. Hervet, and L. Bureau. Friction mechanisms at polymer-solid interfaces. *Comptes Rendus Chimie*, 9:80, 2006.